1986

Effect of microstructure and mechanical properties on the erosion of 18 Ni (250) maraging steel and aluminum alloys

Mahmood Naim
Iowa State University

Naim, Mahmood

EFFECT OF MICROSTRUCTURE AND MECHANICAL PROPERTIES ON THE EROSION OF 18 NICKEL (250) MARAGING STEEL AND ALUMINUM ALLOYS

Iowa State University PH.D. 1986

PLEASE NOTE:

In all cases this material has been filmed in the best possible way from the available copy. Problems encountered with this document have been identified here with a check mark ✓.

1. Glossy photographs or pages _____
2. Colored illustrations, paper or print _____
3. Photographs with dark background ✓
4. Illustrations are poor copy _____
5. Pages with black marks, not original copy _____
6. Print shows through as there is text on both sides of page _____
7. Indistinct, broken or small print on several pages ✓
8. Print exceeds margin requirements _____
9. Tightly bound copy with print lost in spine _____
10. Computer printout pages with indistinct print _____
11. Page(s) _____ lacking when material received, and not available from school or author.
12. Page(s) _____ seem to be missing in numbering only as text follows.
13. Two pages numbered _____. Text follows.
14. Curling and wrinkled pages _____
15. Dissertation contains pages with print at a slant, filmed as received _____
16. Other _____

_____

_____

Effect of microstructure and mechanical properties on the erosion of 18 Ni (250) maraging steel and aluminum alloys

by

Mahmood Naim

A Dissertation Submitted to the
Graduate Faculty in Partial Fulfillment of the
Requirements for the Degree of
DOCTOR OF PHILOSOPHY

Major: Mechanical Engineering

Approved:

Signature was redacted for privacy.
In Charge of Major Work

Signature was redacted for privacy.
For the Major Department

Signature was redacted for privacy.
For the Graduate College

Iowa State University
Ames, Iowa

1986

TABLE OF CONTENTS

		Page
INTRODUCTION		1
PAPER 1:	EFFECT OF MICROSTRUCTURE AND MECHANICAL PROPERTIES ON THE EROSION OF 18 Ni (250) MARAGING STEEL	4
PAPER 2:	EROSION OF PRESTRAINED AND AGED 2024 ALUMINUM ALLOY	50
PAPER 3:	EFFECT OF PRECIPITATED AND DISPERSED HARD PARTICLES ON EROSION	71
PAPER 4:	STUDY OF SUBSTRATE DEFORMATION BY PHOTOELASTICITY IN SINGLE PARTICLE IMPACTS	94
PAPER 5:	SUBSURFACE DEFORMATION STUDIES IN IMPACT EROSION AND PLOWING BY PHOTOELASTICITY	119
SUMMARY		149
ACKNOWLEDGMENT		152

INTRODUCTION

In many areas of engineering applications solid particle erosion results in a serious and costly form of damage. For example, in pneumatic transport of solid particles the enclosing ducts are eroded severely. The efficiency of turbomachinery and other equipment used in catalytic cracking of oil, coal industry, energy recycling plants, mining and pulverized coal burning, is limited due to erosive wear. Mechanical erosion is one of the primary problems in the design and selection of materials for solid propellant nozzles.

The past decade has seen intensified interest in the studies of erosion phenomena on a variety of industrial problems. Specifically, erosion damage caused by ingestion of dusty clouds by vehicles such as helicopters, hovercrafts, V/STOL aircraft has been given much attention due to its economic importance. The damage is principally caused by erosion of the compressor blading which results in significant reduction of the operating life of the engine. Erosion in the gas turbines using the flue gases from coal combustion in pressurized fluidized beds has regenerated interest in evaluation of materials subjected to erosion at elevated temperatures. The possibility of erosion damage to space vehicles on certain planets with dust storms carrying large size particles is also of concern.

Erosion can also be beneficial. Sand blasting and abrasive jet machining or cutting are a few examples.

A review of erosion research indicates that the effect of operating parameters like impact angle, velocity, particle size and shape is well established. The erosion mechanisms can be classified in terms of cutting, plowing, and cracking. However, further studies are desired to establish the subsurface deformation under dynamic impact conditions.

The effect of the variation of the target material properties on erosion is the least understood. There is a general lack of systematic studies where the mechanical properties of the target material are changed by various means and their resistance to erosion is evaluated.

In this study, the phenomenon of erosion is analyzed by selecting precipitation hardening systems, and the results are classified in five papers.

Paper 1 relates the erosion to the variations of mechanical properties and the microstructure obtained by thermomechanical treatments of the 18 Ni (250) maraging steel. Erosion mechanisms are also identified by scanning electron microscopy of the eroded surfaces and debris.

Paper 2 analyzes the erosion behavior of prestrained and aged 2024 aluminum alloy. The variation of erosion is

related to tensile properties and the resulting microstructure. The effect of precipitate size on erosion is also evaluated. Paper 3 further establishes the effect of precipitated and dispersed hard particles on erosion. Here 2011 aluminum alloy is heat treated to obtain large variation in precipitate size. Also, alumina particles of various sizes and concentrations are dispersed in phenolformaldehyde to determine their effect on erosion.

Paper 4 establishes dynamic photoelasticity methods that can be used to study the subsurface deformation caused by a single particle impact. The approach determines the dynamic stresses and the strain rate of deformation during the impact process. Paper 5 again uses photoelasticity techniques to determine the propagation of an impact induced stress field. The residual stress field after repeated impacts is evaluated and its contribution to material removal is discussed. The mode of material detachment and the residual stress field generated due to a particle sliding on both the ductile and brittle materials is also analyzed. The conclusions are summarized at the end.

PAPER 1:

EFFECT OF MICROSTRUCTURE AND MECHANICAL PROPERTIES ON THE EROSION OF 18 Ni (250) MARAGING STEEL

ABSTRACT

Specimens of 18 Ni (250) maraging steel were solution treated and aged at the temperatures of 480° C, 590° C, and 650° C for varying times up to a maximum of 24 hours. Solution annealed specimens were also cold rolled to varying amounts. The erosion behavior of these specimens was studied in a sand-blast type test rig. The tests were conducted under ambient conditions with 125 μm angular silicon carbide particles impacted with a velocity of 50 m/s and at an angle of 30° to the specimen surface.

The variation of erosion has been related to the microstructural changes during aging which involve precipitation, reversion of austenite, and precipitate particle growth. It has also been studied with respect to the mechanical properties. It was found that the erosion rate depends both upon the hardness and ductility. The erosion rate varies directly with hardness when ductility remains constant and it varies inversely with the square of percent area reduction when hardness remains constant.

Scanning electron microscopy of the eroded surfaces and debris revealed that erosion was accompanied by a large amount of plastic deformation and the eroded particles were in the form of small flakes. The flakes were detached because of a combination of cutting, plowing, and crack propagation mechanisms.

INTRODUCTION

Erosion is encountered by a variety of components used in machinery related to agricultural, mining, oil drilling, aerospace applications, etc. Landing gear parts in the helicopters and aircrafts, jet engine starter impellers, rocket motors, and hydrofoils which are made of maraging steel are subjected to erosive atmosphere.

Most of the early work [1-6] on erosion was directed toward the experimental studies related to specific laboratory conditions and the development of empirical equations from the data. Whereas there is a fair knowledge of the operational factors affecting erosion, the understanding of the effect of mechanical and thermal treatments of materials on the erosion process is still in its infancy. Attempts are now being made to study the effect of microstructures and mechanical properties of materials on their erosion behavior. Finnie et al. [7] studied the erosion of AISI 1045 steel in the annealed, hot rolled, and water quenched (untempered and tempered) conditions subjected to a stream of silicon carbide particles. They found that a slight decrease in erosion resistance occurred due to a four-fold increase in hardness resulting from the different heat treatments. These workers also observed that the erosion resistance of Type 01 tool

steel was still lower on tempering. The change in erosion resistance for both the steels when heat treated in different ways (as described above) was fairly small even though there was a large change in hardness. It was mentioned that the change in ductility due to heat treatment was probably a more significant factor in affecting erosion than the change in hardness.

Christman and Shewmon [8] studied the erosion of commercially pure aluminum and 7075 Al alloy by impacting 3/16 inch diameter hardened steel balls normal to the target surface and obtaining overlapping craters. It was found that the aluminum alloy in the annealed condition (150 KHN) was more erosion resistant than in the T-651 condition (aged and strained to a hardness of 210 KHN). When the alloy was overaged to a hardness of 175 KHN, the erosion resistance was seriously impaired. It was surprising to observe that 1100 Al had better erosion resistance than 7075 Al in any of the heat treatment conditions. This observation led these workers to say that the erosion occurs because of shear localization, and the critical factor governing the erosion resistance is not the strength of the material but instead its resistance to shear localization.

Salik and Buckley [9] eroded 6061 Al with glass beads. They found that the solution treatment which resulted in

increased hardness provided higher erosion resistance. The subsequent aging treatment in which case the hardness initially increased and later decreased resulted in poorer erosion resistance.

Salik and Buckley [9] also performed erosion studies on AISI 1045 steel in the annealed, normalized, spheroidized, austempered, water quenched, and tempered conditions. These heat treatments resulted in different microstructures with varying hardness values. The only conclusion that they could draw from this work was of a general nature: the metallurgical changes affected erosion resistance more significantly than the change in hardness. Levy [10] studied the erosion of AISI 1020 and 1075 steels using silicon carbide particles. These steels were heat treated in a way so as to keep hardness changes small. He found that in the case of 1075 steel the spheroidized microstructure was more erosion resistant than the pearlitic structure. The pearlitic microstructure with coarse pearlite provided higher erosion resistance than the one with fine pearlite. This would mean that the erosion resistance decreased with increasing rather than decreasing hardness. The same was found true when the hardness of spheroidized 1075 steel was increased by coldworking. The erosion resistance of 1020 steel was found to depend

ambiguously upon the distribution of hard, brittle θ phase and soft, ductile α phase, since in only two out of the three tests the erosion decreased with increase in distance between the brittle carbide spheroids. With further increase in particle spacing, the erosion increased and matched the behavior of low strength ferrite matrix. It led Levy to conclude that when the ductile α phase became the predominant matrix, so that the resulting strength of the steel was markedly lower, then the strength and not the ductility became the controlling factor in erosion. Foley and Levy [11] reported that they could not find any correlation between erosion and fracture toughness, charpy impact strength, tensile strength, and hardness in the case of AISI 4340 steel. Erosion did seem to correlate weakly with ductility.

Sargent et al. [12] studied the erosion of AISI 1050 and 1080 steels in the normalized and water quenched conditions when eroded by Al_2O_3 and coal ash particles. They found that the erosion resistance of both the steels of Al_2O_3 particles was about the same except in the 30° to 50° angle of impingement range where the 1080 steel in the water quenched condition was slightly less resistant than in the normalized condition. In the water quenched condition, the 1080 steel was more erosion resistant to ash particles than the 1050 steel.

Some recent work has been directed toward the understanding of the mechanisms involved in the erosion process [13-15]. Single particle impact studies have proven very successful in this respect. They have shown that the steady state erosion is preceded by an incubation period, and a definite amount of subsurface plastic strain is induced before the detachment of material occurs [15]. When brittle materials are subjected to impacting particles, ring cracks [1,16] and cone fractures [5] are observed. It means that erosion occurs by the process of crack propagation and chipping [17]. As for the ductile material, the mechanisms appear to be different for both the oblique and normal impacts [18]. In the former case, a scar is produced because of the impingement of the sharp corner of an irregularly shaped particle upon a surface [7]. The material removal is due to the displacement of the particle along the surface, and the fracture is preceded by a large amount of plastic strain [13]. The material that piles up along the edges of the scar is fragile and, therefore, gets damaged during subsequent impacts. This characteristic mode of material has been termed plowing [19]. It was observed that glancing impacts cause "cutting" erosion while "plowing" or deformation erosion dominates at angles close to 90° [20]. Tilly [21] accounts for 90° impact erosion in

terms of the fragmentation of impacting particles. The observation of intense localized shear deformation in narrow bands (termed adiabatic shear bands) has led some research workers [22,23] to raise the possibility of localized temperature rise. However, no direct measurement of such a temperature rise has been reported.

The phenomenon of erosion is very complex, and the understanding of the general mechanisms operative in erosion is far from having been resolved. Erosion has mostly been treated as a cutting [1] or plowing [19] process for ductile materials accompanied by large plastic deformation [13] along with the possibility of localized melting [20,23]. Except for the work by Levy [10] on AISI 1020 and 1075 steels, no one has studied how the various phases in the microstructure affect the erosion process. Thus, apart from the phenomenological aspects, there is very little known about the mechanisms of erosion in terms of the microscopic and submicroscopic structures of material. The variation in erosion behavior due to changes in mechanical properties produced by the thermal and thermo-mechanical treatments have not been reported in any systematic way.

In this paper, the erosion behavior of maraging steel which is used for structural components subjected to erosive atmospheres has been studied. The microstructural changes

have been correlated with the changes in erosion resistance. The effect of strength and ductility on erosion has been investigated by keeping one of these constant. Erosion mechanisms have also been studied briefly.

EXPERIMENTAL

Erosion tests were performed in a sand-blast type of test rig shown in Fig. 1. The eroding particles were fed from a chamber, A, into a stream of gas at mixer, B. They were accelerated using nitrogen gas drawn from a high pressure cylinder, C, in a glass tube, D, of 3 mm inside diameter and 300 mm length. The particle velocity in the test rig could be varied by adjusting the gas regulating valves in the pressure control system. The test samples were mounted on the specimen holder, E, which could be rotated so as to vary the angle of impact from 0° to 90°. A double-disk rotating device [24] was used for measuring the velocity of impacting particles. Angular silicon carbide particles, 125 μm in size, were used as the eroding material. All tests were performed at room temperature with an average particle velocity of 50 m/s. The particle feed rate was found to be 20 g/min. The gap between the specimen surface and the acceleration tube end was kept at 6 mm. The angle of impingement was fixed at 30° to maximize the erosive loss [7].

The specimens were eroded with a total of 200 g abrasive. The first two exposures were made with 20 g charges and the latter four with 40 g each. After each exposure, the specimen was removed from its locating

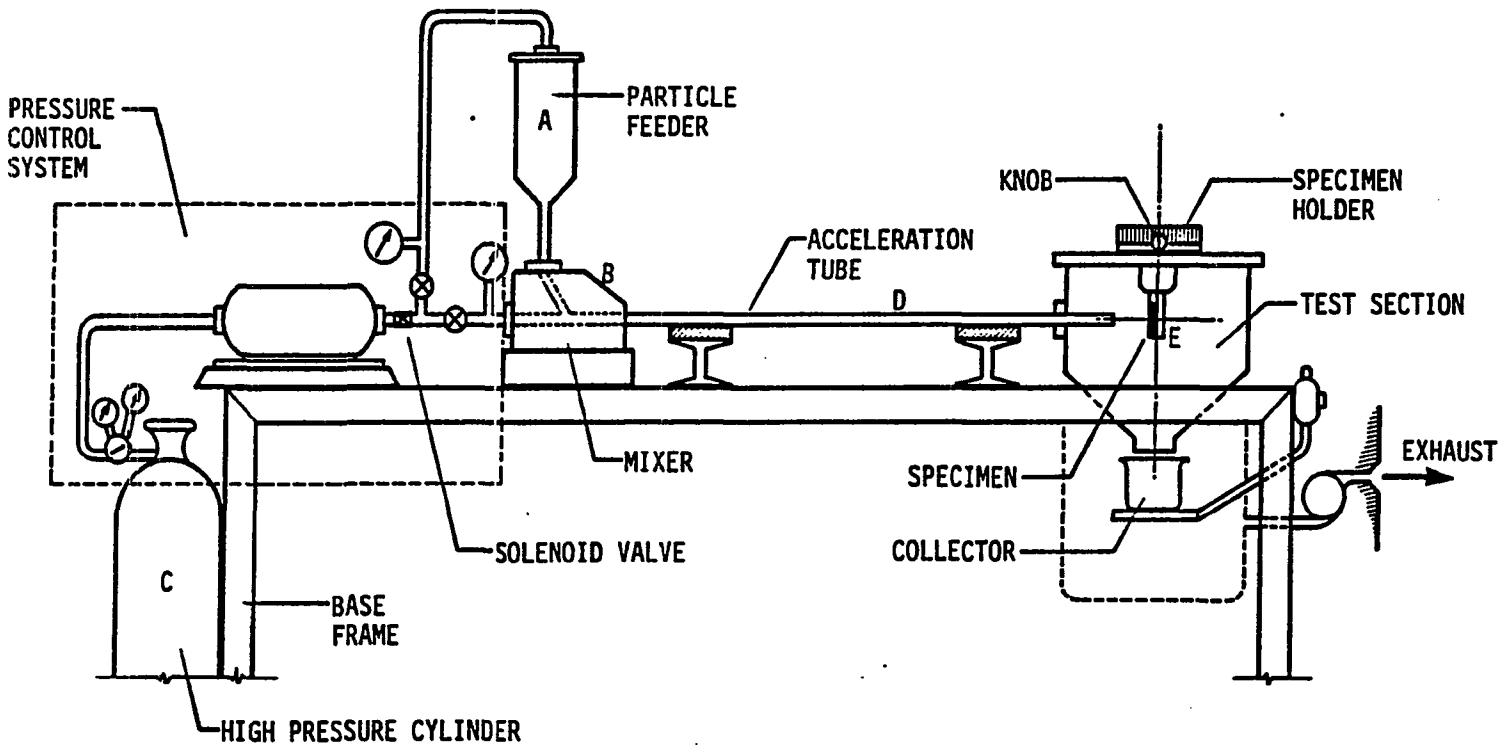

FIGURE 1. Layout of erosion test rig

fixture, brushed off lightly, and weighed to determine the erosive mass loss.

Specimens for the erosion tests were cut in the size 25 mm x 19 mm x 6 mm from flats of 25 mm x 6 mm cross-section of commercially available material. They were solution annealed at 815° C for 1/2 h and then air cooled. The samples were later aged in a salt bath at 480° C, 590° C, and 650° C temperatures for various lengths of time. The opposite flat sides of these specimens were ground parallel. The erosion test surface was polished in running water with emery paper down to a 600 grade finish. Final polishing was done on a rotary polishing cloth using water-suspended alumina particles of the size 0.3 μm and later 0.05 μm.

Tensile specimens were machined, heat treated along with erosion samples, and tested in an electromechanical universal tensile testing machine. Rockwell C hardness was measured, and Brinell hardness readings were taken using 3,000 kg load. Specimens for the tension and erosion test were also prepared from the solution annealed maraging steel cold rolled to 9%, 18%, 35%, 45%, 52%, 65%, and 83% area reduction.

Scanning electron microscopy of the eroded surfaces and the erosion debris was performed using JEOL JSM-U3 Scanning Electron Microscope equipped with a Tractor Northern TN-2000 energy dispersive X-ray analyzer.

RESULTS AND DISCUSSION

Effect of Precipitation Hardening on Erosion

The aging of solution treated maraging steel was done at three different temperatures, viz., 480° C, 590° C, and 650° C, for lengths of time up to a maximum of 24 h to obtain a complete spectrum of behavior in terms of the variation of hardness with aging time is shown in Fig. 2. It should be noted that the aging temperature of 480° C is commonly used in commercial practice.

The above heat-treated specimens were tested under the erosive conditions stated earlier. The plot of erosive mass loss of maraging steel specimens versus the mass of erodent particles impacted is shown in Fig. 3 for the specimens aged at 480° C. The data points plotted are the mean of at least two erosive runs for each condition. A straight line was fitted through the corresponding data points by the method of least squares and a correlation coefficient higher than 0.987 was obtained in all the cases. A similar correlation coefficient was found when erosion data for the specimens aged at 590° C and 650° C were fitted. The slopes of these straight lines represent the erosion rate, $\dot{\varepsilon}$, which is the mass of material lost from the test specimen in milligram per gram of abrasive impacted.

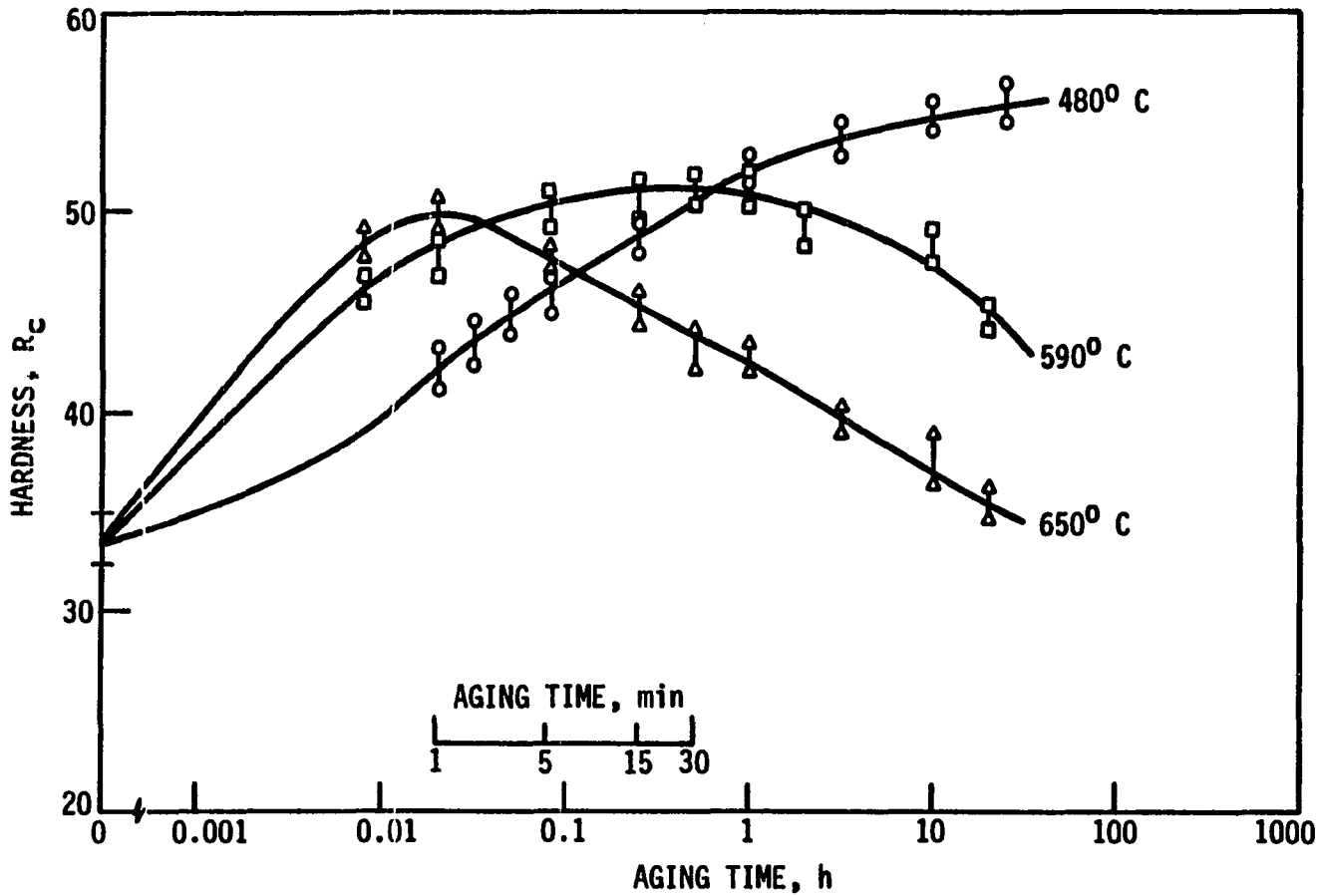

FIGURE 2. Variation of hardness with aging time for 18 Ni (250) maraging steel

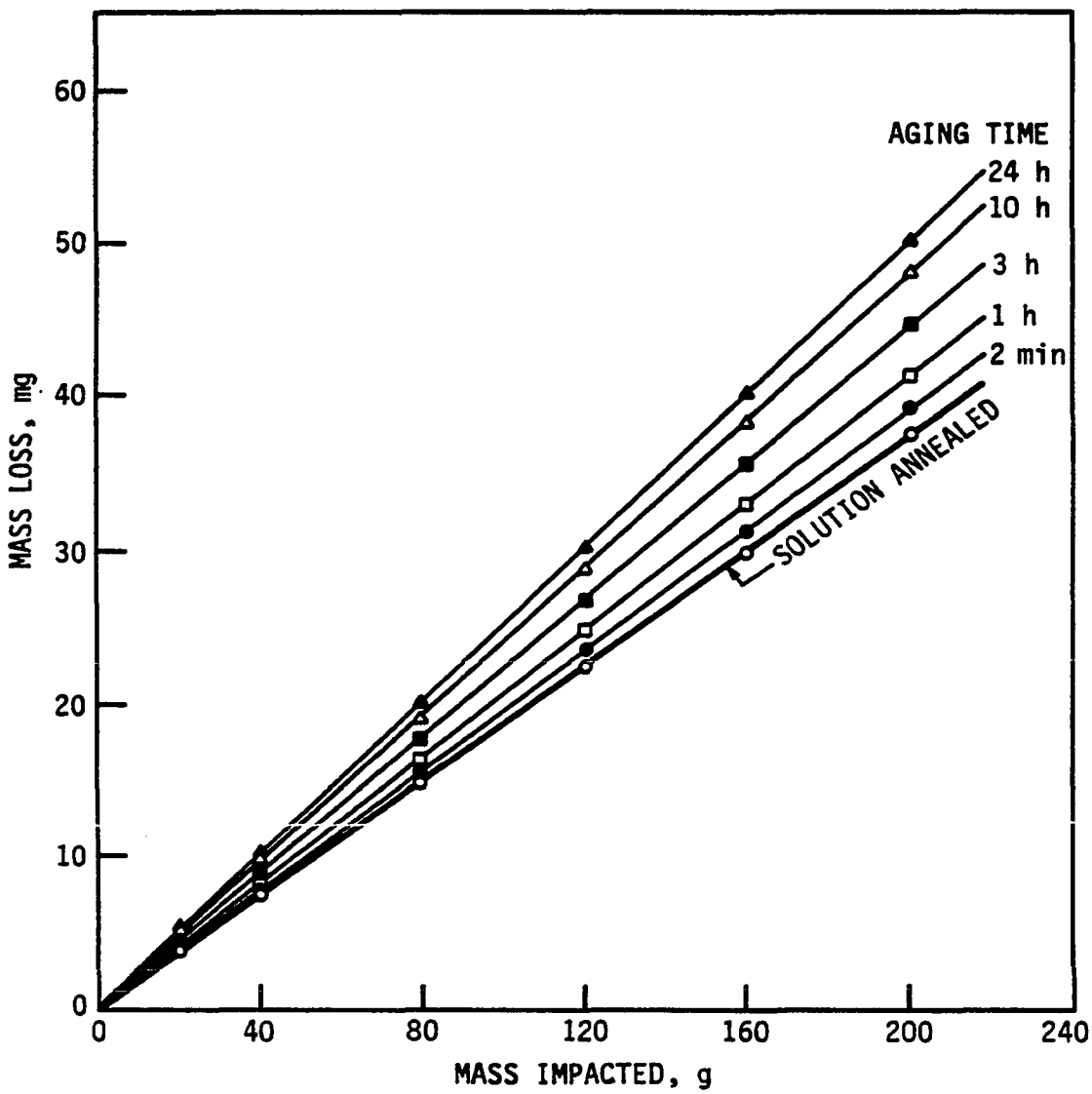

FIGURE 3. Variation of erosion with varying amount of SiC abrasive impacted for 18 Ni (250) maraging steel aged at 480° C for varying lengths of time. Erosion conditions: $\alpha = 30°$, $v = 50$ m/s

The variation of erosion rate with aging time is shown in Fig. 4. Whereas aging for 1 min at the temperatures of 480° C, 590° C, and 650° C results in the increase of Rockwell hardness by about 25%, 43%, and 48% respectively, over that of the solution annealed condition, the erosion rate remains practically unchanged. With further aging, the erosion rate continues increasing for the samples aged at 480° C in which case no overaging was observed up to an aging time of 24 hours. In the case of aging at 650° C and 590° C, whereas the peak hardness was reached in about 1 min and 30 min, respectively, the erosion peaked at 1 h and 30 min correspondingly. When aged further at these two temperatures, the hardness decreased and so did the erosion rate.

The erosion behavior was examined in terms of the microstructural changes occurring in the material. It has been well documented [25] that aging in maraging steels results in the recovery of martensite, the formation of precipitates, and the reversion of Ni-rich austenite. The rapid hardening from aging arises from the formation of Ni_3Ti and Fe_2Mo precipitates in the matrix [26]. The amount of austenite formed has been reported [25] to increase with aging time and temperature, as shown in Fig. 5. In order to relate erosion with microstructural changes, it was

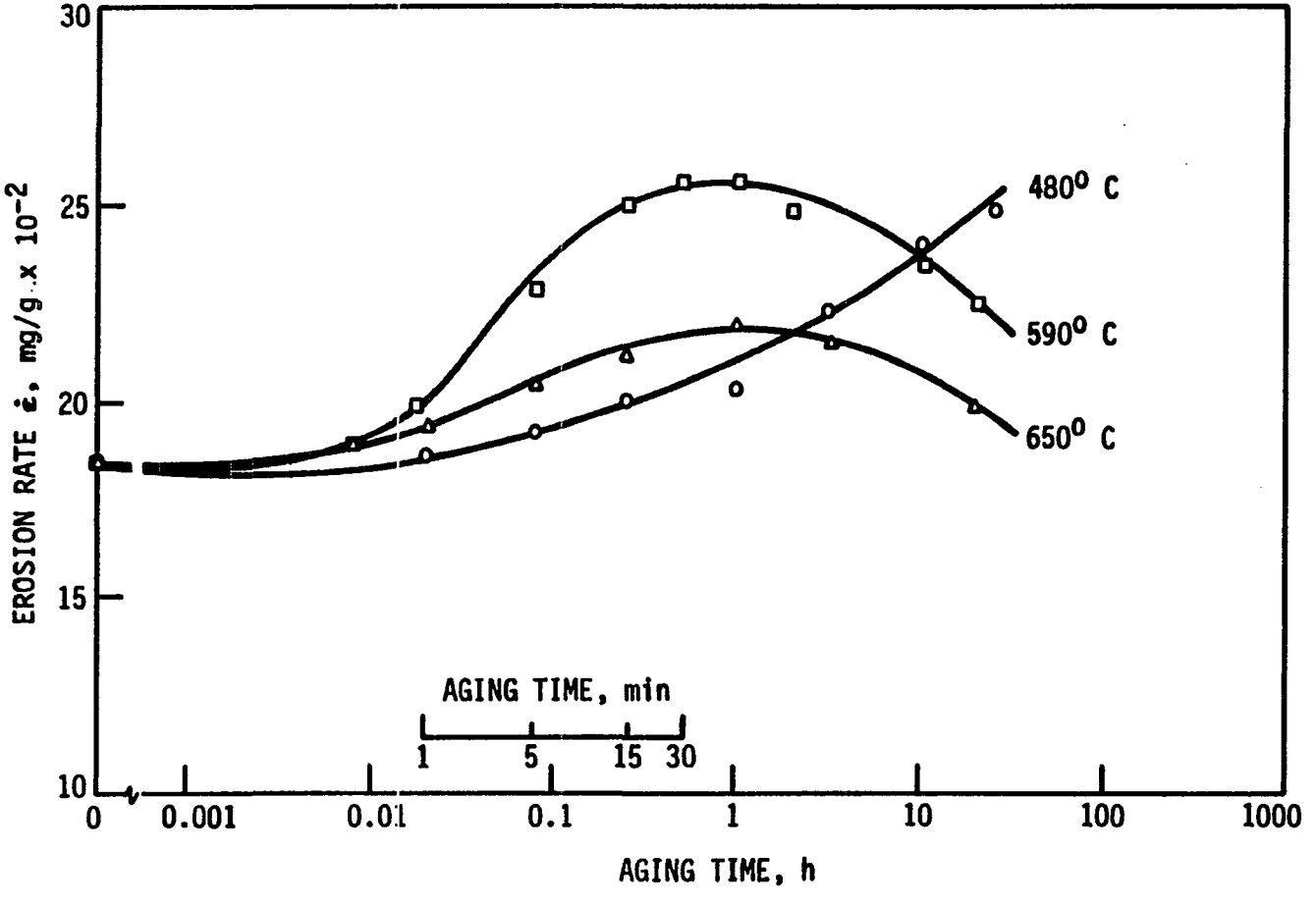

FIGURE 4. Variation of erosion rate with aging time for 18 Ni (250) maraging steel aged at three different temperatures. Erosion conditions: $\alpha = 30°$, v = 50 m/s

considered necessary to determine the variation of the amount of austenite reverted as a function of aging time for the three aging temperatures relevant to the erosion data. Since any such correlation is possible only on a qualitative level, it was unnecessary to determine the exact values experimentally by X-ray diffraction. Instead the austenite variation was extrapolated from the data reported in the literature (see Fig. 5) using the Arrhenius equation. An Arrhenius plot using the time for 10% austenite reversion as the basis is shown in Fig. 6. It provided the time shifts needed to represent the austenite reversion behavior for aging temperatures of 480° C, 540° C, 590° C, and 650° C, and the shifted curves are shown in Fig. 7. The additional 540° C temperature was included in order to check the validity of this procedure with the experimental data reported for this temperature by Peters [27]. These data points are also plotted in Fig. 7 which confirm a reasonable agreement between the experimental and extrapolated curves. A small scatter for low values of reverted austenite is not of any concern from the viewpoint of erosion, as will be seen later. It is probably due to the presence of additional element Ti in the experimental material because Ti has been reported to retard the reversion of austenite [27].

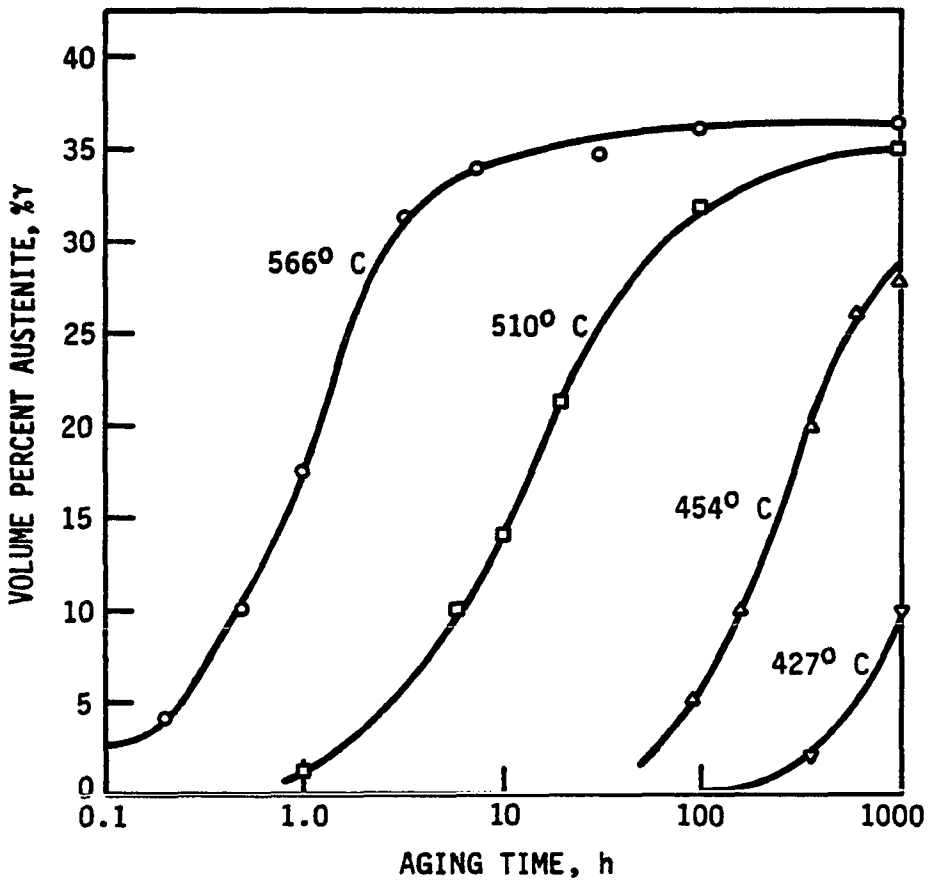

FIGURE 5. Variation of austenite reversion as a function of aging time for several temperatures. Maraging steel composition: 17.4% Ni, 5.67% Mo, 7.80% Co, 0.03% C, balance Fe

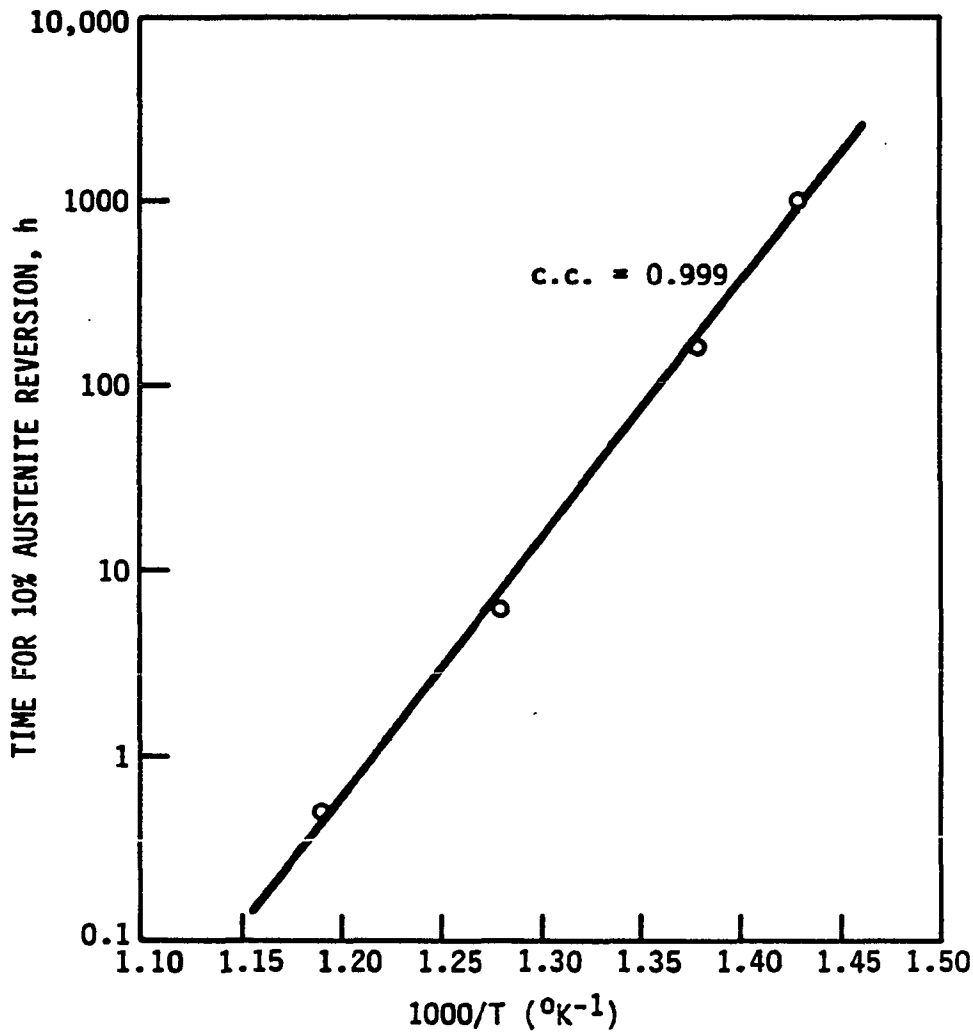

FIGURE 6. Arrhenius plot relating austenite reversion and aging temperature for maraging steel

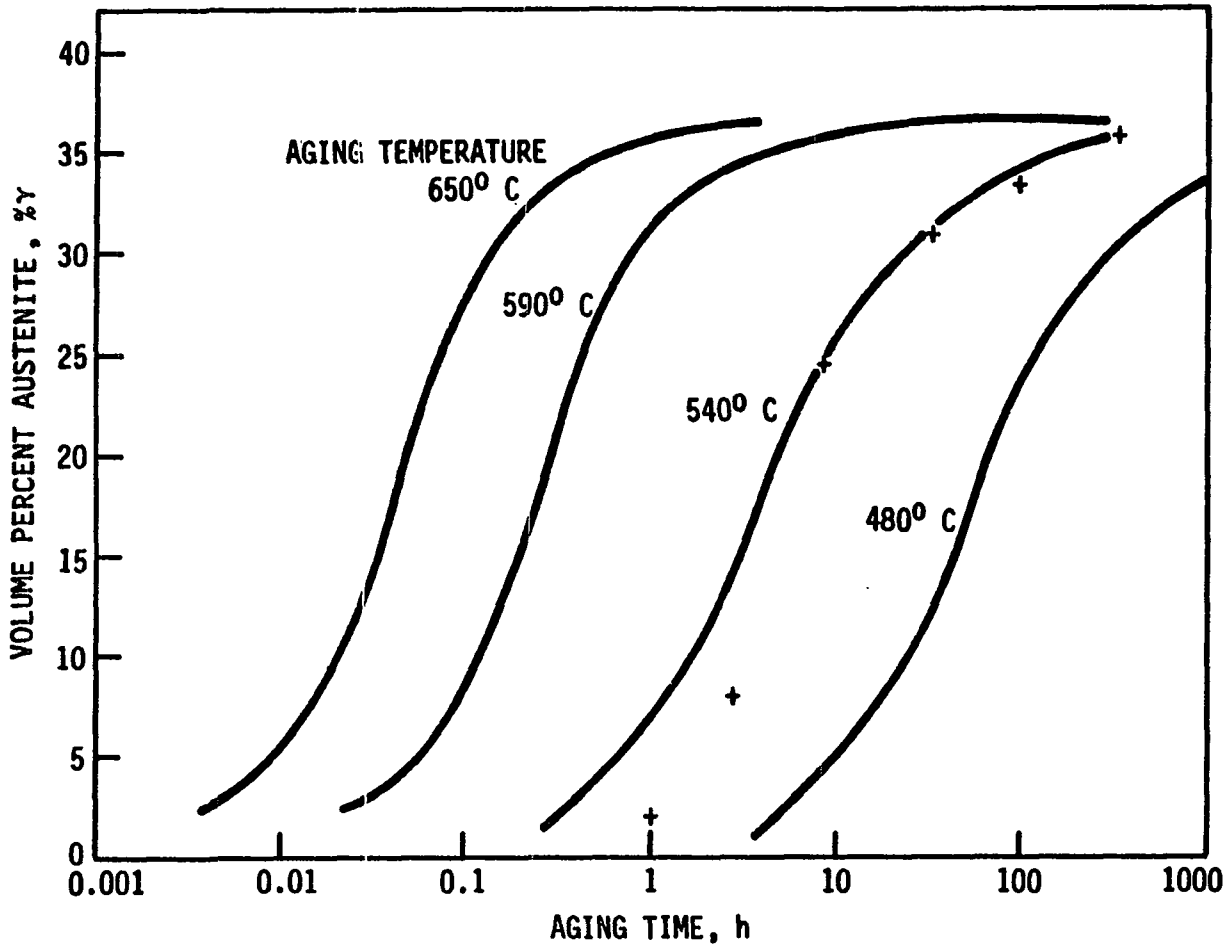

FIGURE 7. Austenite reversion versus aging time for 18 Ni (250) maraging steel evaluated using the Arrhenius plot in Fig. 6. Data marked with + from Reference [27]

Figures 8, 9, and 10 show the relationship of austenite reversion to hardening and erosion rate for the three aging temperatures used in this work. When aging is done at 480° C, precipitation increases hardness continuously up to an aging time of 20 hours. At this point, the hardness tends to level off and the austenite reversion reaches about 10% by volume. The erosion rate keeps increasing along with hardness with no sign of any moderating effect.

Aging at 590° C (see Fig. 9) is accompanied by an initial rapid increase in hardness due to increasing precipitation which later gets moderated because of the start of austenite reversion. There is evidence of some precipitate particle growth occurring during the later part of aging as well. Miller and Mitchell [26] have reported that precipitates grow from disks of 50-100 Å in diameter into spheroids of 200-300 Å in diameter during aging in the temperature range of 480° C to 640° C over a period of 1 hour to 3 hours. However, softening is believed to be much more due to the formation of significant amount of austenite and only a little due to the growth in precipitate particle size [28]. Based on the above analysis, the aging behavior of maraging steel has been divided into three zones in Fig. 9. The first zone is related to mostly precipitation hardening and very little to austenite reversion. In the

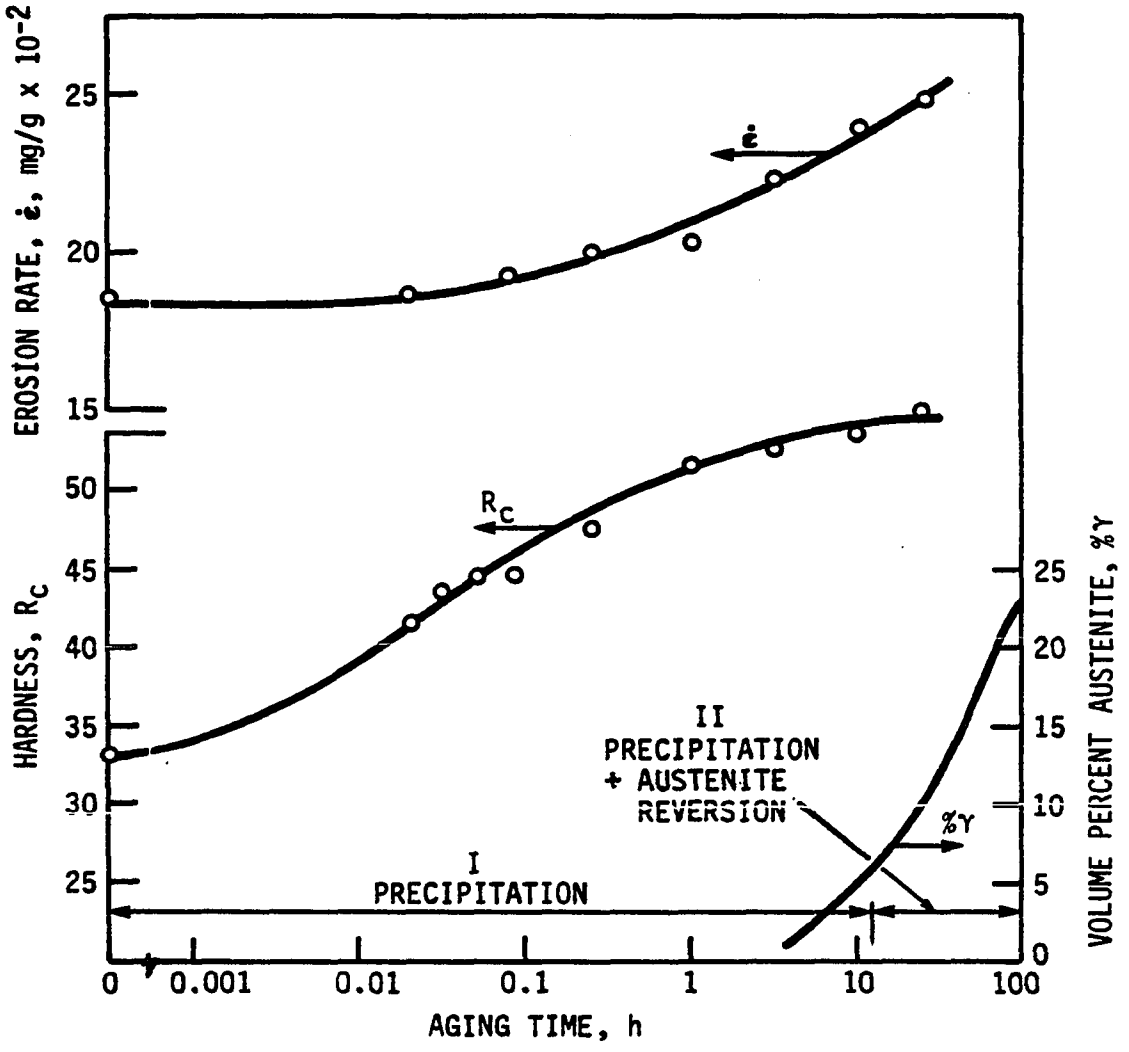

FIGURE 8. Variation of erosion rate with hardness and austenite reversion for 18 Ni (250) maraging steel aged at 480° C

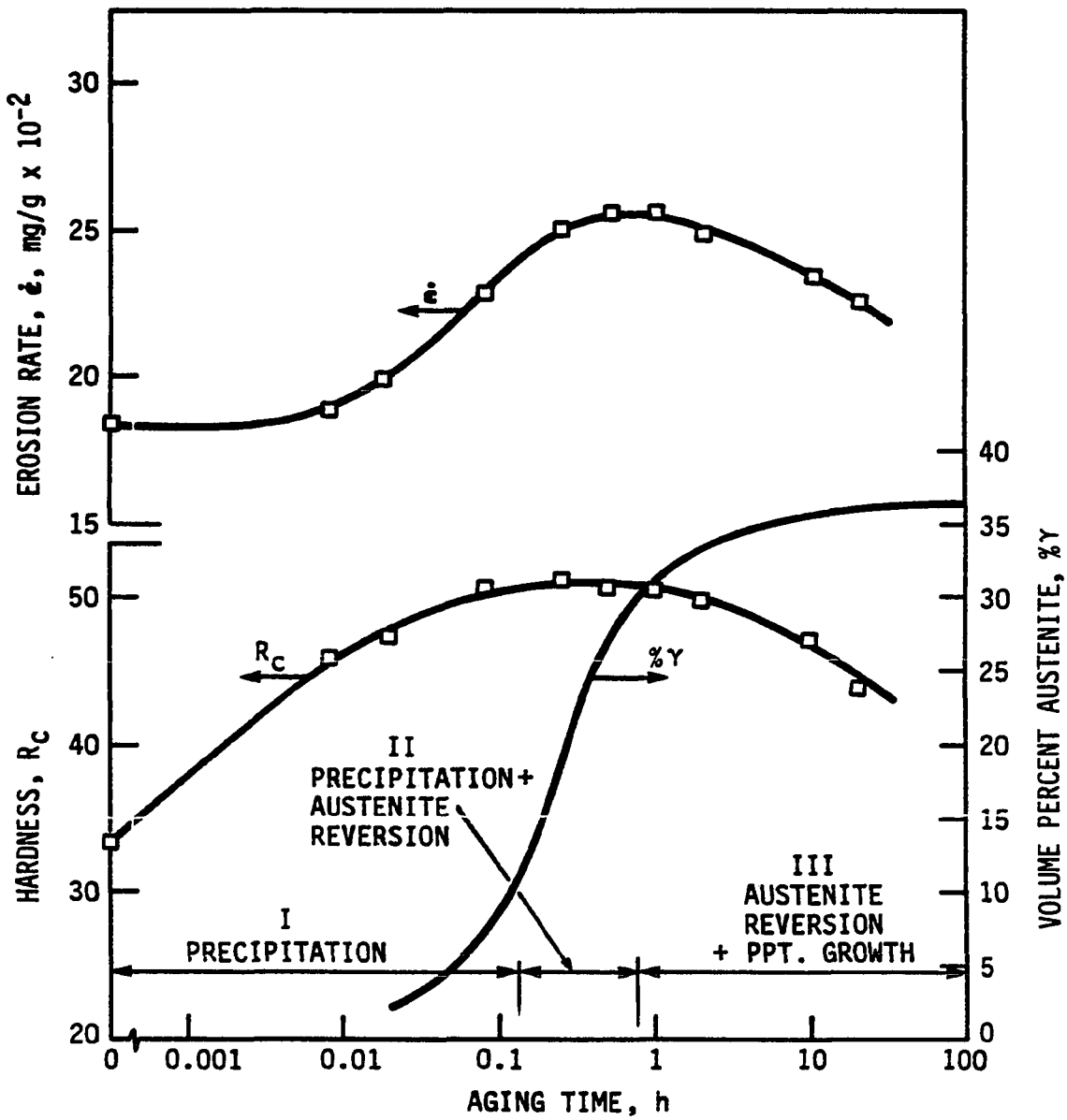

FIGURE 9. Variation of erosion rate with hardness and austenite reversion for 18 Ni (250) maraging steel aged at 590° C

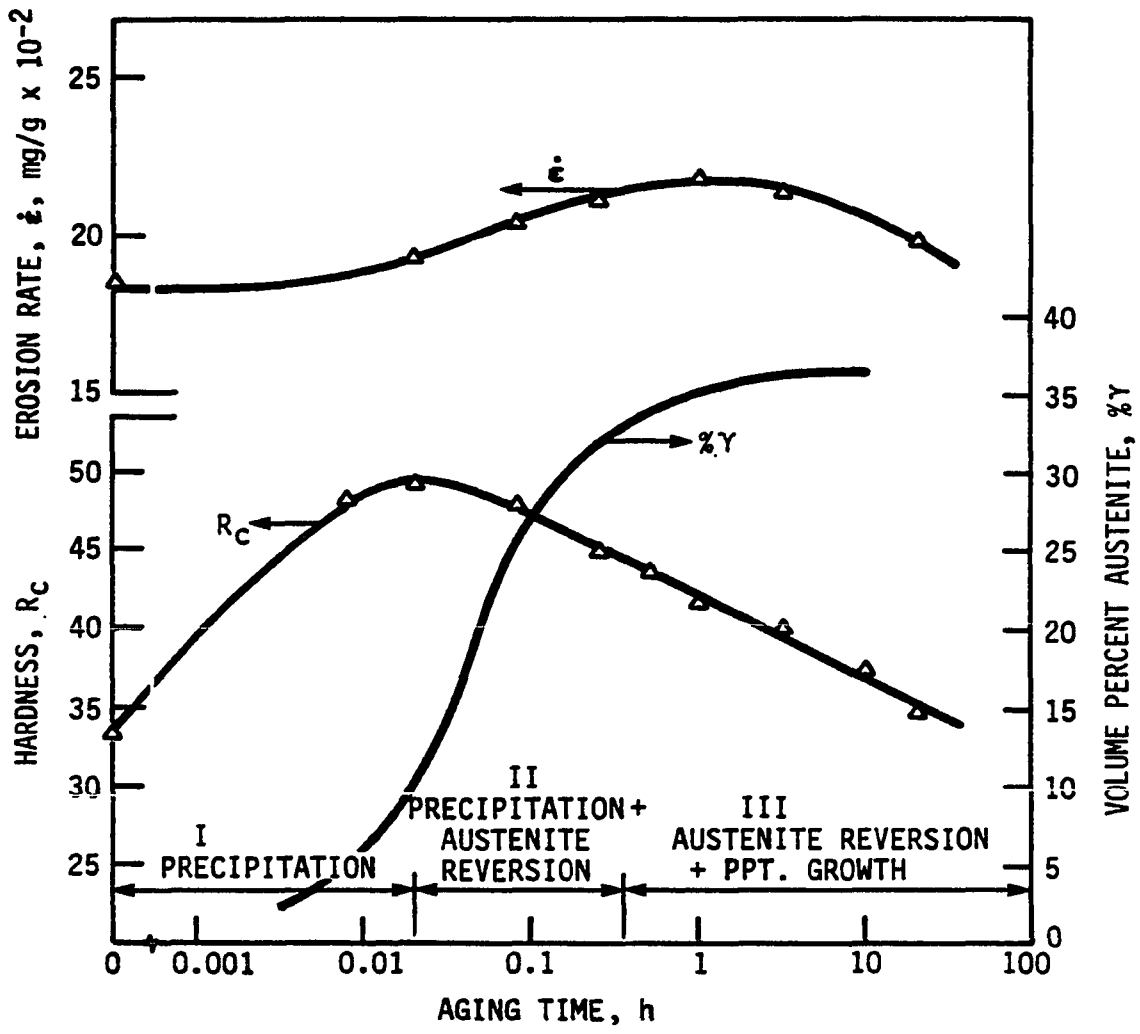

FIGURE 10. Variation of erosion rate with hardness and austenite reversion for 18 Ni (250) maraging steel aged at 650° C

second zone, austenite reversion takes place at a very rapid rate and it is also accompanied by precipitation. Since these two processes affect hardness in opposite ways, the hardness of the material levels off and later starts decreasing. In the third zone, which represents overaging the drop in material hardness is due to the reversion of significant amount of austenite and softening from precipitate particle growth. These three zones signifying the characteristic phenomena in terms of the microstructural changes have also been marked in Figs. 8 and 10. It should be noted that the higher the aging temperature, the shorter the aging time needed for the commencement of zones II and III.

The erosion behavior may now be examined in terms of the microstructural changes occurring in these three zones. There is no effect on erosion until appreciable precipitation strengthening has occurred. With increased precipitation for longer aging times, the erosion rate starts increasing. When aging is done at 480° C, the erosion rate does not show any sign of moderation up to an aging time of 20 hours which corresponds to about 10% austenite reversion. The same holds true for aging temperatures of 590° C and 650° C where the erosion rate rises to a maximum with increased aging time and then starts

decreasing. The drop in erosion rate occurs when austenite reversion reaches about 30% to 35%. Afterwards, the erosion rate continues decreasing because of the softening due to increased austenite reversion and precipitate particle growth.

It should be noted that the conditions for maximum strength and minimum erosion rate are different. The erosion rate in the solution treated condition is the lowest and so is the hardness. This would not be a desirable condition to use in practice. For applications where maximum strength and minimum erosion are sought, aging at a temperature of 650° C appears to be the best because the peak hardness of 50 R_C (50% increase over the solution treated hardness) is being obtained with practically no increase in erosion rate over that of the solution treated condition.

Effect of Mechanical Properties on Erosion

In order to examine the relationship between tensile properties and erosion, tensile tests were run on the samples aged at 590° C. This case was selected because it provides conditions for both the aging and overaging. The variation of Brinell hardness (BHN), ultimate strength, and percent area reduction as a function of the aging time is

shown in Fig. 11. Since hardness and ultimate strength vary in the same manner, hardness alone will be used for the strength parameter in later discussion. It is noted that whereas aging produces large changes in hardness, the percent area reduction drops considerably on initial aging for 1 min but remains fairly constant afterwards. Similar variation in percent area reduction has been observed [29] even in the case of 480° C aging, as shown in Fig. 12. The variation in erosion rate with BHN is shown in Fig. 13 for both the aging temperatures. It is noted that whereas with aging for 1/2 min the hardness increases by a large amount (20% for 480° C and 42% for 590° C), the change in erosion rate is negligible. With further aging the erosion rate increases at a rapid rate along with increasing hardness until the maximum hardness is reached. When overaging occurs, as is the case for 590° C aging temperature, the erosion rate decreases along with the decrease in hardness. It is, thus, obvious that hardness as a strength parameter affects erosion rate significantly past the minimum aging time of 1/2 min. The variation of erosion rate with ductility alone (ignoring strength), as often cited in the literature, is thus not realistic.

The variation of erosion rate with ductility, while keeping the hardness constant, was studied by cold rolling

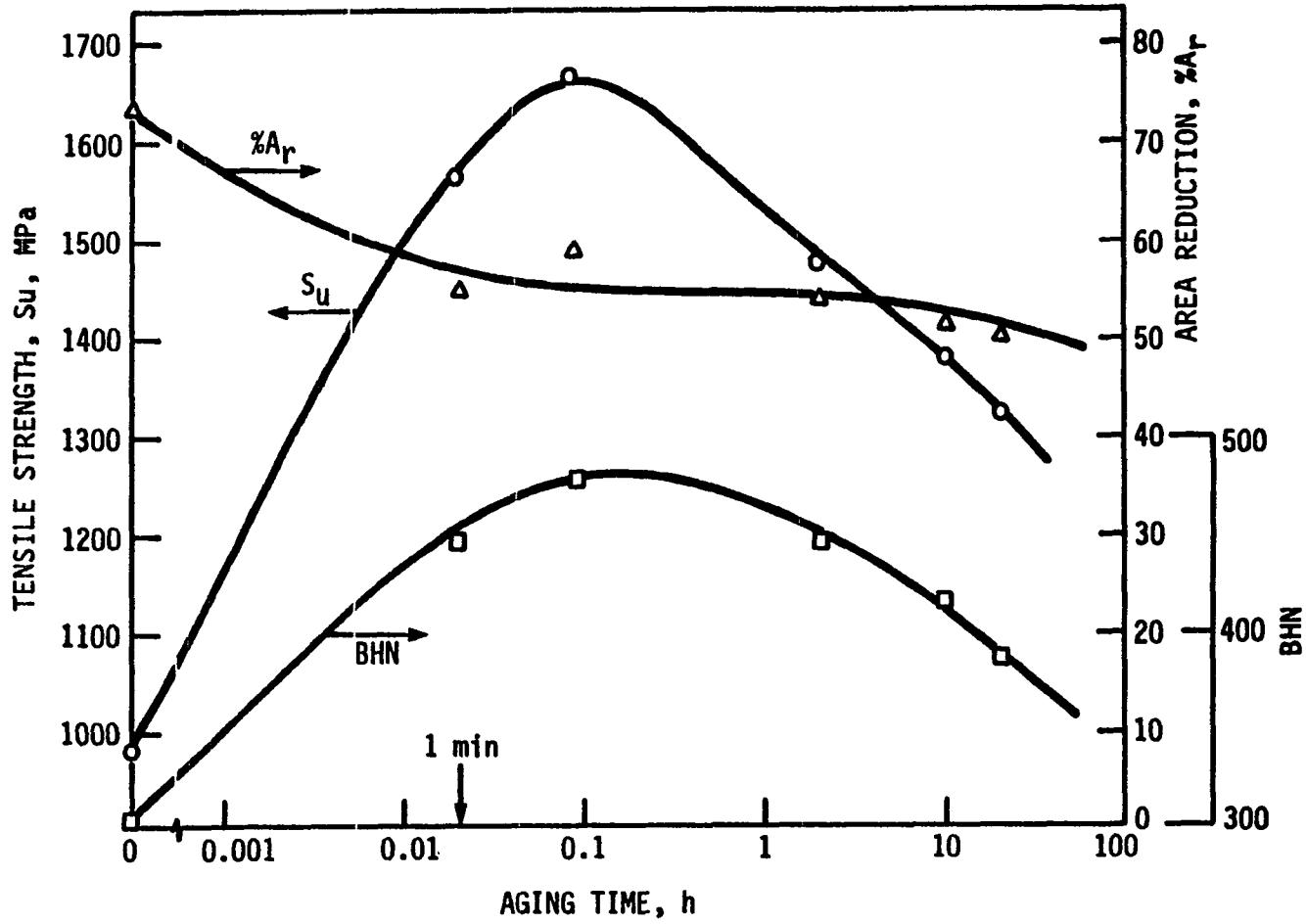

FIGURE 11. Mechanical properties of 18 Ni (250) maraging steel aged at 590° C

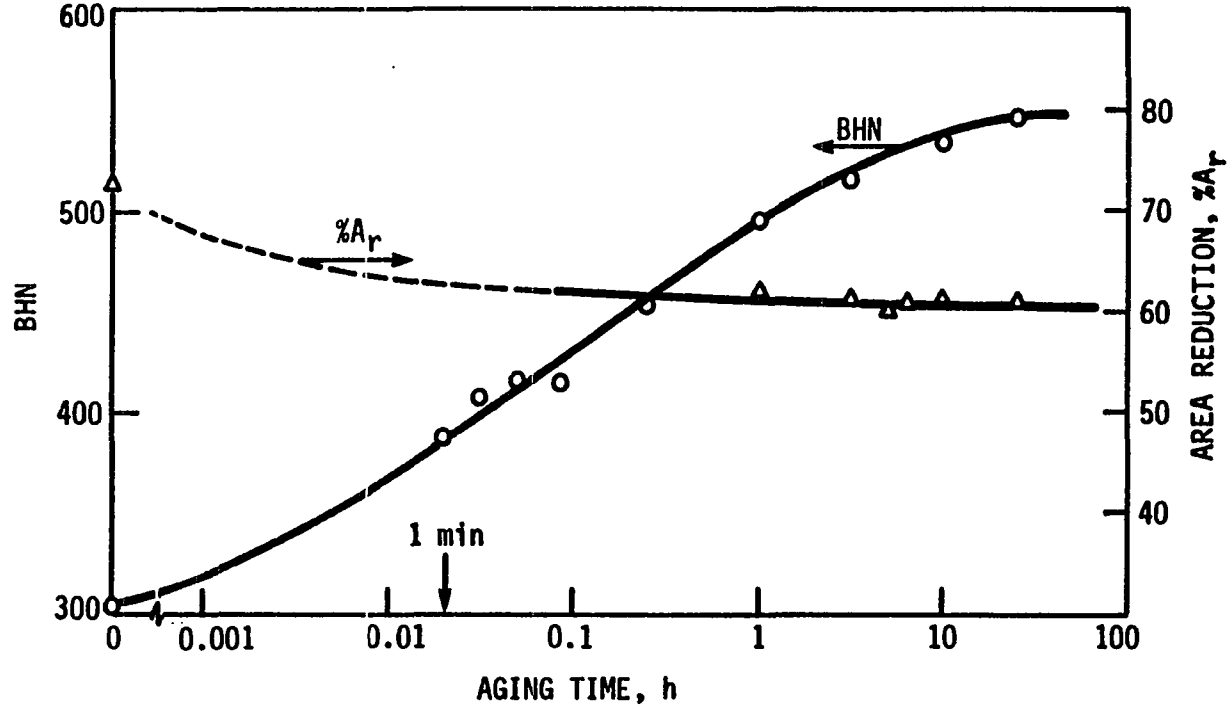

FIGURE 12. Mechanical properties of 18 Ni (250) maraging steel aged at 480° C. Percent area reduction data from Reference [29]. Dotted part extrapolated

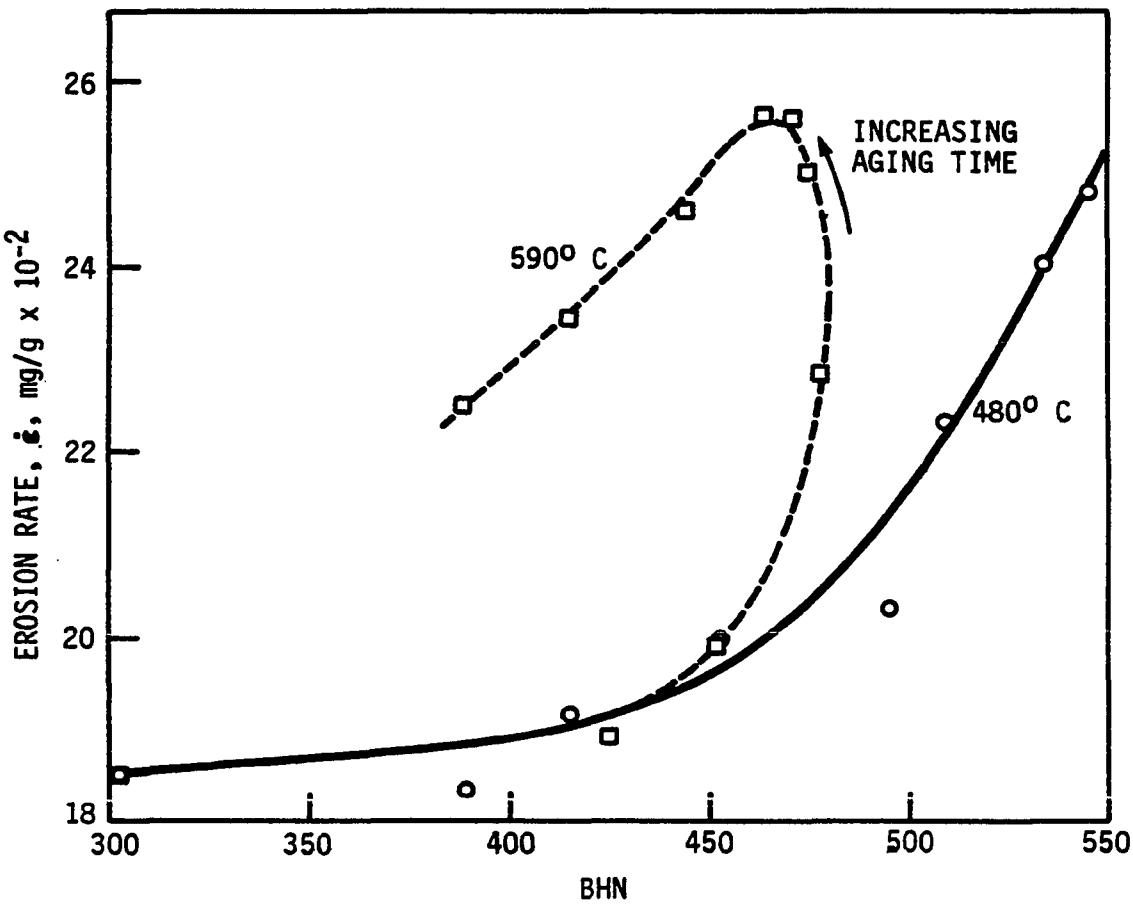

FIGURE 13. Variation of erosion rate with Brinell hardness for aging temperatures of 480° C and 590° C

the material in the solution treated condition. Since maraging steel has a very low strain hardening exponent of 0.025, cold working did not change the hardness by any significant amount even though the ductility was changed considerably. The percent area reduction data along with the hardness for percent cold work values of 9, 18, 35, 45, 52, 65, and 83 are given in Fig. 14. It also shows the erosion values for the corresponding cold work conditions. Whereas the hardness remains fairly constant for 18% to 83% cold work, the percent area reduction changes from 72% to 54%. For these conditions of constant hardness, the erosion rate has been plotted against percent area reduction in Fig. 15. It shows that the erosion rate increases very rapidly with increasing cold work (or decreasing percent area reduction) up to about 65% cold work. In this range, the erosion rate, $\dot{\varepsilon}$, was found to be inversely proportional to $(\%\ Ar)^2$.

Erosion Mechanisms

In order to gain some insight into the mechanisms of material removal, scanning electron microscopy was performed on a number of eroded surfaces. It was found that the impact of a stream of angular particles at an angle to a ductile metal surface forms grooves, as shown in Fig. 16.

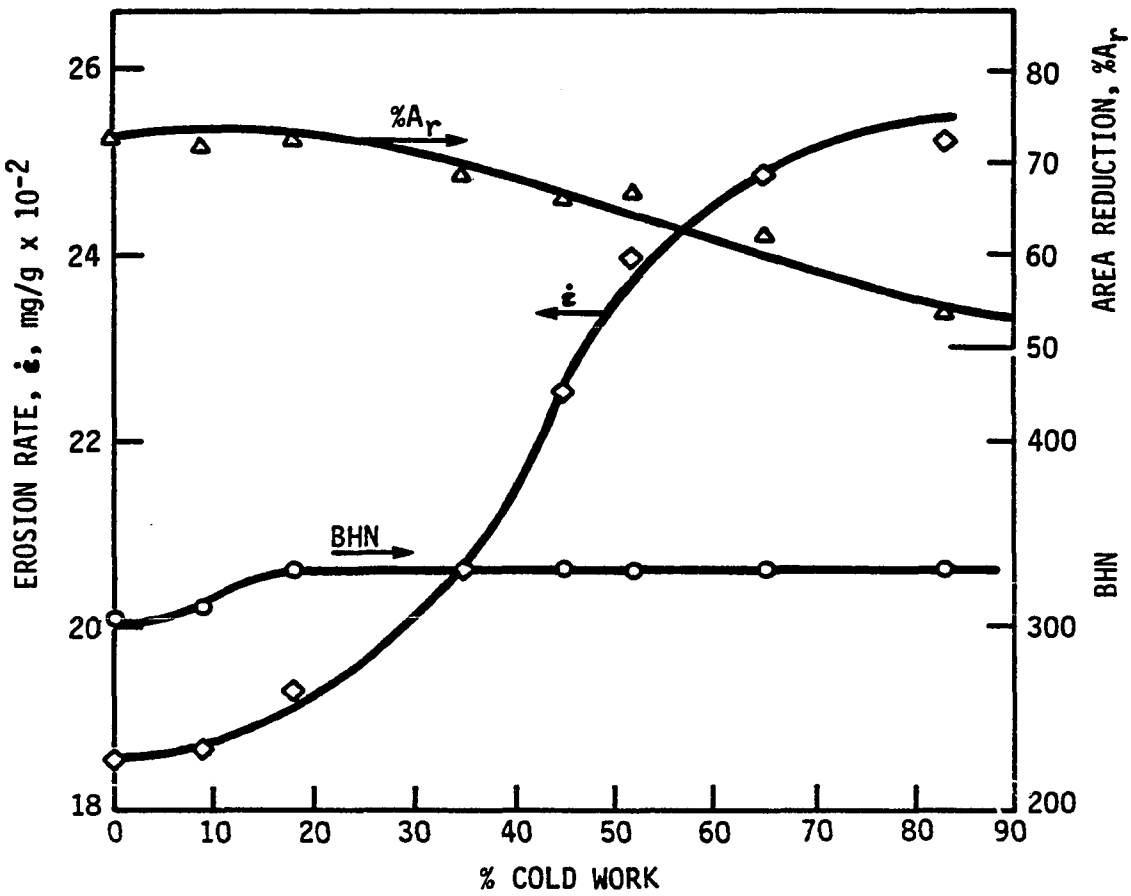

FIGURE 14. Variation of erosion rate, percent area reduction and hardness with percent cold work for maraging steel

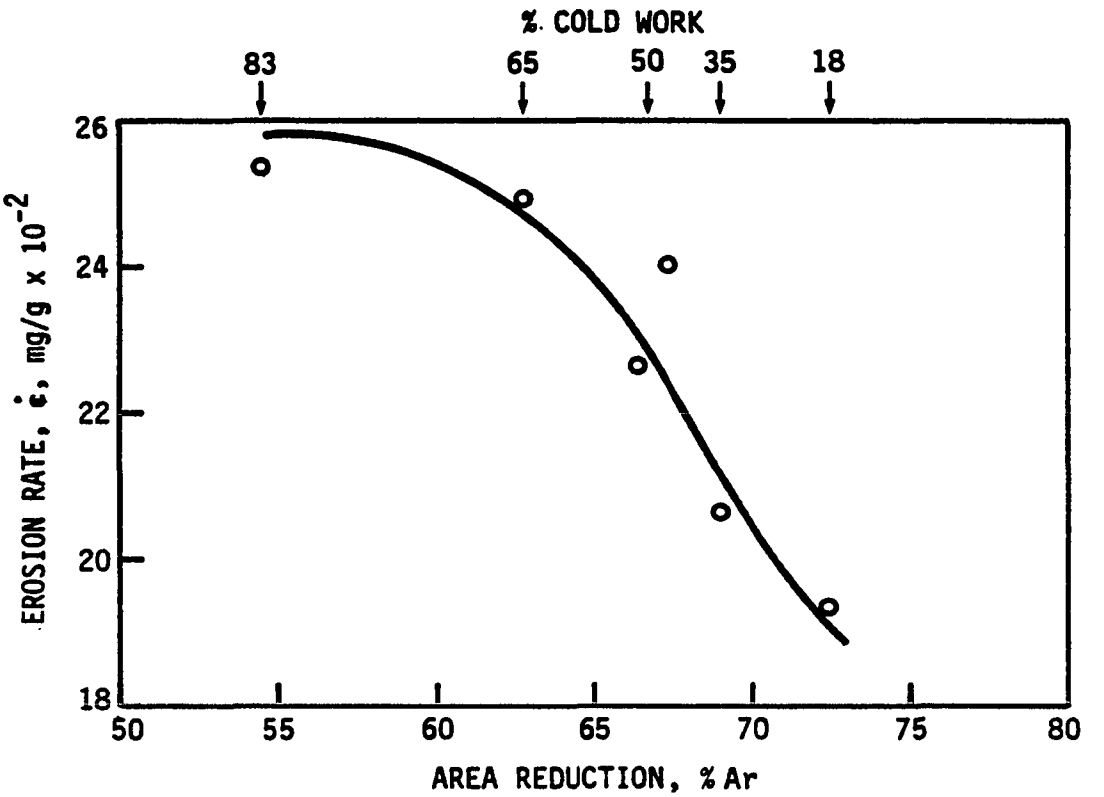

FIGURE 15. Variation of erosion rate with percent area reduction for coldworked maraging steel

These appear to have been formed by a combination of the cutting and plowing action. The latter is evidenced by the pile-up of material around the edges. The eroded surface appears to be covered with loosely attached material. The energy dispersive X-ray analysis and selective dot mapping techniques (see Fig. 17) indicated that some of the impacting particles were imbedded in the target surface and possibly acted as barriers to subsequent erosion in their locations. The fragmentation of impacted particles was also an operative mechanism which was determined by the sieve analysis technique. It provided that about 9% of the particles, originally 125 μm in size, were fragmented down to a size of 100 μm and about 16% down to 88 μm or finer. Since fragmentation would increase the number of particles, while increasing their sharpness, interacting with the target surface, erosion will be increased.

The micrograph in Fig. 18 provides evidence of cutting in some locations and considerable plastic deformation elsewhere. This deformation produces extrusion of the target material in the form of thin overlapping layers which present the appearance of flakes. The examination of these flakes at higher magnification revealed flow of the ductile material (see Fig. 19) as inferred from their smooth profiles. It is essentially a layered structure as would be

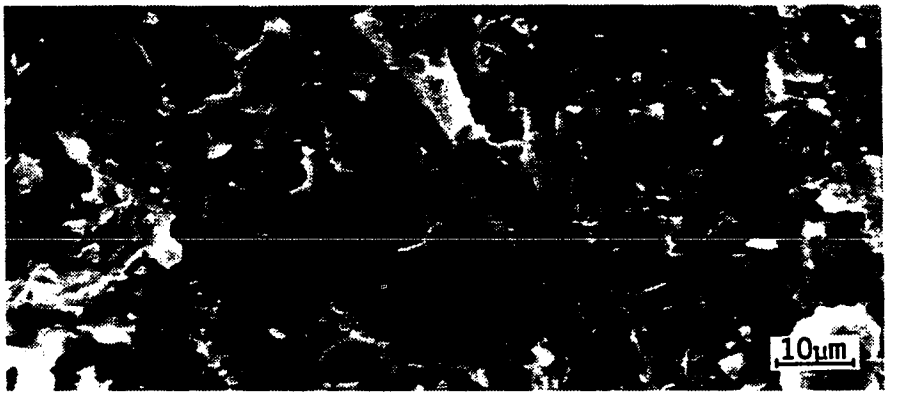

FIGURE 16. Scanning electron micrograph of an eroded surface showing a groove with extruded lips

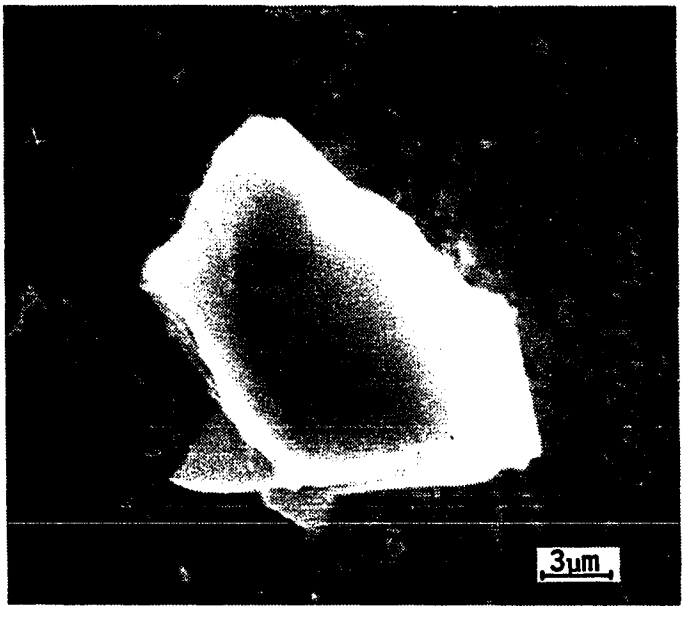

(a)

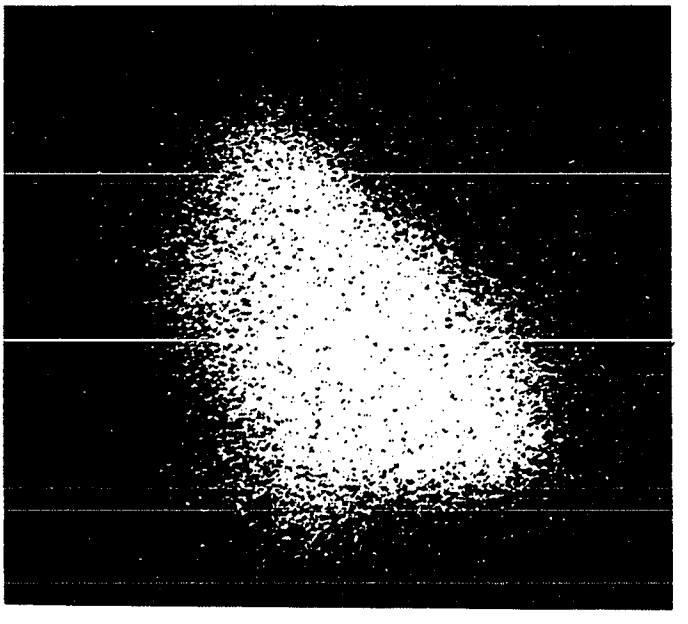

(b)

FIGURE 17. Scanning electron micrographs showing a SiC particle embedded in the eroded surface (a), and selective Si dot mapping of energy dispersive X-rays (b)

formed by successive impacts at the same location because the edges of these layers have random contours. The excessive deformation in the regions adjoining these edges is responsible for the cracks that appear in the flake transverse to the direction of maximum tensile stress. The growth of these cracks results in the detachment of flakes from the eroded surface.

Erosion debris were also examined by electron microscopy. Figure 20 shows the deformation features on the surface of the debris that was detached from the substrate. It shows considerable plastic deformation in the material at the detachment level, flaky structure, and even a large crack running through it.

From the above analysis of the eroded surfaces and the debris, it is concluded that the target material is eroded by a combination of cutting, plowing, and crack propagation mechanisms where the latter two appeared to be the dominating modes.

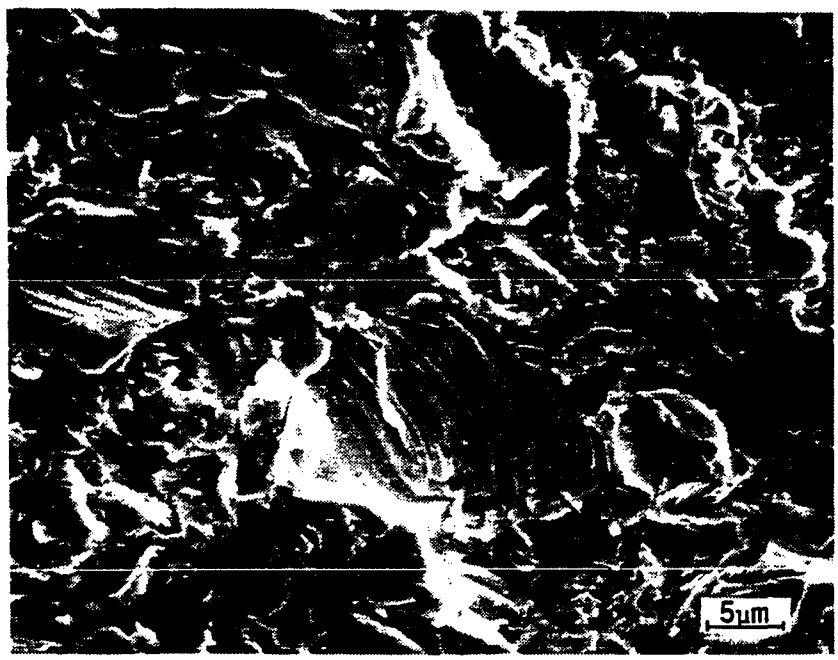

FIGURE 18. Scanning electron micrograph showing cutting, plastic deformation, and flake generation on an eroded surface

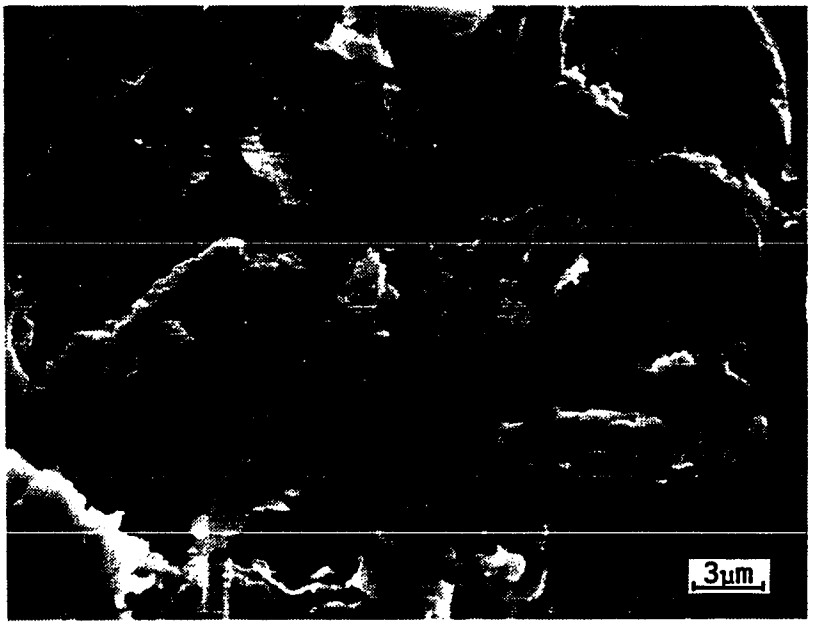

FIGURE 19. Scanning electron micrograph showing flakes along with cracks in them

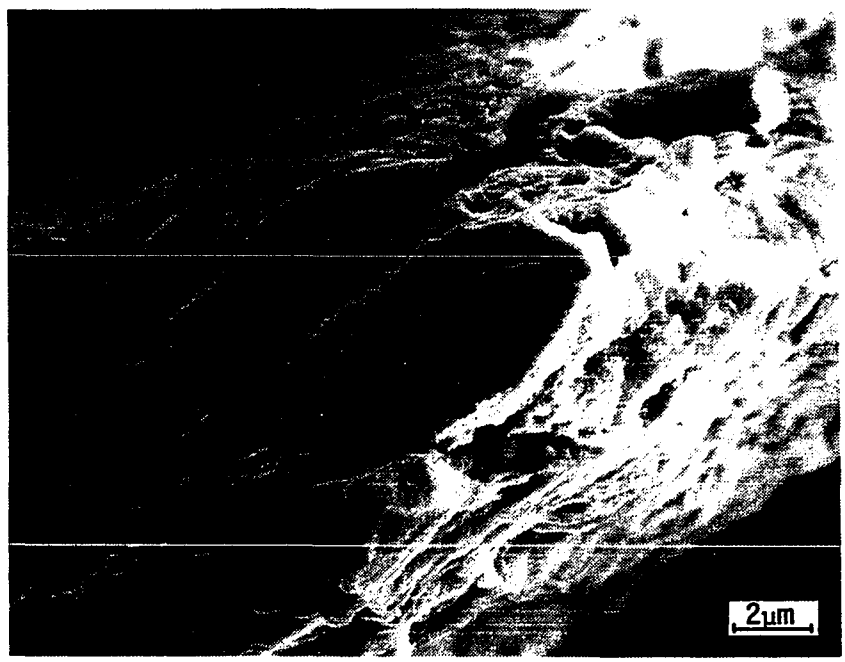

FIGURE 20. Scanning electron micrograph of an erosion debris

CONCLUSIONS

Erosion of 18 Ni (250) maraging steel is related to its aging behavior which may be divided in three zones. In Zone I hardness increases because of the precipitate formation and so does the erosion rate. In Zone II along with precipitation austenite reversion occurs and the net effect is softening of the matrix and leveling of the erosion rate. In Zone III increased reversion of austenite and particle growth decrease hardness along with the erosion rate.

The erosion rate varies directly with hardness when ductility remains unchanged during precipitation hardening. It was also found to vary inversely with the square of percent area reduction when the hardness remained constant. It shows that hardness and ductility both affect the erosion resistance of a material.

Erosion involves considerable plastic deformation in the substrate. The material is detached in the form of multilayered flakes because of a combination of cutting, plowing, and crack propagation mechanisms.

ACKNOWLEDGEMENT

The research was supported by the Engineering Research Institute of Iowa State University.

REFERENCES

1. Finnie, I. "Erosion of Surfaces by Solid Particles." Wear 3 (1960): 87-103.

2. Bitter, J. G. A. "A Study of Erosion Phenomena: Parts I and II." Wear 6 (1963): 5-190.

3. Neilson, J. H. and Gilchrist, A. "Erosion by a Stream of Solid Particles." Wear 11 (1968): 111-143.

4. Head, W. J. and Harr, M. E. "The development of a Model to Predict the Erosion of Materials by Natural Contaminants." Wear 15 (1970): 1-46.

5. Adler, W. F. "Analytical Modeling of Multiple Particle Impacts on Brittle Materials." Wear 37 (1976): 353-364.

6. Jennings, W. H., Head, W. J. and Manning, C. R., Jr. "A Mechanistic Model for the Prediction of Ductile Erosion." Wear 40 (1976): 93-112.

7. Finnie, I., Wolak, J. and Kabil, Y. "Erosion of Metals by Solid Particles." Journal of Materials 2, No. 3 (1967): 682-700.

8. Christman, T. and Shewmon, P. G. "Erosion of a Strong Aluminum Alloy." Wear 52 (1979): 57-70.

9. Salik, J. and Buckley, D. H. "Effect of Mechanical Surface and Heat Treatments on Erosion Resistance." In Wear of Materials - 1981, pp. 592-596. Edited by S. K. Rhee, A. W. Ruff and K. C. Ludema. The American Society of Mechanical Engineers, New York, 1981.

10. Levy, A. V. "The Solid Particle Erosion Behavior of Steel as a Function of Microstructure." Wear 68 (1981): 269-278.

11. Foley, T. and Levy, A. "The Effect of Heat Treatment on the Erosion Behavior of Steel." In Wear of Materials - 1983, pp. 346-353. Edited by K. C. Ludema. The American Society of Mechanical Engineers, New York, 1983.

12. Sargent, G. A., Keshavan, M. K., Mehrotra, P. K. and Conrad, H. "The Erosion of Plain Carbon Steels by Ash Particles from a Coal Gasifier." In Wear of Materials - 1981, pp. 613-618. Edited by S. K. Rhee, A. W. Ruff and K. C. Ludema. The American Society of Mechanical Engineers, New York, 1981.

13. Ives, L. K. and Ruff, A. W. "Transmission and Scanning Electron Microscopy Studies of Deformation at Erosion Impact Sites." In Wear of Materials - 1977, pp. 392-400. Edited by W. A. Glaeser, K. C. Ludema and S. K. Rhee. The American Society of Mechanical Engineers, New York, 1977.

14. Rickerby, D. G. and Macmillan, N. H. "The Erosion of Aluminum by Solid Particle Impingement at Normal Incidence." Wear 60 (1980): 369-382.

15. Naim, M. and Bahadur, S. "Workhardening in Erosion Due to Single Particle Impacts." In Wear of Materials - 1984, pp. 592-596. Edited by K. C. Ludema. The American Society of Mechanical Engineers, New York, 1984.

16. Knight, C. G., Swain, M. V. and Chaudhri, M. M. "Impact of Small Steel Spheres on Glass Surfaces." Journal of Material Science| 12 (1977): 1573-1586.

17. Sheldon, G. L. and Finnie, I. "The Mechanisms of Material Removal in the Erosive Cutting of Brittle Materials." Transactions of the ASME 88B (1966): 393-400.

18. Brown, R., Jun, E. J. and Edington, J. W. "Mechanisms of Erosive Wear for 90° Impact on Copper and Iron Targets." In Wear of Materials - 1981, pp. 583-591. Edited by S. K. Rhee, A. W. Ruff and K. C. Ludema. The American Society of Mechanical Engineers, New York, 1981.

19. Sheldon, G. L. and Kanhere, A. "An Investigation of Impingement Erosion Using Single Particles." Wear 21 (1972): 195-209.

20. Winter, R. E. and Hutchings, I. M. "Solid Particle Erosion Studies Using Single Angular Particles." Wear 29 (1974): 181-194.

21. Tilly, G. P. "A Two Stage Mechanism of Ductile Erosion." Wear 23 (1973): 87-96.

22. Edington, J. W. and Wright, I. G. "Study of Particle Erosion Damage in Haynes Stellite 6B, I: Scanning Electron Microscopy of Eroded Surfaces. II: Transmission Electron Microscopy." Wear 48 (1978): 131-144.

23. Winter, R. E. and Hutchings, I. M. "The Role of Adiabatic Shear in Solid Particle Erosion." Wear 34 (1975): 141-148.

24. Ruff, A. and Ives, L. "Measurement of Solid Particle Velocity in Erosive Wear." Wear 35 (1975): 195-199.

25. Peters, D. T. and Cupp, C. R. "The Kinetics of Aging Reactions in 18 Pct Ni Maraging Steels." Transactions of the Metallurgical Society of AIME 236 (1966): 1420-1429.

26. Miller, G. P. and Mitchell, W. I. "Structure and Hardening Mechanisms of 18% Nickel-Cobalt-Molybdenum Maraging Steels." Journal of the Iron and Steel Institute 203 (1965): 899-904.

27. Peters D. T. "A Study of Austenite Reversion During Aging of Maraging Steels." Transactions of the ASM 61 (1963): 62-74.

28. Cheng, I-Lin and Thomas, G. "Structure and Properties of Fe-NiCo-Ti Maraging Steels." Transactions of the ASM 61 (1968): 14-25.

29. 18% Nickel Ultra High Strength Maraging Steels: VanadiumAlloys Steel Company (VASCO), Latrobe, PA, 1966.

PAPER 2:

EROSION OF PRESTRAINED AND AGED 2024 ALUMINUM ALLOY

ABSTRACT

Specimens of 2024 aluminum alloy were solution treated and aged at 190° C for varying times up to a maximum of 100 hours. Solution annealed specimens were also strained to 3% and 6% prior to aging. The erosion behavior of these specimens was studied in a sand-blast type test rig. The tests were conducted under ambient conditions with 125μm angular silicon carbide particles impacted with a velocity of 50 m/s and at an angle of 30° to the specimen surface. Erosion behavior has been studied with respect to the variations in microstructure and the resulting mechanical properties. It is found that aging with prior straining results in higher hardness and also in higher erosion rate. Furthermore, erosion rate decreases with the increase in ductility as well as precipitate size during aging.

INTRODUCTION

The effect of microstructure and mechanical properties on the erosion resistance of 2024 aluminum alloy was studied because it is extensively used in many components of aircrafts, missiles, and spacecrafts. The examples of parts subjected to erosive environments include aircraft baffles, deflectors, wing skins, cowls, engines, propellers, skin of helicopter rotors, and the skin of supersonic military aircraft wings. The reason for the extensive use of this alloy in these devices is its high strength-to-weight ratio. The alloy is commonly precipitation hardened which results in a significant increase in strength. Straining prior to aging introduces excess vacancies and dislocations. This results in increased diffusion and precipitation, which further contributes to enhanced strength.

All of the erosion investigations on 2024 aluminum alloy [1 - 4] have been performed with the main objective of determining the effect of impact conditions on erosion, and the results of some of these these studies are described below. Grant and Tabakoff [1] eroded annealed 2024 aluminum with alumina particles of 110 μm size at various velocities and angles of impact. They found that the angle of impact α for maximum erosion was between 20 and 30 degrees for all of the velocities tested. Their data for the 20° impact angle

indicated that the velocity exponent in the erosion-velocity proportionality relationship was approximately 2.8. At 90° impact angle, the velocity exponent was found to be of the order of 4. This is the highest value of exponent reported in the literature, and has been attributed by these workers to the aerodynamic effects developed in the wind tunnel erosion test facility used in their experiments. Tabakoff et al. [3] also arrived at similar conclusions when they eroded 2024 aluminum with coal ash particles instead of alumina particles as used in earlier studies.

Smeltzer et al. [4] studied the erosion of this aluminum alloy in the annealed and "fully heat treated" condition. The heat treatment increased the hardness from 10 to 49 RA and the yield strength from 100 to 400 MPa. They found that the annealed target eroded less than the "fully heat treated" target. Since the weight loss differences were less than 5 percent, they inferred that the flow strength of a target material had little bearing on its erosion resistance. Instead the small differences in erosion rates were due to high pressure and temperature at the impact location which erased the effect of heat treatment.

High temperature erosion studies [4,5] have shown that the erosion rate may increase or decrease with temperature,

depending upon the angle of particle impingement and test temperature. Smeltzer et al. [4] found that the maximum erosion rate occurred between the impact angles.of 30 to 37.5°, and the erosion rate at elevated temperatures was more severe than at room temperature at impact angles higher than 37.5°. They concluded that the test temperature and particle velocity had unpredictable complex effects upon erosion. Gat and Tabakoff [5] also showed that at oblique impact angles the erosion rate of 2024 aluminum decreased with increasing temperature, but at normal impact angle the erosion rate increased. From the literature, it is still uncertain whether the erosion-temperature relation is a property of the material or of the impact conditions.

In terms of the erosion mechanisms in this alloy, the phenomena of ripple formation and intense plastic deformation have been reported. There are hints of surface melting and lack of micromachining [4], but the conclusive evidence of these aspects is still lacking in the literature.

The microstructure and mechanical properties of 2024 aluminum alloy have been well documented [6], but the effect of the variation in these on erosion rate has not been fully studied. In view of the above, experiments were designed in this work to evaluate the erosion resistance of this alloy

in aged and overaged conditions. The material was also strained prior to aging. The erosion behavior has been related to microstructure and mechanical properties resulting from the thermal and thermomechanical treatments.

EXPERIMENTAL

The specimens were cut from flats, 6 mm thick and 25 mm wide, of commercially available 2024 aluminum alloy. The size of the erosion specimens was 6 mm x 19 mm x 25 mm. The opposite flat surfaces of the erosion specimens were ground parallel and the tensile specimens were machined. It is at this stage that the specimens were heat treated. For solution treatment the specimens were held in a furnace for 1 h at 490° C and then water quenched. Aging was done subsequently at 190± 5° C for varying lengths of time up to a maximum of 100 hours. In some cases, the specimens immediately after solution treatment were stretched to 3% and 6% elongations in a tensile machine and were subjected to aging treatment within an hour of stretching. All the specimens following aging were stored at 0° C and exposed to room temperature conditions for 24 h prior to testing.

The erosion specimens were abraded with emery paper in running water down to a 600 grade finish, and polished with water-suspended alumina particles of 0.3 μm and later 0.05 μm in size. It provided a reference surface roughness of 0.15 to 0.23 μm (rms) for all the erosion experiments.

Erosion tests were performed in a sand- blast type of test rig, described elsewhere in detail [7]. The test rig uses compressed nitrogen gas to accelerate abrasive

particles in a glass tube, 3 mm inside diameter and 300 mm length, and with its end spaced 6 mm from the erosion specimen surface. To minimize any variation in erosion due to the glass tube wear, a new glass tube was used for each erosion target. Angular silicon carbide particles, 125 μm in size, were used as the erodent. All tests were performed at room temperature. The average impact velocity of the erodent was kept constant at 50 m/s, as measured by the double-disk rotating device [8]. The angle of impingement, measured between the target surface and the impacting particles, was fixed at 30° so as to provide near maximum erosion [1,3]. An erosion test involved exposing the specimen to a charge of 20 g abrasive at a time, and to a total of 100 g in five increments of 20 g each. After each exposure, the specimen was removed from its locating fixture, brushed off lightly, and weighed to determine the mass loss due to erosion. The slope of the linear regression line fitted thru the data plot of the target mass loss versus the abrasive mass impacted represents the erosion rate, $\dot{\varepsilon}$, in mg of mass loss per g of abrasive impacted. The correlation coefficient was found to be higher than 0.998 in all the cases.

RESULTS AND DISCUSSION

Figure 1 shows the variation of hardness with aging time for 3% and 6% prestrained specimens, and also for specimens with no prestrain. The minimum prestrain of 3% was selected because this has been shown to be the critical degree of cold work for affecting the precipitation timing in this alloy [9]. When deformation in excess of this critical value is applied, it introduces a large number of vacancies along with dislocations. The latter act as precipitate nuclei and the vacancies promote diffusion. Thus a prestrain of 3% and higher results in earlier precipitation. The effect of this is reflected in the variation of hardness. It is seen in Fig. 1 that for all the conditions hardness increases rapidly after an aging time of 0.5 h, reaches a maximum and then decreases. For the specimens aged without prior straining, the hardness increases from 135 VHN to a maximum of 158 VHN in 10 h of aging time. For the specimens aged after 3% strain, a peak hardness of 166 VHN is reached after 9 h of aging and for the specimens aged after 6% strain, the peak hardness is 173 VHN after 6 h of aging. Thus, straining prior to aging results in higher hardness for any aging time, and the larger the prestrain, the earlier the peak hardness is reached on aging treatment.

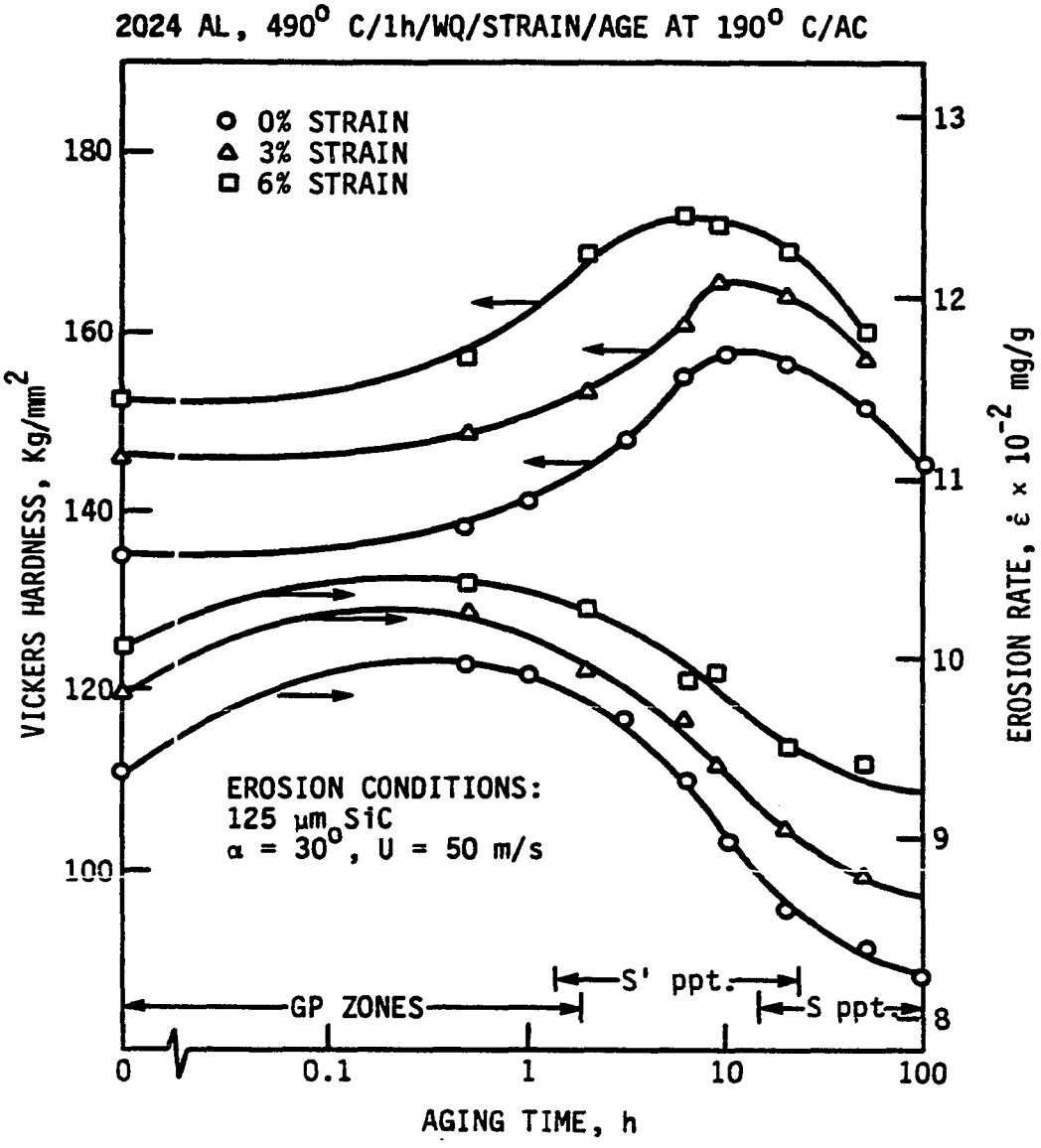

FIGURE 1. Variation of hardness and erosion rate with aging time for 2024 aluminum strained prior to aging at 190° C

The variation of erosion rate with aging time for the above prestrain conditions is also shown in Fig. 1. It is noted that in all the cases the erosion rate increases with aging time up to about 0.5 h but decreases with further aging. A higher value of the prestrain results in a higher erosion rate for any aging time. The maximum value of erosion rate occurs at an aging time of 0.5 h whereas the maximum hardness is obtained with aging times of 10 h, 9 h, and 6 h for prestrain values of 0, 3, and 6%, respectively. Figure 2 which has been replotted from Fig. 1 shows the variation in erosion with target hardness. The dotted parts of the curves represent conditions corresponding to the supersaturated solid solution and very short aging times. Since the erosion rate both increases and decreases with increasing hardness, a direct or inverse proportionality relationship of erosion rate with hardness alone is out of question.

As erosion involves localized plastic deformation [4,7], the variation of erosion rate with tensile strength and percent area reduction of the target material was also examined. The variation of tensile strength with aging time is shown in Figure 3. Similar to hardness, the tensile strength also increases more rapidly on aging when the specimens are prestrained than when they are not. The

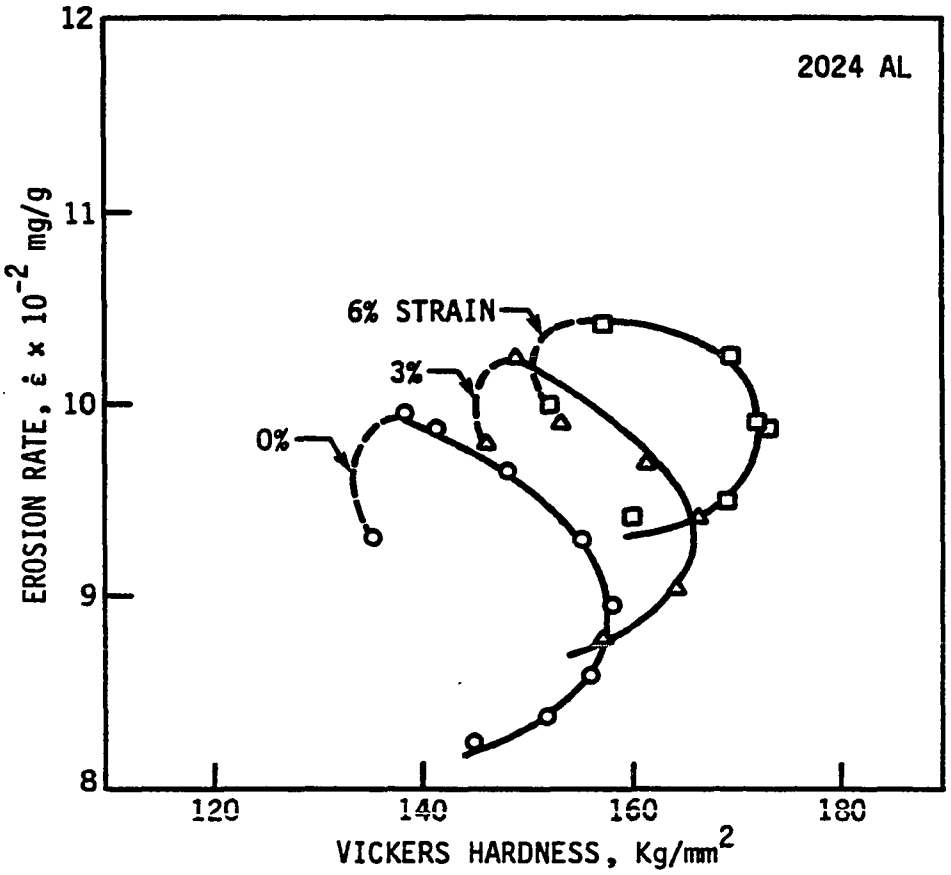

FIGURE 2. Variation of erosion rate with target hardness for 2024 aluminum

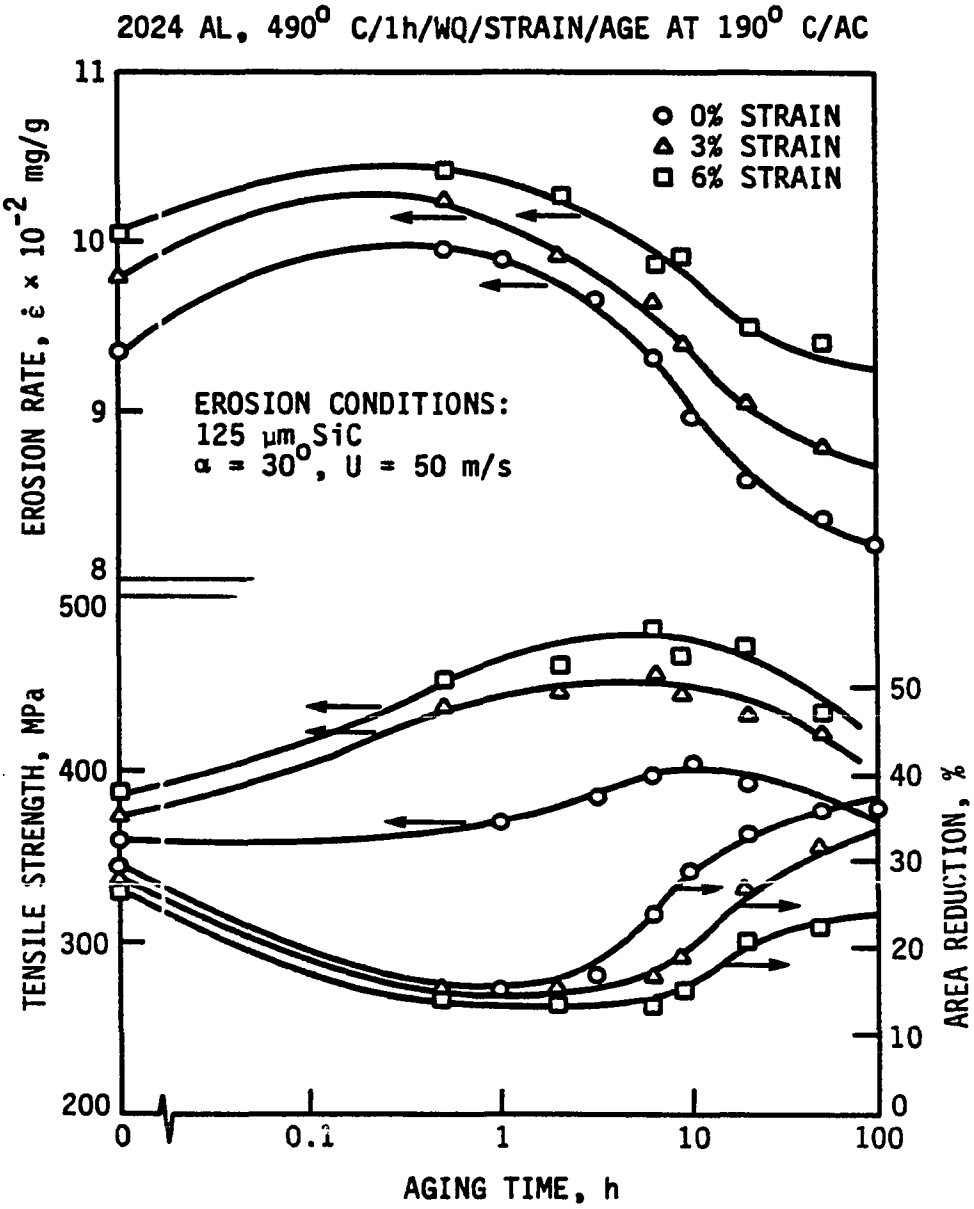

FIGURE 3. Comparison between the variation of erosion rate and tensile properties for thermomechanically treated 2024 aluminum

maximum increase in tensile strength is about 13% in 10 h aging with no prior straining, whereas the corresponding increases are 27% and 34% for 3% and 6% prestrains reached after 6 h and 5 h aging, respectively. Since the variation of tensile strength is in general similar to that of hardness, no direct relation is observed between the tensile strength and erosion rate.

The variation of percent area reduction as a function of the thermomechanical treatments is also shown in Fig. 3. It decreases in the initial aging period of 1 h and then increases after aging times of 5 to 10 h. The prestraining results in a slight reduction of ductility for any aging time. Since the decrease in ductility implies less deformation of material needed for its removal from the substrate, percent area reduction (% Ar) and erosion rate show inverse relationship, $\dot{\varepsilon} \propto 1/ (\% \text{ Ar})^{0.68}$. It is shown more clearly in Fig. 4 but the problem is that for some percent area reduction values two erosion rates appear possible. It is felt that this ambiguity arises because of the additional complication from residual tensile stresses induced in the solution treated specimens due to water quenching. The portion of curves pertaining to this state are shown dotted in the figure.

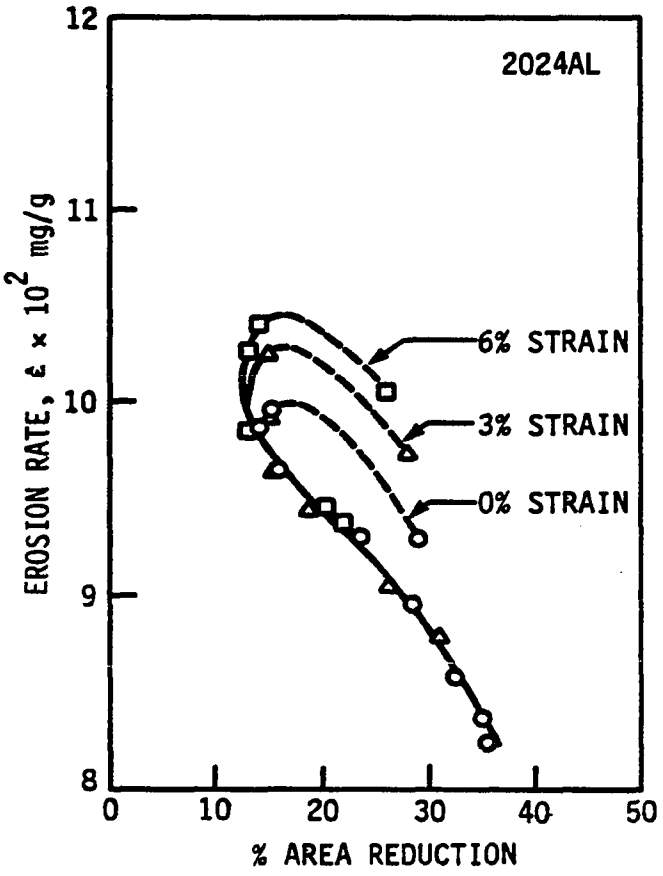

FIGURE 4. Variation of erosion rate with percent area reduction

The variation of erosion rate with microstructural changes during aging is also shown in Fig. 1. In the early stages of aging, the Gunier Preston (GP) zones of copper and magnesium atoms collected on the {110} aluminum planes are formed [10-12]. With increasing aging times, the growth of GP zones is accelerated, but their form and size are not known. A rapid increase in hardness on further aging occurs due to the formation of incoherent metastable S'(Al_2CuMg) precipitates [6]. These are nucleated heterogeneously at dislocations and grow as laths on the {210} aluminum planes in the (001) direction [13]. The decrease in hardness during later stages of aging is due to the coarsening of precipitates to stable condition S (Al_2CuMg). Briefly speaking, the erosion rate increases as the GP zones grow in size and decreases as the S' precipitates are formed and get coarser with overaging finally transforming to S phase.

The variation of erosion rate with precipitate size is shown in Fig. 5. Here the data on precipitate size were taken from Broek and Bowles [9] and the numbers indicate the prestrain and aging conditions as specified. It is noted that the precipitate size increases from 1600 Å to 3000 Å when the undeformed material is overaged beyond maximum hardness. In the 3% and 6% strained conditions, the precipitate size is smaller because of the presence of

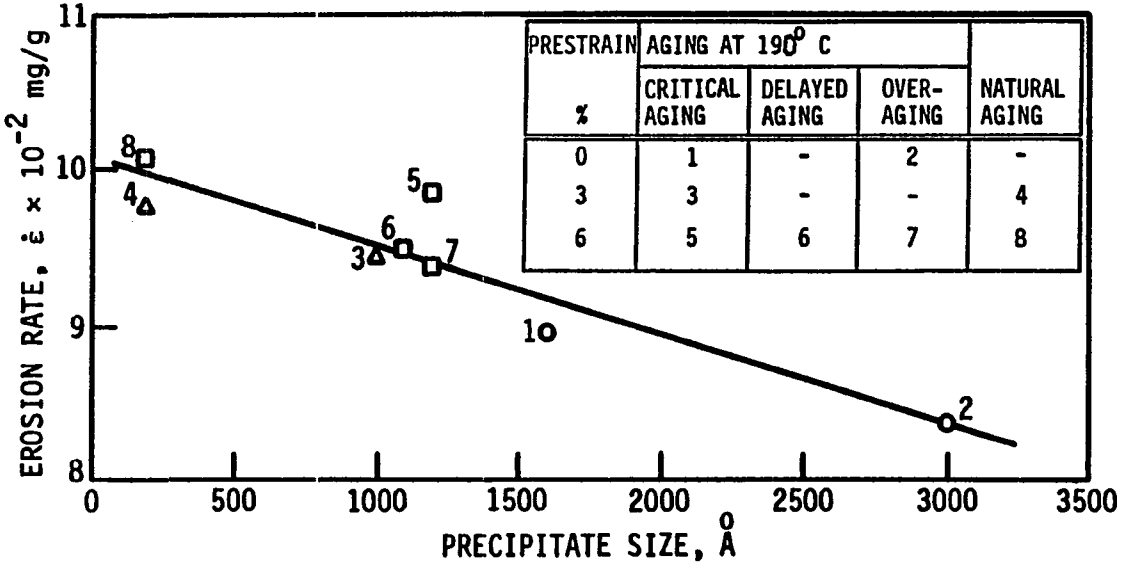

FIGURE 5. Variation of erosion rate with precipitate size for 2024 aluminum. Data on precipitate size from Broek and Bowles [9]. The insert shows the conditions corresponding to different data points

increased number of dislocations which act as nucleation sites. There is an inverse linear relationship between the erosion rate and precipitate size. It is so because, as pointed out by Jahanmir [14], subsurface microvoid and microcrack nucleation determine the erosion rate of ductile metals having hard inclusions or second phase particles. Thus a material containing larger precipitates will have fewer microcracks than the one with smaller particles and will, therefore, show higher erosion resistance. These precipitates cannot restrain the sliding motion of the impacting particles, and localized large plastic deformation results. As the precipitates grow on overaging, dislocation cannot cut thru the precipitates. Because the dislocations cannot move easily, the plastic deformation is reduced. Also the sliding motion of the impacted particles is restrained by the presence of large precipitates and the erosion rate is decreased. As the increase in precipitate size on overaging is also accompanied with an increase in ductility and a decrease in hardness, the effect of precipitate size on erosion is not exclusive.

CONCLUSIONS

The following conclusions were made regarding the erosion behavior of prestrained and aged 2024 aluminum alloy:

(1) Aging with prior straining results in higher hardness and higher erosion.

(2) Higher amounts of prestrain increase the hardness and the erosion rate for any aging time.

(3) Erosion rate is not a unique function of hardness or tensile strength, but it is inversely proportional to $(\% \text{ Ar})^{0.68}$ for aged specimens.

(4) Erosion rate also decreases with increased precipitate size during aging.

REFERENCES

1. Grant, G. and Tabakoff, W. "Erosion Prediction in Turbomachinery Resulting from Environmental Solid Particles." Journal of Aircraft 12, NO. 5 (1975): 471-478.

2. Gat, N. and Tabakoff, W. "Some Effects of Temperature on the Erosion of Metals." Wear 50 (1978): 85-94.

3. Tabakoff, W., Kotwal, R., and Hamed, A. "Erosion Study of Different Materials Affected by Coal Ash Particles." Wear 52 (1979): 161-173.

4. Smeltzer, C. E., Gulden, M. E. and Compton, W. A. "Mechanisms of Metal Removal by Impacting Dust Particles." Journal of Basic Engineering 92 (1970): 639-654.

5. Gat, N. and Tabakoff, W. "Effects of Temperature on the Behavior of Metals Under Erosion by Particulate Matter." Journal of Testing and Evaluation 8, NO. 4 (1980): 177-186.

6. Hunsicker, H. Y. "The Metallurgy of Heat Treatment." In Aluminum Vol. 1, pp. 109-162. Edited by K. R. Van Horn. American Society for Metals, Metals Park, Ohio, 1967.

7. Naim, M. and Bahadur, S. "Effect of Microstructure and Mechanical Properties on the Erosion of 18 Ni (250) Maraging Steel." In Wear of Materials-1985, pp. 586-594. Edited by K. C. Ludema. The American Society of Mechanical Engineers, New York, 1985.

8. Ruff, A and Ives, L. "Measurement of Solid Particle Velocity in Erosive Wear." Wear 35 (1975): 195-199.

9. Broek, D. and Bowles, C. Q. "The Effect of Precipitate Size on Crack Propagation and Fracture of an Al-Cu-Mg Alloy." Journal of the Institute of Metals 99 (1971): 255-257.

10. Preston, G. D. "The Diffraction of X- Rays by Age-Hardening Alloy of Aluminum and Copper Alloys." Proceedings Royal Society of London 167 A (1938): 526-538.

11. Silcock, J. M. "The Structural Ageing Characteristics Al-Cu-Mg Alloys with Copper: Magnesium Weight Ratios of 7:1 and 2.2:1." Journal of the Institute of Metals 89 (1960-61): 203-210.

12. Hardy, H. K. "The Ageing Characteristics of Some Ternary Aluminum- Copper- Magnesium Alloys with Copper: Magnesium Weight Ratios of 7:1 and 2.2:1." Journal of the Institute of Metals 83 (1954-55): 17-34.

13. Wilson, R. N. and Patridge, P. G. "The Nucleation and Growth of S' Precipitates in an Aluminum- 2.5% Copper- 1.2% Magnesium Alloy." Acta Metallurgica 13 (1965): 1321-1327.

14. Jahanmir, S. "The Mechanics of Subsurface Damage in Solid Particle Erosion." Wear 61 (1980): 309-324.

PAPER 3:

EFFECT OF PRECIPITATED AND DISPERSED HARD PARTICLES ON EROSION

ABSTRACT

The effect of precipitated hard particles on erosion was studied using 2011 aluminum alloy and that of dispersed hard particles by dispersing alumina particles in a phenolic resin. The specimens of aluminum alloy were solution treated and aged at two different temperatures for varying lengths of time in order to obtain precipitates in varying sizes and densities. The alumina dispersed phenol formaldehyde specimens were also prepared with alumina particles in varying sizes and concentrations. The erosion behavior of these specimens was studied in a sand-blast type test rig. The tests were conducted under ambient conditions with 125 μm angular silicon carbide particles impacted with a velocity of 50 m/s and at an angle of 30° to the specimen surface. Erosion behavior has been examined with respect to the microstructure and mechanical properties. A decrease in erosion rate is measured as the GP zone diameter increases from 100 to 500 Å during aging of the aluminum alloy at 130° C. It also decreases with the increase in size and concentration of alumina particles dispersed in phenol formaldehyde matrix.

INTRODUCTION

The erosion behavior of various precipitation hardening alloys has been reported in the literature. However, most of these studies relate to the variation in erosion with changes in operating parameters like impact angle and impact velocity [1-4] whereas the effect of microstructure and mechanical properties on erosion has been investigated by only a few workers [5-7].

Smeltzer et al. [5] studied the erosion of 2024 aluminum, Ti-6Al-4V, and 17-7 PH stainless steel in the annealed and 'fully heat treated' conditions. They found that erosion weight loss differences were less than 5 percent in these conditions even though the variation in yield strength was considerably large.

Salik et al. [6] studied the effects of mechanical surface treatments and heat treatments on the erosion resistance of 6061 aluminum alloy. They found that the effect of mechanical surface treatments on erosion was limited, because, after the outermost layers had been eroded, the impact of particles resulted in the formation of a surface work hardened layer independent of the initial surface condition. They found that erosion increased with both an increase in hardness due to aging, and a decrease in hardness due to overaging.

Naim and Bahadur [7] studied the erosion of 18 Ni (250) maraging steel in the aged and overaged conditions. For the same experimental conditions as used in this work, they found that for a constant ductility erosion rate increased with increased hardness, and when the ductility increased, erosion rate decreased. An increase in the reverted soft austenite phase also decreased the erosion rate.

Brown and Ayers [8] added 70 μm angular TiC particles into the surface of 6061 aluminum by laser melting. With 70 μm diameter glass spheres impacting perpendicular to the surface at 122 m/s, they found that the composite Al-TiC layer eroded at a rate 50% greater than the basic aluminum alloy. The removal of material occurred due to extensive subsurface fracture of TiC particles and flake formation.

Jahanmir [9] used an approximate elastic-plastic solution to analyze the stresses around particles dispersed in a relatively soft matrix. It led to the prediction of subsurface microvoid formation in regions below the target surface. The formation of the greatest number of voids was shown to coincide with the impingement angle of peak erosion. Arguing that a material containing large particles will have fewer microcracks, he concluded that large precipitates would result in decreased erosion rate. He also pointed out that the interparticle spacing and the

precipitates density were likely to affect the erosion rate by changing the rate of subsurface void nucleation and crack propagation.

The object of this paper was to study how the presence of hard particles in a soft matrix affected the erosion rate. It led to using two systems: a precipitation hardening system such as 2011 aluminum alloy, and a dispersion hardening system where alumina particles were dispersed in a phenolic resin. The particular aluminum alloy was selected because it exhibits a large variation in precipitate size on aging [10-11]. The heat treatment conditions were selected in the light of this information.

EXPERIMENTAL

Erosion and tensile specimens were cut from a commercial grade 2011 aluminum rod of 20 mm diameter. The opposite flat sides of the erosion specimens were ground parallel and The tensile specimens were machined. They were then solution treated at 530° C and aged at 130° C and 190° C for varying lengths of time up to a maximum of 20 days. The specimens after aging were stored at 0° C and were exposed to room temperature for 24 h prior to any testing.

The test surface of the aluminum erosion samples was polished in running water with emery paper in discrete steps down to a 600 grade finish. Final polishing was done on a rotary polishing cloth using water-suspended alumina particles of the size 0.3 μm and later 0.05 μm. It provided a base surface roughness of 0.15 to 0.23 μm rms.

The effect of hard particles dispersed in a soft matrix on erosion was studied by preparing specimens of phenol formaldehyde dispersed with angular alumina particles. They were compression molded at a pressure of 30 MPa and temperature of 150° C. A total of five particle sizes, viz., 44, 53, 74, 100 and 150 μm, were used while maintaining a fixed weight of 5%. The second set of specimens were prepared with a fixed particle size of 53 μm and with varying weight percentages of 1, 2, 3, 4 and 5.

Unlike the aluminum alloy, no surface preparation for erosion specimen was needed in this system.

Erosion tests were performed on erosion specimens, 5 mm thick and 20 mm diameter, in a sand-blast type of test rig, described elsewhere in detail [7]. Compressed nitrogen gas was used to accelerate abrasive particles in a glass tube of 3 mm inside diameter and 300 mm length. The end of the glass tube was spaced 6 mm from the surface of erosion specimen. To eliminate any variation in erosion measurements from the glass tube wear, a new glass tube was used for each erosion target. Angular silicon carbide particles, 125 μm in size, were used as the erodent. All the tests were performed at room temperature and the average impact velocity of the erodent was 50 m/s. The particle feed rate was 20 g/min. The angle of impingement was fixed at 30° to obtain maximum ductile erosion [12].

The erosion tests were performed by exposing an erosion specimen of aluminum alloy to a charge of 20 g at a time and eroding it with a total of 100 g abrasive in five increments of 20 g each. Similarly, the phenolic base erosion specimen was eroded with abrasive in increments of 10 g upto a maximum of 50 g. After every exposure, the specimen was removed from its locating fixture, brushed off lightly, and weighed to determine the mass loss due to erosion. The

latter was plotted against the abrasive mass impacted in grams. The slope of the regression straight line fitted represents the erosion rate, $\dot{\varepsilon}$, in mg of mass loss per g of abrasive impacted. The correlation coefficient was found to be higher than 0.998 in all the cases.

The tensile properties of heat treated aluminum alloy were determined using specimens conforming to the ASTM specification E-8, while the alumina dispersed phenolic specimens were tested in flexure as per ASTM Designation D 790.

RESULTS AND DISCUSSION

Figure 1 shows the variation of Vickers microhardness with aging time for two aging temperatures, 130° and 190° C, for 2011 aluminum alloy. The average hardness was 82 VHN after solution treatment at 530° C. When aged at 130° C, the hardness increases to 125 VHN after an aging period of 5 days, remains constant during the aging period of 5 to 9 days, and increases rapidly again during aging for 20 days. Aging at a higher temperature of 190° C results in a more rapid increase in hardness reaching a maximum of 120 VHN after 1 day and the hardness thereafter decreases continuously during aging over a period of 20 days. The combination of the aging temperatures and times selected thus cover both the aging and overaging treatments.

The variation of erosion rate with aging time is also shown in Figure 1 for the two aging temperatures. It is noted that erosion rate increases initially with increased aging time, reaches a maximum value and drops on subsequent aging. The erosion rate is about the same during aging over a period of 1 day irrespective of the aging temperature though the corresponding hardness values are quite different. The peak erosion rate for 190° C aging temperature coincides with the peak hardness (aging time of 1 day) and the erosion rate decreases afterwards as the

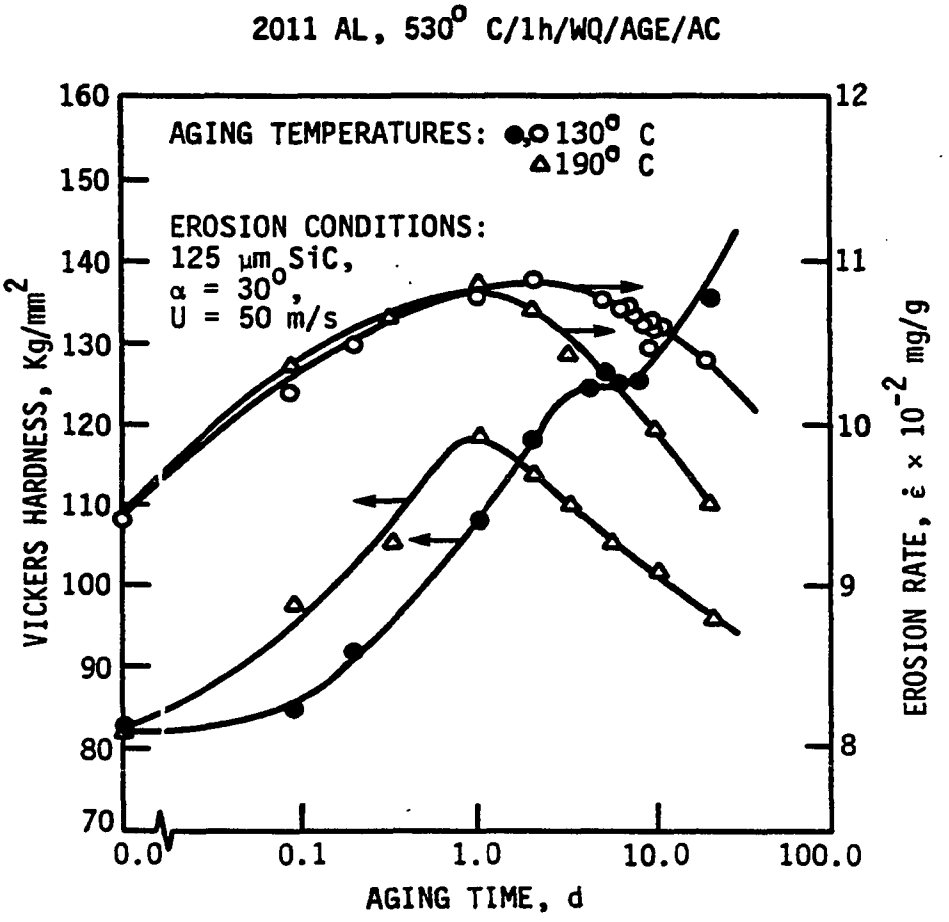

FIGURE 1. Variation of target hardness and erosion rate with aging time for 2011 aluminum alloy aged at 130° C and 190° C.

hardness decreases during overaging. Interestingly enough it is not the case with 130° C aging because erosion rate decreases after reaching a maximum value on aging for 2 days even though the hardness keeps increasing. The erosion rate undergoes a decreasing trend during the aging period of 5 to 9 days when the hardness remains fairly constant. For aging between 1 to 20 days, specimens aged at 190° C erode less than those aged at 130° C. Thus, contrary to the statements by some workers that a direct relationship exists between the erosion rate and target hardness [13,14], the above observation suggests that the variation in hardness alone cannot explain the variation in erosion.

The comparison between the variation of erosion rate and the tensile properties as a function of aging time is presented in Fig. 2. When aged at 130° C, the tensile strength increases from 315 MPa in the solution annealed condition to 380 MPa after 5 days, remains unchanged during aging from 5 to 9 days, and increases further to 415 MPa on aging for 20 days. Aging at 190° C results in a peak tensile strength of 375 MPa after 1 day, and the strength decreases on further aging. It would thus be noted that the variation of tensile strength is similar to that of hardness and so the comments made above with respect to hardness as an indicator of erosion behavior apply here as well.

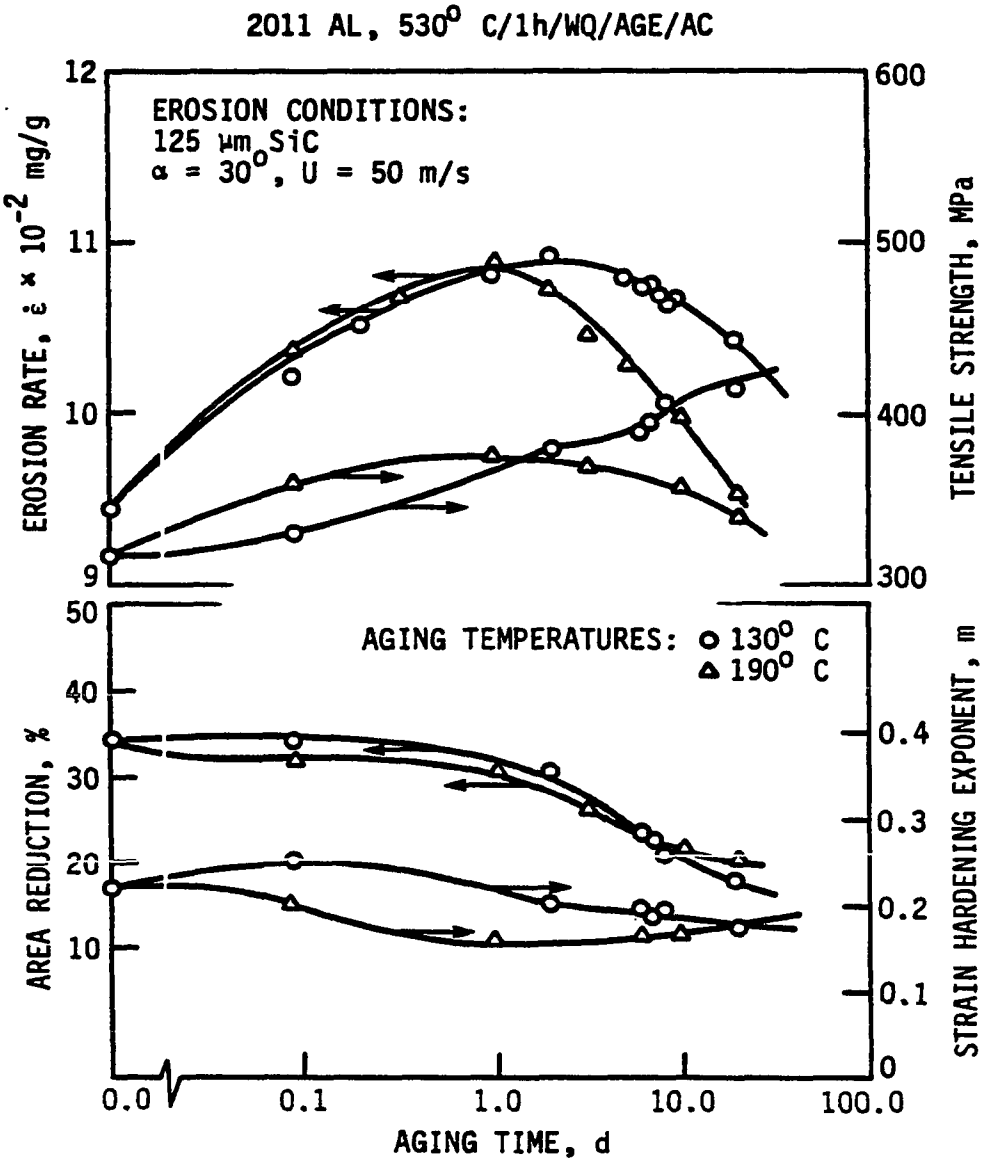

FIGURE 2. Comparison between the variation of mechanical properties and erosion rate for 2011 aluminum alloy aged at 130° C and 190° C

For both aging temperatures, the percent area reduction remains fairly constant upto an aging time of 1 day and decreases with further aging. Thus the variation in erosion rate does not seem to agree with the variation in ductility either [7,14,15].

In an earlier work by one of the authors [16], it was observed that the maximum erosion rate coincided with the maximum value of the the strain hardening exponent for high silicon, 1.0% Mn and 1.0% Ni steels where about 30% retained austenite was being obtained. In view of this, the correlation between strain hardening exponent and erosion rate was tried here as well. The plot in Fig. 2 shows that no such correlation is possible.

The variation in erosion rate is examined in the light of microstructural transformation in Fig. 3 for aging at a temperature of 130° C. Aging results initially in the development of Guinier-Preston (GP) zones which are formed by the segregation of copper atoms in the supersaturated solid solution α [10,11]. GP1 zones consist of copper-rich regions of 4 to 6 Å thick and about 80 to 100 Å in diameter [10]. The increasing number of coherent GP1 zones which account for the initial rise prior to the flat plateau in the hardness curve (Fig. 1) result in increasing erosion rate. At higher aging times, coherent GP2 zones, about 20

to 30 Å thick, are formed and the peak hardness is due to a mixture of GP2 zones and partially coherent θ' platelets about 100 A thick [10,11]. The rapid increase in the zone (specifically GP2) diameter from about 100 Å to 500 Å [10] results in decreasing erosion rate.

Aging at 190° C results directly in the formation of GP2 zones. As aging time is increased, both the number and size of GP2 zones is increased and a rapid increase in hardness is observed [10]. During this stage, the erosion rate increases because of the increased number of GP2 zones. When the peak hardness is reached the alloy contains GP2 zones plus one-third of the possible θ' platelets which are about 80 Å thick. As overaging starts, the GP2 zones disappear and the incoherent θ' forms in significant amounts. The size of the θ' ranges from 80 to 150 Å in thickness and 100 to 600 Å in diameter. Any further increase in aging time decreases hardness due to the formation of equilibrium incoherent θ phase, $CuAL_2$, at the expense of the incoherent θ' phase [10]. With increase in precipitate size during overaging, the erosion rate decreases.

The effect of particle size and concentration on erosion rate was studied directly using a phenolic matrix material dispersed with alumina particles. Figure 4 shows

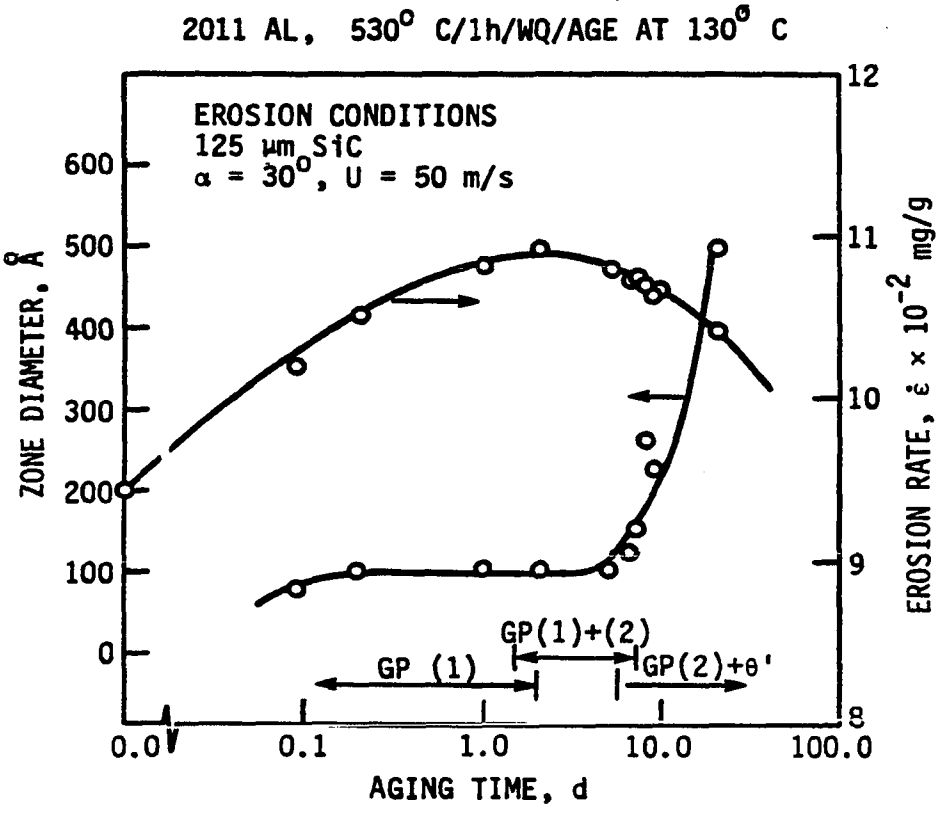

FIGURE 3. Comparison of GP zone diameter and erosion rate

the variation of hardness and erosion rate with particle size for a fixed alumina weight proportion of 5%. The hardness of the specimen containing the smallest size (44 μm) alumina particles is 86 R_E as compared to 82 R_E for the pure phenolic. The decrease in hardness from 86 R_E to 84 R_E, as the alumina particle size is increased from 40 μm to 80 μm, is fairly small and further increase in particle size does not seem to change the hardness. As for the erosion rate, it is maximum with no particles and decreases linearly as the alumina particle size increases. Since the weight percent of alumina is fixed, larger particle sizes result in smaller number of particles in the matrix material. Thus, this observation supports the explanation offered earlier for the variation of erosion rate during the aging of the aluminum alloy. It is also noted that a mere 5 wt. percent alumina of 150 μm particle size resulted in decreasing the erosion rate of the phenolic resin by 30%. Thus the presence of very few particles in a soft matrix is good for decreased erosion rate.

Figure 5 shows the variation of hardness, flexure strength and erosion rate when alumina particles of 53 μm size were dispersed in phenolic resin in varying amounts upto a maximum of 5 wt. percent. As the particle concentration increases from 0 to 3%, the yield strength

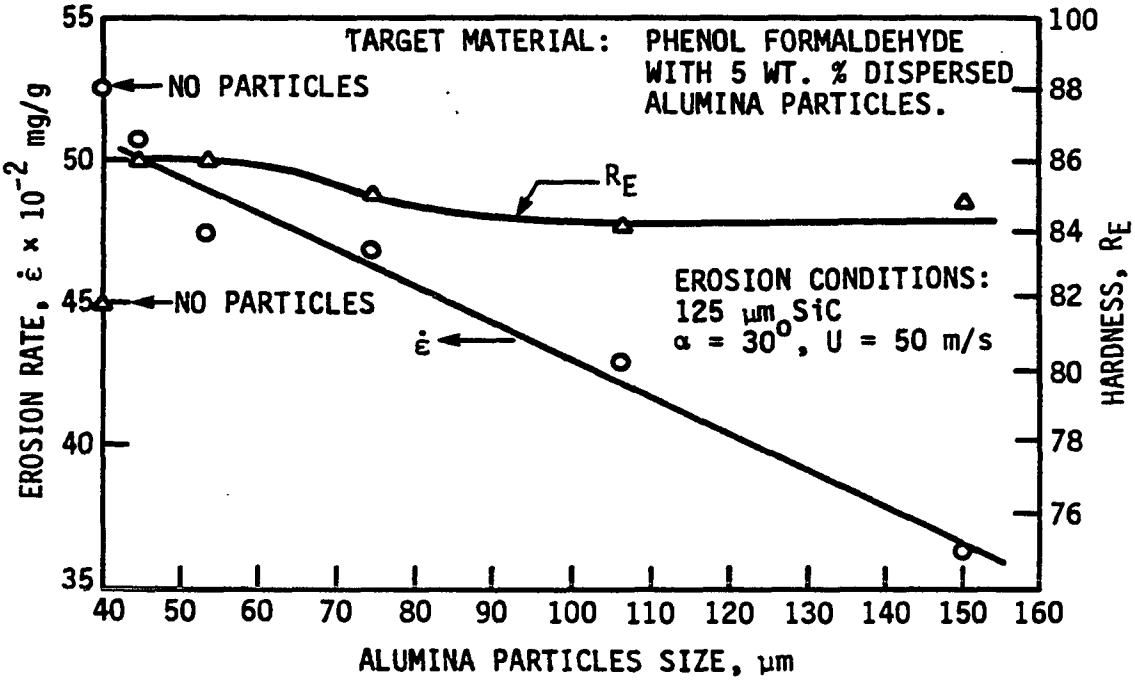

FIGURE 4. Effect of alumina particle size on hardness and erosion rate for alumina dispersed phenol formaldehyde

increases from about 40 to 65 MPa and decreases with higher concentrations. The hardness increases significantly only with more than 3 wt. % alumina. The erosion rate decreases very slightly with increasing particle concentration. Thus the increased particle size is much more effective in decreasing erosion rate.

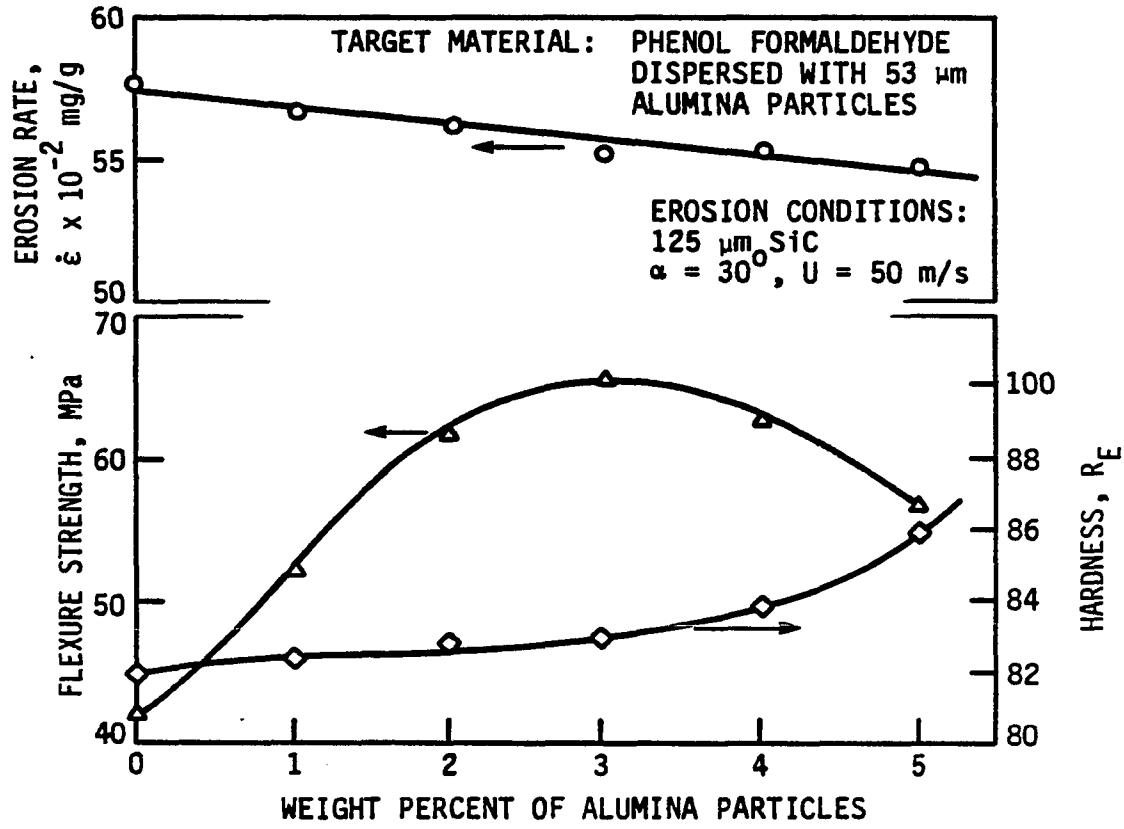

FIGURE 5. Effect of alumina particle concentration on hardness, flexure strength and erosion rate for alumina dispersed phenol formaldehyde

CONCLUSIONS

The following conclusions were made regarding the effects of precipitated hard particles in a soft matrix as found in 2011 aluminum alloy and dispersed hard particles in a phenolic resin:

(1) The erosion rate of soft matrices containing precipitates or dispersed hard particles is not singularly related to either hardness, ductility or strain hardening exponent.

(2) Erosion rate decreases with increase in GP zone diameter and $CuAl_2$ precipitate size during aging of 2011 aluminum.

(3) An increase in the size or concentration of dispersed alumina particles in phenol formaldehyde matrix decreases the erosion rate, and the increased size is more effective in decreasing erosion rate than the concentration.

ACKNOWLEDGMENT

The study was supported by a grant from the Olin Foundation, and the Engineering Research Institute at Iowa State University, Ames, Iowa.

REFERENCES

1. Christman, T. and Shewmon, P. G. "Erosion of a Strong Aluminum Alloy." Wear 52 (1979): 57-70.

2. Grant, G. and Tabakoff, W. "Erosion Prediction in Turbomachinery Resulting from Environmental Solid Particles." Journal of Aircraft 12, NO. 5 (1975): 471-478.

3. Sheldon, G. L. and Kanhere, A. "An Investigation of Impingement Erosion Using Single Particles." Wear 21 (1972): 95-209.

4. Bellman, R., Jr., and Levy, A. "Erosion Mechanisms in Ductile Metals," Wear 70 (1981): 1-27.

5. Smeltzer, C. E., Gulden, M. E. and Compton, W. A. "Mechanisms of Metal Removal by Impacting Dust Particles." Journal of Basic Engineering 92 (1970): 639-654.

6. Salik, J., Buckley, D. and Brainard, W. A. "The Effect of Mechanical Surface and Heat Treatments on the Erosion Resistance of 6061 Aluminum Alloy." Wear 65 (1981): 351-358.

7. Naim, M. and Bahadur, S. "Effect of Microstructure and Mechanical Properties on the Erosion of 18 Ni (250) Maraging Steel." In Wear of Materials-1985, pp. 586-594. Edited by K. C. Ludema. The American Society of Mechanical Engineers, New York, 1985.

8. Brown, R. and Ayers, J. D. "Solid particle Erosion of Al 6061 with Laser melted and TiC Injected Surface Layer." In Wear of Materials-1983, pp. 325-322. Edited by K. C. Ludema. The American Society of Mechanical Engineers, New York, 1983.

9. Jahanmir, S. "The Mechanics of Subsurface Damage in Solid Particle Erosion." Wear 61 (1980): 309-324.

10. Silcock, J. M., Heal, T. J. and Hardy, H. K. "Structural Ageing Characteristics of Binary Aluminum-Copper Alloys." Journal of the Institute of Metals 82 (1953-54): 239-248.

11. Dahlgren, S. D. "Coherency Stresses, Composition and Dislocation Interaction for θ" Precipitate in Aged-Hardened Al-Cu." Metallurgical Transactions 7A (1976): 1401-1405.

12. Finnie, I., Wolak, J. and Kabil, Y, " Erosion of Metals by Solid Particles." Journal of Materials 2, NO. 3 (1967): 682-700.

13. Levy, A. V. and Jahanmir, S. "The Effect of Microstructure of Ductile Alloys on Solid Particle Erosion Behavior." In Corrosion-Erosion Behavior of Materials, pp. 177-189. Edited by K. Natesan, Metallurgical Society of AIME, New York, 1980.

14. Levy, A. V. "The Solid Particle Erosion Behavior of Steel as a Function of Microstructure." Wear 68 (1981): 269-287.

15. Foley, T. and Levy, A. "The Erosion of Heat-Treated Steels." Wear 91 (1983): 45-64.

16. Shah, S. M., Verhoeven, J. D., and Bahadur, S. "Erosion behavior of High Silicon Steels." submitted to Wear.

PAPER 4:

STUDY OF SUBSTRATE DEFORMATION BY PHOTOELASTICITY IN SINGLE PARTICLE IMPACTS

ABSTRACT

Dynamic photoelasticity methods have been used to study the substrate deformation in polyurethane rubber due to the impact of a 3 mm steel ball with a velocity of 50 m/s and at angles of 30° and 90°. The experimental set-up used a multiple-spark camera with an integral polariscope to visualize the dynamic stress field generated by impacting the steel ball using a linear gas gun. The stress field was photographed in the plane of the impact as well as below it. The analysis of the data showed that the rate of propagation of the stress field was 198 m/s. A maximum strain rate of 2,860 m/s was determined after a small time following the impact which also coincided with the time of maximum indentation.

INTRODUCTION

Erosion due to solid particle impacts is a serious problem in pneumatic hammers, typewriter fingers and balls, gas turbine engines, pipes for pneumatic transport of solids, etc. The removal of material in these impact situations depends upon the magnitude of stresses and strains induced, strain rate, nature of deformation, and residual stresses. Several studies have attempted to determine the state of stress and strain rate of deformation due to single impacts on metals [1-3]. Hutchings et al. [1] measured the impact deformation of grains by scanning electron microscopy and the impact duration by high-speed photography. For a mild steel target impacted at 30 degrees with a 9.5 mm diameter steel ball at a velocity of 141 m/s, they estimated a rate of strain of about 10^6/s within the shear band of deformation. Measuring plastic deformation by transmission electron microscopy and determining the impact duration analytically, Narayan [2] estimated a strain rate of 10^5/s in magnesium oxide when impacted by alumina particles of 0.3 to 27 μm diameter at a velocity of 152 m/s. Using analytical expressions and impact crater dimensions, Rickerby and Macmillan [3] also estimated a strain rate of 10^5/s in the case of 1100-0 aluminum specimens impacted normally by 1.58 mm diameter WC-6% Co spheres with a velocity of 54 m/s.

Since target material properties vary with the rate of deformation, the above indirect estimates are at best approximate. A direct assessment of the dynamically induced stresses and strain rates using the techniques of photoelasticity was therefore explored in this work. This paper demonstrates the potential of photoelasticity in the analysis of complex deformation as produced in an impact situation and provides preliminary results on the impact-induced stresses and strain rates in polyurethane rubber.

The principle of photoelasticity capitalizes on the fact that many transparent polymers that are optically isotropic in the stress-free state become optically anisotropic when they are stressed. These materials are called photoelastic materials, as they become doubly refracting when subjected to static or dynamic state of stress. When such photoelastic materials are viewed in properly conditioned polarized light, optical interference produces a fringe pattern. The order of interference, commonly termed the fringe order N, is related to the principal stress difference, $\sigma_1-\sigma_2$, by the stress-optic law [4] as follows

$$\sigma_1-\sigma_2 = N\, f_\sigma/h \qquad \text{(eq. 1.)}$$

where f_σ is known as the material stress fringe value which is a property of the photoelastic material for a given wavelength of light, and h is the model thickness. The stress fringe patterns induced by dynamic load are recorded by high-speed photographic cameras. The isochromatic fringes indicate the location and relative magnitude of stresses at a given time after impact. The fringe order can also be related to the principal strain difference by the following equation [4]

$$\varepsilon_1 - \varepsilon_2 = N f_\varepsilon / h \qquad \text{(eq. 2.)}$$

where f_ε is the material strain fringe value. The differentiation of this equation with respect to time provides the strain rate at a given location. The stress and strain fringe values are also dependent on the loading rate [5]. With increase in strain rate the strain fringe value decreases rapidly whereas the stress fringe value increases slowly. The static stress and strain fringe values have been used in this study due to the lack of reported values under the impact loading condition.

EXPERIMENTAL

The dynamic stress wave visualization was performed using a multiple-spark camera in combination with a linear gas gun, and the residual stress fringes were recorded in a circular polariscope. The multiple-spark camera was used because it provides high framing rate, excellent resolution and large size image. Figure 1 shows the details of the multiple-spark camera used in this work [6]. It has a variable framing rate which can be adjusted in discrete steps from 67,000 to 810,000 frames per second and the effective exposure time is about 0.6 μs per frame.

Essentially, the camera consists of a charging circuit that is connected to sixteen pairs of electrodes arranged in a 4 by 4 rectangular array to provide high intensity sparks. The electrode pairs are solid brass spheres of 13 mm diameter with an air gap of 6 mm. The circuit that provides high intensity multiple sparks in a controlled short duration consists of inductors, resistors and capacitors. The capacitors are connected to the spark electrodes in parallel to resistors that carry the current during charging of the camera. The inductors are air wound and the windings can be tapped at eight different locations so as to vary the effective inductance and the framing rate of the camera.

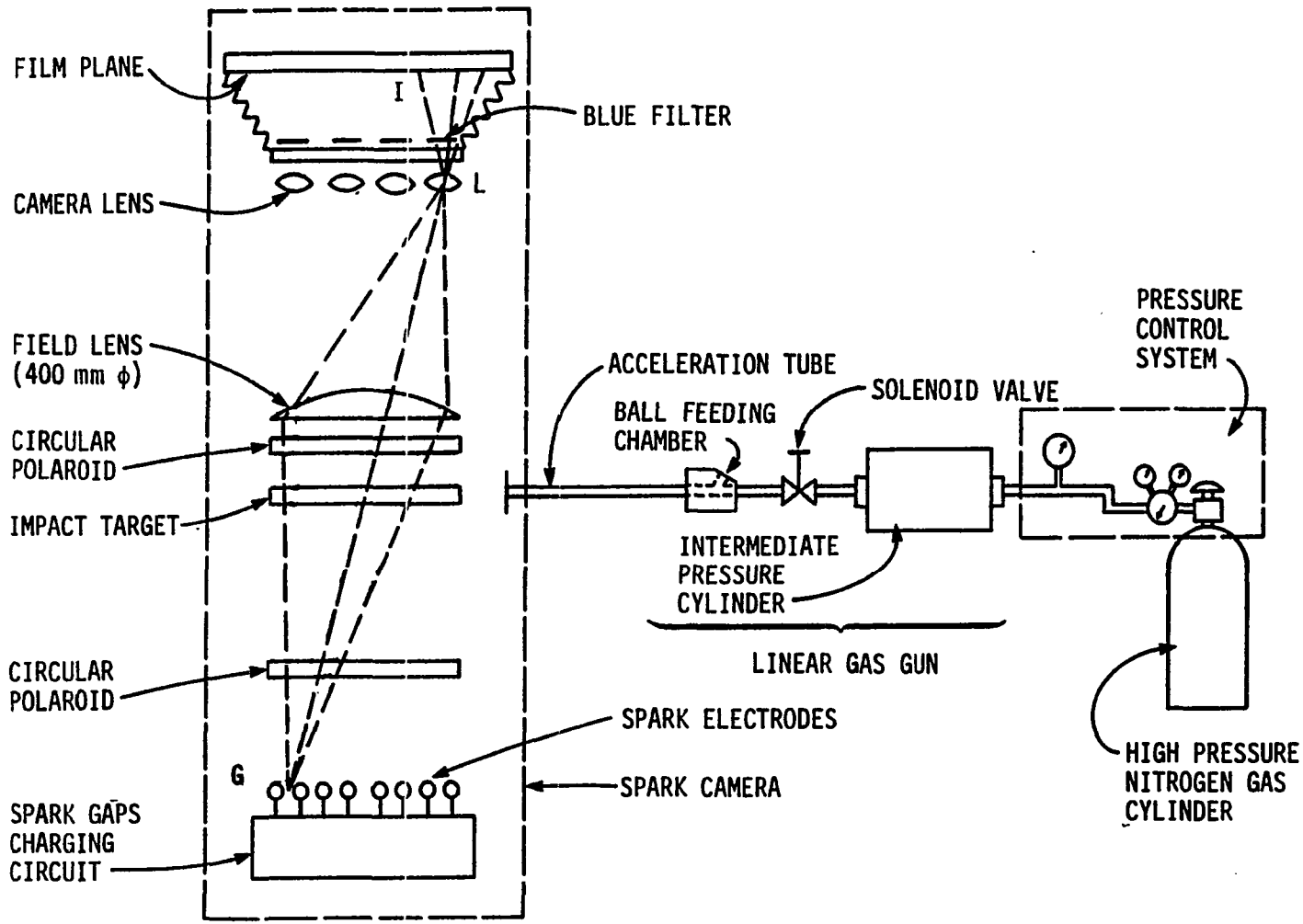

FIGURE 1. Experimental setup showing multiple spark camera and linear gas gun for visualization of dynamic stresses

The camera is operated by initially charging the bank of capacitors to a positive potential of 15 KV by a 15 KV-15 mA DC power supply. A 15 KV pulse from a variable 1 to 20 KV DC trigger module closes the electrical circuit and initiates the sparking sequence as the capacitors start discharging across the electrodes. This discharge produces a voltage oscillation in the electrical circuit going from a positive 15 KV DC to a negative 15 KV DC potential. There is thus a potential difference of 30 KV across any spark gap, which ionizes the air between the electrodes and produces an intense light output. This sequence of events continues through all the 16 spark gaps after which the circuit is discharged through a bleed resistor. The electrical circuit thus provides high intensity multiple sparks in a controlled short duration.

The optical system of the camera consists of two circular polaroids and a large field lens to provide images of stress waves on a film used in the camera assembly. The light from each spark is polarized as it passes through the two circular polaroids separated by a photoelastic target material. It is then focused by a 400 mm diameter plano-convex field lens into a single 35 mm camera lens. There are sixteen 35 mm camera lenses arranged in a 4 by 4 array. The images are focused and separated by adjusting the

distance between the spark electrodes, the field lens, and the camera lenses. It ensures that the light emerging from any spark gap G would be focused by the field lens at the center of a camera lens L without overlap on any other lens. Each lens, therefore, "sees" the light from only one spark and records a 65 mm diameter distinct picture I on a 356 mm by 279 mm film plane. A 4 by 4 array of 16 distinct images is recorded on the film. Each image is associated with the firing time of a particular spark. There is no interference of images or "shadow" from the other sparks. Since the field lens is not color corrected, each wave length emitted by the spark is focused in a different plane and so the image on the film is not in sharp focus. The sharpness of the image is improved by filters that allow the light to be passed in the blue color region (3,500 - 5,100 Å wavelength). The blue color is chosen because it corresponds to the hottest temperature of the spark and lasts for a short duration of about 0.6 μs. The larger wavelengths are associated with the cooler emissions from the spark and last over longer periods.

A linear gas gun, described elsewhere in detail [7], was used to fire 3 mm diameter steel balls to impact the targets. The angle of impact was varied by changing the alignment of the acceleration tube with respect to the

target surface. The operation of the gas gun involved placing a 3 mm diameter steel ball in the feeding chamber followed by manual triggering of the solenoid valve. It releases the compressed gas which propels the ball at high velocity through the acceleration tube thereby resulting in its impact on the target surface.

A control system, shown in Figure 2, was developed to detect the impact of a ball on the target surface and trigger the multiple spark circuit after a desired time delay. Here the pressure pulse generated due to impact was sensed by an accelerometer which was mounted on the target near the impact location. The signal was then passed through a charge amplifier so as to trigger a pulse generator. The latter generates two pulses, a synchronous pulse of 0.5 V that triggers an oscilloscope, and a 20 V pulse that triggers the multiple spark circuit trigger module. The triggering delay time in both pulses is independently adjustable. The variation of light intensity with time from all the spark gaps is sensed by a photocell and is photographed from the oscilloscope. It provides the time after impact as well as the framing rate of the stress field as viewed by the spark camera.

The dynamic stress waves were recorded on a Kodak 4127 film, 279 mm by 356 mm size, which has a fine grain

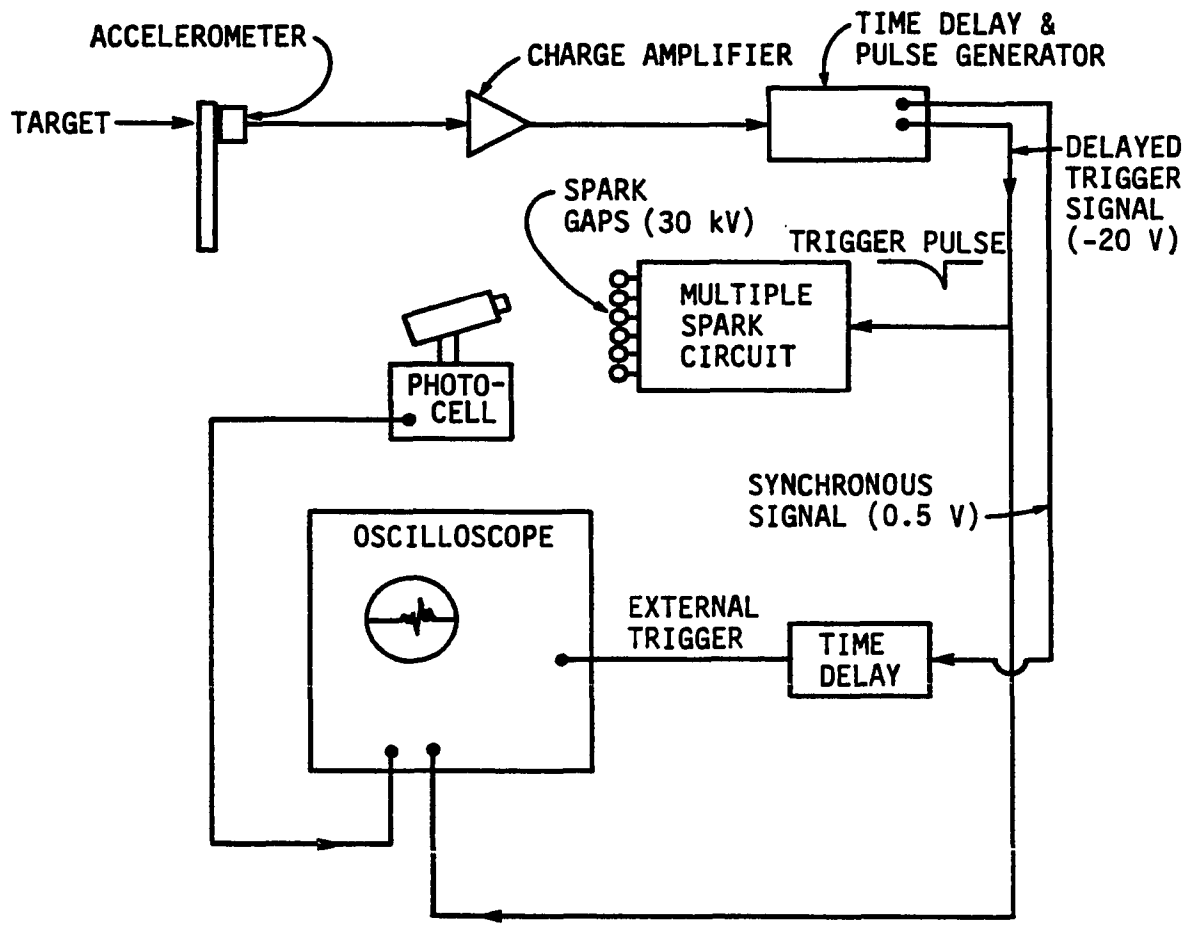

FIGURE 2. Control system for triggering the spark camera

structure and is sensitive to blue light. This, in combination with the filters used, yields a bandwidth of 4,900 to 5,100 Å which is narrow enough to approximate monochromatic light conditions in dynamic photoelasticity. The film was prefogged [4] so as to get high contrast negatives with well-defined isochromatic fringes.

The sequence of operation in an experiment was as follows. A sheet of a photoelastic target material was placed in the polariscope section of the spark camera. The linear gas gun was adjusted for the desired impact velocity and angle. The steel ball was placed in the feeding chamber. The capacitors in the spark circuit were charged to 15 KV. The predetermined time delays were set in the control circuit. The linear gas gun was actuated manually by triggering the solenoid valve with an electrical switch. This resulted in the acceleration of the ball which finally impacted on the target surface. The impact pulse was sensed by the accelerometer and the multiple spark circuit was triggered. A 4 by 4 array of 16 images showing the impact induced dynamic waves were recorded on a single film sheet and the framing rate was determined from the oscilloscope.

Polyurethane rubber (Hysol 8705) in the form of stress-free rectangular plate of 200 mm x 500 mm x 6 mm size was used as the target material because of the following

considerations. Its modulus of elasticity of 3 MPa is low and so it results in low velocity stress waves which are easy to photograph. Its stress fringe value of 0.18 KN/m is low and so it offers the promise of showing more fringes at small loads. The drawbacks of this material are that it is relatively opaque to light and thus results in a poor contrast image on the film. It develops stress fringes because of its own weight and is difficult to deform plastically. Since the impact loads involved were low in this work, it was felt that the advantages of this material outweighed the drawbacks.

RESULTS AND DISCUSSION

The propagation of dynamically induced stress waves was studied by impacting a 3 mm diameter rigid ball at 50 m/s velocity and at an angle of 30 degrees to the surface of the polyurethane rubber plate. The isochromatic stress fringes developed because of impact were photographed in the spark camera. Figure 3 shows the stress wave in the plane of impact after a single impact in sixteen timed frames. Frame 1 shows the stress field induced after 140 μs of impact and the succeeding frames at 14 μs intervals. The dark fringes represent the instantaneous location of the stress wave propagating from the point of impact. The changes in the position of dark fringe from frame to frame show that the stress field is expanding from the point of impact at a uniform velocity of 198 m/s. The outermost fringe in Fig. 3 represents the pressure wave or p-wave [8]. The velocity of p-wave, as estimated from the fringe position, is 198 m/s.

The p-wave velocity C_p can also be predicted [8] by the formula $C_p^2 = E/\{\rho\ (1-\nu^2)\}$, where E is the modulus of elasticity, ρ the density and ν the Poisson's ratio. Using the static values of these properties [9], E = 3 MPa, ρ = 0.0011 g/mm^3, and ν = 0.46, the p-wave velocity works out to be 65 m/s. Therefore, the measured velocity is three times the predicted value. It is so because the modulus of

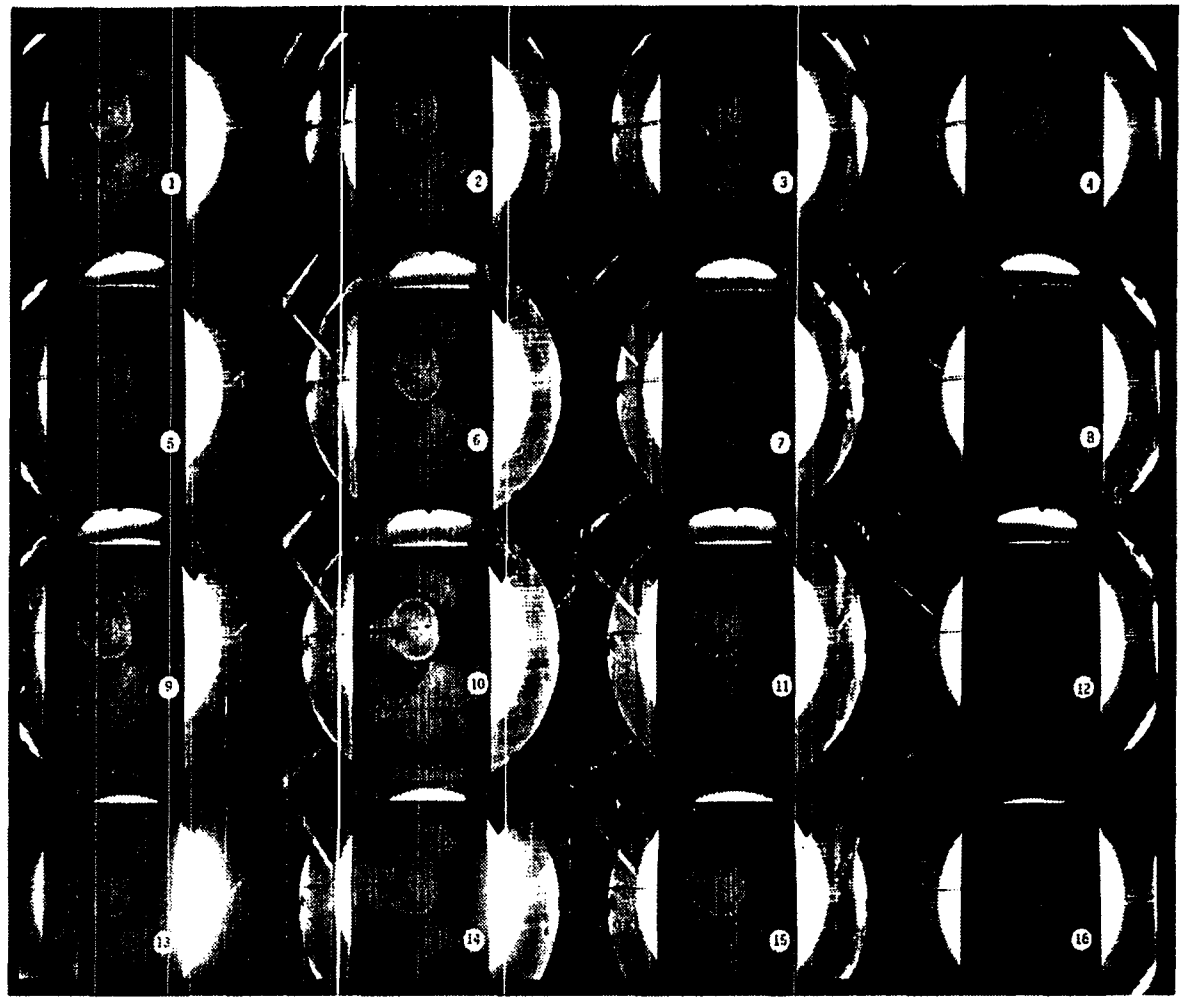

FIGURE 3. Sequence of dynamically induced stress waves in polyurethane rubber plate after a single oblique impact (Ball diameter 3 mm, impact velocity 50 m/s, time after impact 140 μs, framing interval 14 μs)

elasticity also increases with higher rate of loading. Based on the measured and predicted p-wave velocities, the impact induced loading causes a nine fold increase in the modulus of elasticity. It signifies the need to determine the material properties for analytical prediction of erosion at the same loading rate as encountered in erosion.

The frames in Fig. 3 also show an elongated contact zone together with the ball rebounding at a velocity of 48 m/s. Since the impact velocity was 50 m/s, it shows that the loss in kinetic energy due to impact is small, as would be expected for this viscoelastic material which is difficult to deform plastically. The spark camera was unable to resolve the stress wave gradient on the surface of the target material because, in the transmission type polariscope, as used in this work, the light intensity variation is integrated through the target material thickness and so a single band of dark zone was all that could be detected. Thus in the future the surface deformation rate, the dynamic, and the residual stress fields will be studied using Moire' fringe techniques [10].

In order to observe the dynamic stresses induced beneath the point of impact, the steel ball was next impacted with the same velocity normal to the edge of the polyurethane rubber sheet. The dynamic stress fringes

induced, starting after 150 μs of impact, are shown in Fig. 4 and the time interval between each frame is again 14 μs. These fringes represent the pressure wave or p-wave [8]. The impact induced stress field, represented by dark fringes, is expanding concentrically about the impact location in all of the sixteen frames. From the location of the fringes in different frames, the stress field is found to expand with time at a uniform velocity of 198 m/s. This velocity is again higher than that predicted from the static modulus of elasticity for the reasons explained earlier.

The intensity of stress induced by the p-wave at a given location at any time is represented by the fringe order in the particular frame. The fringe order was determined using an image analysis system and the far field from the impact location was treated as being at zero stress level. It was found that in our case the fringe order increased with decreasing distance towards the impact location. The fringes could not be resolved very close to the impact location for very short times after impact as the stress field was very small and the fringes were very close to each other. The fringes were counted in different frames and a plot of the fringe order versus depth below the impact location was prepared for different times after impact, as shown in Fig. 5. Here the fringe order at any location

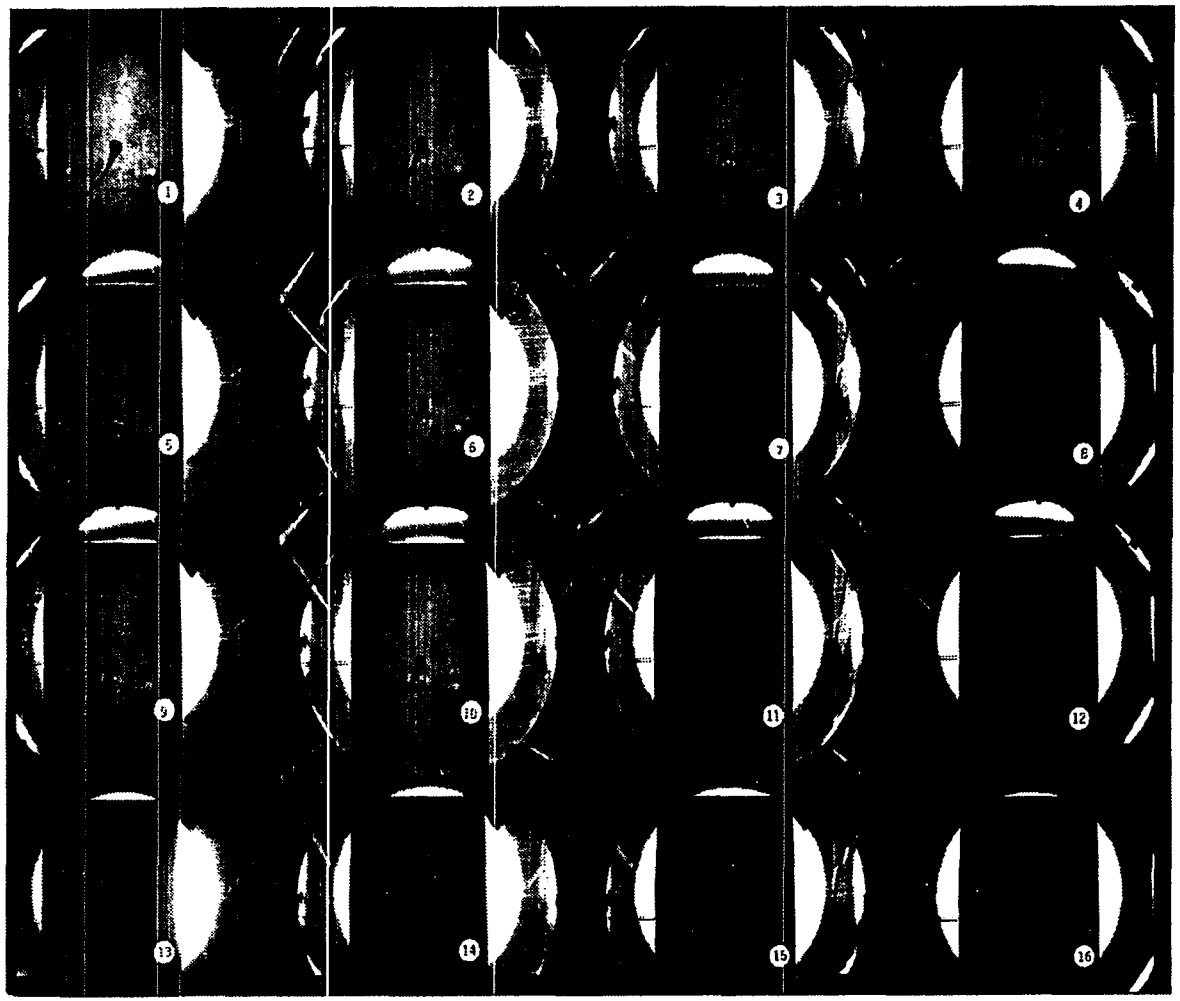

FIGURE 4. Stress waves in polyurethane rubber after a single normal impact on the edge (Ball diameter 3 mm, impact velocity 50 m/s, time after impact 150 µs, framing interval 14 µs)

represents the maximum shear stress. If a stress fringe value of 0.18 KN/m determined under static loading conditions is used, then according to the stress optic law (see equation 1) the maximum shear stress in KPa at any location at a given time would be 15 times the fringe order at that location. For example, at a depth of 15 mm where the fringe order is 6.5, the shear stress is 97.5 KPa after 150 μs of impact. The depth of penetration of the impacting ball and the time of maximum compression, both measured from Fig. 4, were 4.5 mm and 178 μs.

Figure 6 shows the variation of fringe order versus time after impact corresponding to varying depths below the point of impact. It shows that for any depth the longer the time after impact, the higher is the fringe order, which means that the stress intensity at any location increases with increasing time. It has been shown [9,10] that the stress intensity will finally decrease over extended times. The variation in stress intensity with longer times after impact was not pursued due to the slow response of this material to impulse loading. The slopes of these curves represent the rate of change of fringe order with time at any given location. Assuming that the rate of change of strain fringe value, df_ε/dt, is small, equation 2 may be written as

$$d\varepsilon/dt = f_\varepsilon(dN/dt)/h \qquad \text{(eq. 2.)}$$

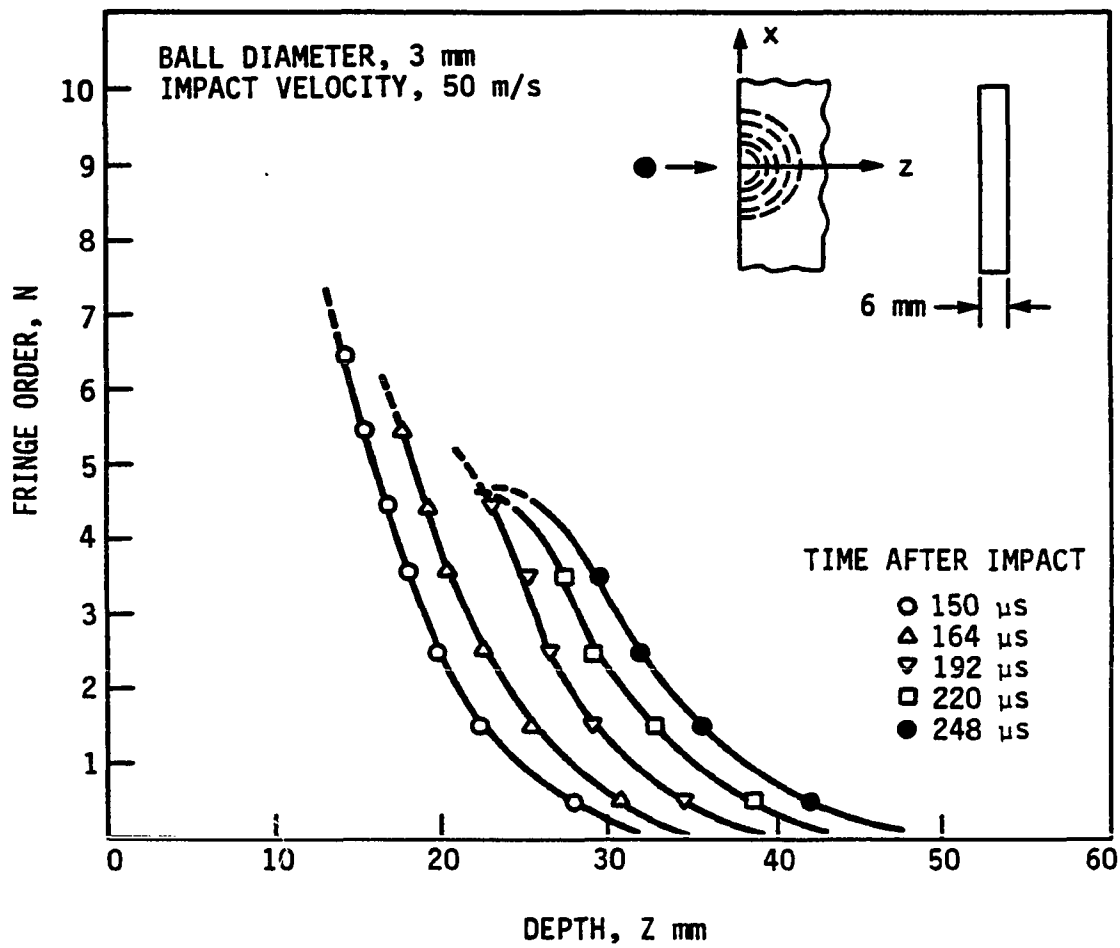

FIGURE 5. Dynamic stress field in polyurethane rubber after a single normal impact

so that dN/dt is directly proportional to the strain rate at any location. Using a static value of f_ε = 0.08 mm, it is found that, at a depth of about 5 times the penetration distance (4.5 mm), the maximum strain rate is 952/s after 150 μs of impact and 2860/s after 178 μs. The latter is the time corresponding to maximum indentation as the ball starts rebounding after this. Figure 6 shows that, at any given location, the induced strain rate increases with increase in time after impact. Studies on low velocity impact [9,10] have shown that at a given location the strain rate or the corresponding stress level reaches a maximum after some time and then decays. The decay is not seen in Fig. 6 because the time after impact covered is not long enough to show the complete pressure pulse caused by the impact at 50 m/s velocity. It is also noted from Fig. 6 that the strain rate at any given time is higher near the impact location and decreases with increasing depth.

Further work is being pursued on polycarbonate as the target material. Since its modulus of elasticity is higher, it will provide a quicker response to impact loading, thereby making the mapping of the stress field far from the impact location possible. It will also be possible to observe in this material the residual plastic deformation which could provide an insight into the mode of material detachment during impact.

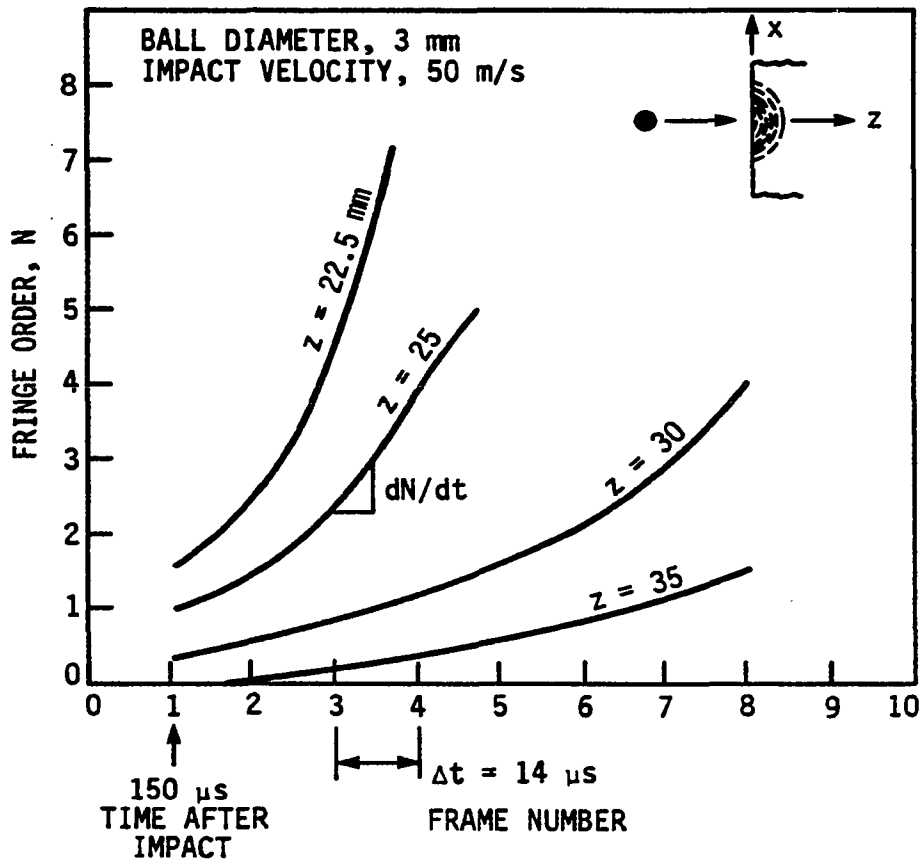

FIGURE 6. Variation of stress in polyurethane rubber after a single normal impact. (Framing interval, 14 μs; depth below the point of impact, Z)

CONCLUSIONS

Dynamic photoelastic methods can be effectively utilized to study the variation in stress and strain rate with time at different locations in an impact zone. This study revealed that in the case of polyurethane rubber the dynamic stress field velocity was 198 m/s which is three times the velocity predicted by the static properties of the target material. It led to the conclusion that the impact induced deformation increased the modulus of elasticity by nine folds. Ignoring slight change in the stress fringe value with higher rates of loading, it was found that the shear stress at a depth of three times the maximum indentation was 100 KPa after 150 μs of impact. Furthermore, a maximum strain rate of 2,860/s was reached at the time of maximum indentation.

ACKNOWLEDGMENT

The study was supported by the Engineering Research Institute at Iowa State University, Ames, Iowa. The guidance from Professor C. P. Burger in the area of dynamic photoelasticity is gratefully appreciated.

REFERENCES

1. Hutchings, I. M., Winter, R. E. and Field, J. E. "Solid Particle Erosion of Metals: The Removal of Surface Materials by Spherical Projectiles." Proceedings Royal Society of London 348 A (1976): 379-392.

2. Narayan, J. " The Characterization of the Damage Introduced During Micro-Erosion of MgO Single Crystals." Wear 25 (1973): 99-109.

3. Rickerby, D. G. and Macmillan, N. H. " The Erosion of Aluminum by Solid Particle Impingement at Normal Incidence." Wear 60 (1980): 369-382.

4. Dally, J. W. and Riley, W. F. Experimental Stress Analysis. McGraw-Hill Book Company, New York, 1978.

5. Durelli, A. J. and Riley, W. F. Introduction to Photomechanics. Prentice-Hall, Inc., Englewood Cliffs, New Jersey, 1965.

6. Ligon, J. B. "A Photomechanics Study of Wave Propagation." Ph. D. dissertation, Iowa State University, Ames, Iowa, 1971.

7. Naim, M. and Bahadur, S. "Effect of Microstructure and Mechanical Properties on the Erosion of 18 Ni (250) Maraging Steel." In Wear of Materials-1985, pp. 586-594. Edited by K. C. Ludema. The American Society of Mechanical Engineers, New York, 1985.

8. Kolsky, H. Stress Waves in Solids. Dover Publications, Inc., New York, 1963.

9. Durelli, A. J. and Riley, W. F. "Stress Distribution on the Boundary of a Circular Hole in a Large Plate During Passage of a Stress Pulse of Long Duration." Journal of Applied Mechanics 28 (1961): 245-251.

10. Riley, W. F. and Durelli, A. J. "Application of Moire Methods to the Determination of Transient Stress and Strain Distribution." Journal of Applied Mechanics 29 (1962): 23-29.

PAPER 5:

SUBSURFACE DEFORMATION STUDIES IN IMPACT EROSION AND PLOWING BY PHOTOELASTICITY

ABSTRACT

Static and dynamic photoelasticity methods have been applied in studying the mechanisms of erosion. A multiple spark camera and a linear gas gun were used to photograph the impact-induced dynamic stress waves. The propagation of stress waves in a polycarbonate material is analyzed on the impact of a 3 mm diameter rigid ball travelling at 50 m/s velocity. The role of pressure, shear, and Rayleigh waves in causing damage is identified. The residual stress field generated due to particle impact is determined using a circular polariscope. It is found that the deformation under impact-induced high strain rates and the residual stress field generated with repeated impacts produce cracking, and the interaction of these cracks results in erosion. The impact on the brittle columbia resin produced lateral, circumferential and radial cracks resulting in material removal. The stress gradient and cracking was also studied during plowing on the above two materials.

INTRODUCTION

The significance of deformation studies in terms of the stresses and strain rates induced during the impact and plowing phases of erosion has been long recognized. Hutchings et al. [1] investigated the removal of material from mild steel targets by impacting 9.5 mm steel balls at oblique angles. They used a high speed camera to determine the rebound velocity and the rotational velocity of the impacting ball. They were able to observe the detachment of material from impact but could not see the crack formation or propagation.

Evans et al. [2] reported the impact damage in brittle materials in the form of radial and lateral cracks. They showed that the extent of the radial fracture depends on the toughness of the target and the velocity and radius of the projectile; while the depth of the lateral fracture depends largely on the hardness of the target and the velocity, radius and density of the projectile. They used numerical analysis to predict the development of a plastic wave and concluded that the stresses are symmetric about the impact center and that the radial and tangential stresses at each location are comparable in magnitude. They did not use experimental techniques to observe the dynamic stress waves. However, they predicted that the driving force for crack

extension during impact is the dynamic tensile stress field developed after the unloading elastic wave interacts with the slower moving plastic wave.

Knight et al. [3] studied by high speed photography the fracturing of pyrex and soda-lime glasses impacted by small steel spheres (800 and 1000 μm diameter). They observed that in the loading cycle the crack growth follows tensile stress trajectories as predicted by the Hertzian stress analysis, but could not resolve the crack propagation in the unloading cycle. They remarked that the reflected stress pulse did not play a crucial role in the initiation of damage within the area of contact. They showed that the impact removal of material was due to the interaction of cone cracks.

Lawn and Swain [4] considered erosion as a surface fragmentation process, where individual chipping events were treated as miniature point indentations. They observed that during indentation on soda-lime glass, cracks propagated from the deformation zone which formed about a contact point. Radial cracks, which spread downward below the point of contact, were formed during loading of the indenter and the unloading produced lateral cracks that spread sideways and eventually to the specimen surface.

Naim and Bahadur [5] studied the residual state of stress after a single normal impact in polycarbonate. They found maximum strain concentration at the center of the indented region and a sharp strain gradient from the center to the periphery. In another study [6], the same workers observed the propagation of dynamic stress waves in polyurethane rubber using photoelasticity techniques. Since the selected photoelastic material deformed slowly, only the impact induced pressure wave could be observed. The study provided the variation of stress with time after impact, and showed a maximum strain rate of 2860/s after 178 μs of impact due to the normal impact of a 3 mm diameter steel ball at a velocity of 50 m/s.

In order to develop a thorough understanding of erosion, it is considered necessary to analyze deformation in the substrate as soon as the impact occurs. It has been shown [7] that when a time-dependent load is applied at a point on one edge of a semi-infinite plate, two basic stress waves, namely, dilatational waves and distortional waves, are generated. These waves propagate radially from the point of impact and their velocities, C_p and C_s, respectively, can be computed from the following equations

$$C_p^2 = E/\{\rho\ (1-\nu^2)\} \quad \{\text{dilatational}\} \quad \text{(eq. 1.)}$$

$$C_s^2 = E/\{2\rho\ (1+\nu)\} \quad \{\text{distortional}\} \quad \text{(eq. 2.)}$$

where ρ, E and ν are the mass density, modulus of elasticity, and Poisson's ratio, respectively, of the impacted material.

The dilatational wave (also called the pressure wave or p-wave) is produced by radial displacements of the target material at the point of load application. The maximum shearing stresses associated with this wave, at every point in the field, make an angle of 45 degrees to the wave front. This maximum shear is independent of the angular position of the point and, as a consequence, the photoelastic fringes associated with p-wave form circular lines with the point of load application as the center [7, 8].

The distortional wave, also called the shear wave or s-wave, is produced by the localized transverse motion of the target material to the direction of propagation of the wave [7]. Therefore, the maximum shearing stresses at every point in the field are in the plane of the wave front. The fringe pattern associated with a distortional wave is quite complex since the magnitude of the maximum shear at any point is a function of the angular position of that point [7].

In this study, the substrate deformation during impact and plowing is analyzed by photoelasticity in terms of the dynamic induced stresses and residual stress field.

EXPERIMENTAL

Two photoelastic materials, viz., polycarbonate and columbia resin, were used in this work. Polycarbonate (PSM-1) is used because of its high figure of merit and high sensitivity index [9] so that a large number of fringes are developed in this material with small loads. It can be deformed plastically and shows good yield and flow characteristics under stress. It also has a short response time to impact loading because of its high modulus of elasticity. Columbia Resin (CR-39) was also used in this investigation, because it is a brittle photoelastic material. It thus provides insight into the development of cracks due to the impact and sliding processes in a brittle material. The photoelastic materials tested were in the form of stress-free rectangular plates of 200 mm x 500 mm x 6 mm size.

The dynamic load induced stress fringe patterns were recorded by a multiple spark camera which provided high framing rate, excellent resolution, and large size image. The residual stress fringes were recorded in a circular polariscope. The multiple spark camera, linear gas gun, and the experimental procedure have been described in detail earlier [6]. Here 3 mm diameter steel balls were impacted normally on the photoelastic target materials at a velocity of 50 m/s using the linear gas gun. The target plate was

placed in the polarizing field of the spark camera. The impact was sensed by a control system that triggered the electrical circuit of the camera providing high intensity multiple sparks in a controlled short duration. The optical system of the camera was capable of light polarization and image separation. The images were obtained in a 4 by 4 array of 16 frames on a single sheet of 279 mm by 356 mm size. The framing rate was determined by a photocell. The wavelength of the light recorded on the film was about 5,000 Å.

A stylus, with a cone angle of 50°, was plowed through both the photoelastic materials at two different speeds, 6 mm/s and 20 mm/s. The plowing features were observed using a Zeiss Universal microscope in transmission mode with polarizing filters through the specimen thickness by changing the depth of the focal point. The use of white light made it possible to observe the stress fringes in color. This allowed for an easy determination of increasing or decreasing order of stress near the deformation zone by identifying the color of the fringes [10].

RESULTS AND DISCUSSION

For the case of a 3 mm diameter steel ball impacted with a velocity of 50 m/s normally to the polycarbonate sheet surface, the fully developed dynamic stress field induced beneath the impact location is shown in Fig. 1. It consists of 16 frames where the first frame was obtained after 66 μs of impact. The frame interval between each succeeding frame is 14 μs. Figure 2 which shows the first frame thus depicts the events at a time of 66 μs after the impact. In this photograph, a surface wave, called Rayleigh wave or R-wave, separates from the Shear wave, called S-wave [7]. The R-wave travels along the surface normal to the direction of impact, with its effective depth of penetration below the surface being equal to two times its wavelength. The S-wave travels below the free surface on which the impact is made. The outermost dark fringe represents the Pressure wave or P-wave [7].

Each frame in Fig. 1 shows the location of stress waves with time. These locations were measured using EyeCom II image analysis system. The measurements provided the velocities of stress waves which are given in Table 1. It is noted that the P-wave velocity is about twice that of the S-wave and, therefore, the P-wave front travels ahead of the S-wave. The R-wave velocity is the lowest. A comparison of

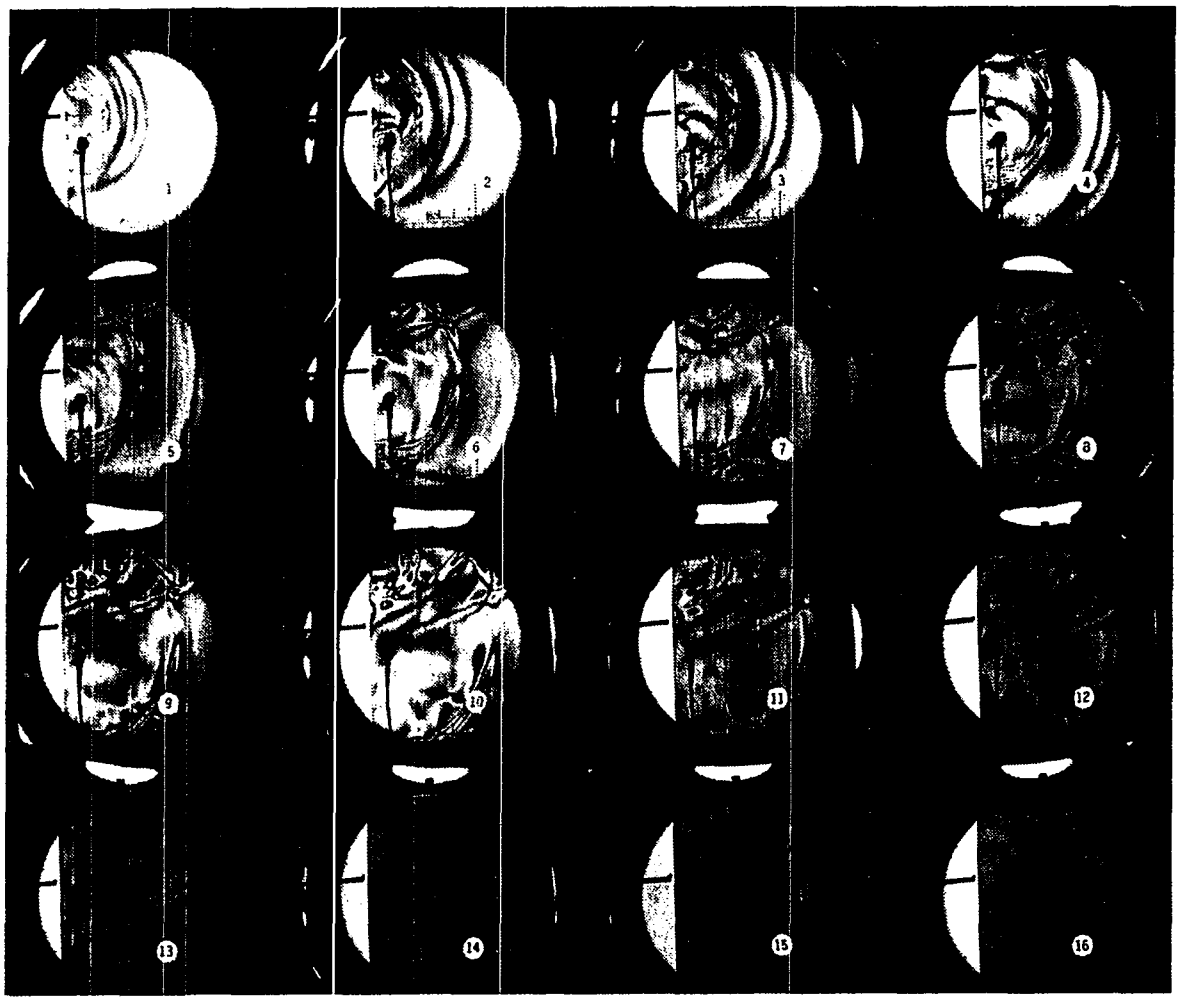

FIGURE 1. Stress waves in PSM-1 after a single normal impact. (Ball diameter 3 mm, impact velocity 50 m/s, time after impact 66 μs, framing interval 14 μs)

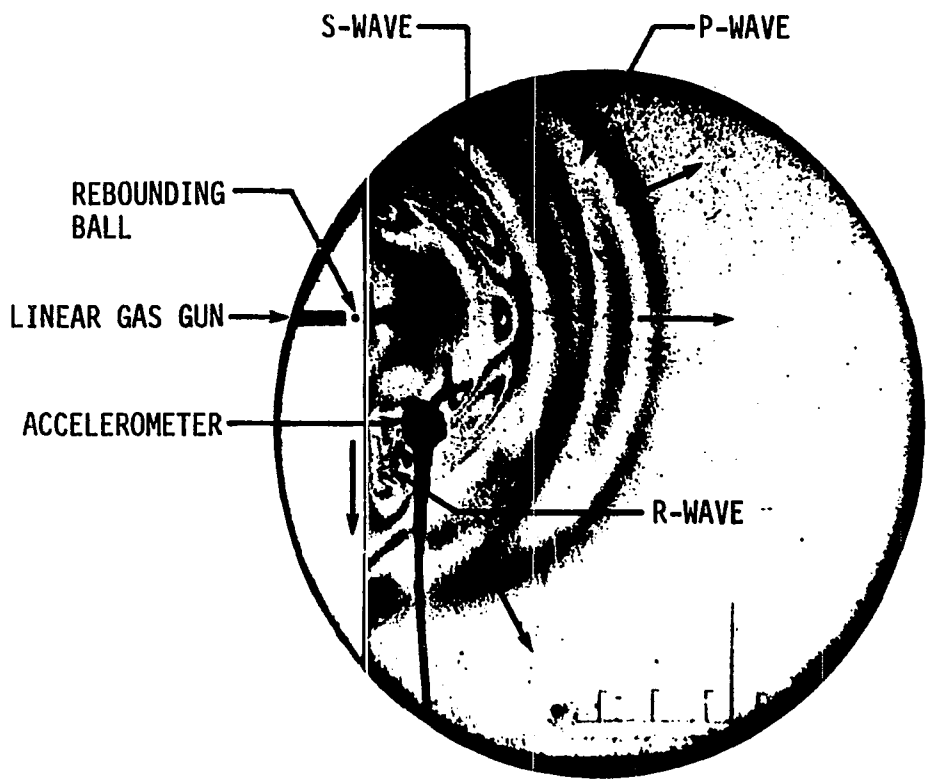

FIGURE 2. Microflash photograph showing stress wave propagation in a polycarbonate target impacted with a 3 mm diameter steel ball at a velocity of 50 m/s (time after impact 66 μs)

the experimentally determined wave velocities with the analytically predicted values indicates that all the experimental values are higher than the predicted values. This is because the dynamic load changes the elastic modulus of the target material [10] while the predictions are based on the static value.

TABLE 1. Stress wave velocities in polycarbonate specimen[1].

Stress wave	Predicted velocity[2], m/s	Experimental velocity, m/s	% Difference
Pressure	C_p = 1956	2000	+2.25
Shear	C_s = 860	920	+6.98
Rayleigh	C_r = 807	820	+1.61

[1] Physical properties of polycarbonate: Poisson's ratio, $\nu = 0.38$; Elastic modulus, $E = 2.39 \times 10^9$ N/m^2, Mass density, $\rho = 1170$ Kg/m^3 [9].

[2] Predicted velocities C_p and C_s determined from equations (1) and (2). $C_r = (0.862 + 1.14\,\nu)/(1 + \nu)\,C_s$.

The variation of R-wave fringe order N with the distance x measured normal to the direction of impact is shown in Fig. 3. The fringe order shows the order of optical interference and is related to the principal stress difference $(\sigma_1-\sigma_2)$ by the stress optic law [9]

$$(\sigma_1-\sigma_2) = N\, f_\sigma/h \qquad \text{(eq. 3.)}$$

where f_σ is the material fringe value and h is the model thickness. The fringe order here is thus proportional to the normal stress tangential to the free surface and the variation of fringe order from positive to negative implies that the stress level goes through tension and compression in the direction of propagation of the R-wave. The tensile stress field ahead of the compression field propagates at a velocity of 820 m/s from the point of impact.

The P-wave originating from the impact location is initially a compression wave. When it reflects from the boundaries of the target material, it becomes tensile and can thus open small cracks in the substrate where the reflecting waves intersect [11]. Frames 5 thru 16 in Figure 1 show the reflecting P-waves and their interaction at several points. In this work, however, the cracks could not be resolved either by the spark camera or by the light microscope in transmission mode. All that could be observed was a small zone of plastic deformation about the impact location with no evidence of material detachment. This indicates that the maximum amplitude of the dynamic stress is reached near the contact zone causing localized plastic deformation. Later, the stress decreases below that of the target material yield strength so that an elastic wave front comprised of P, S and R waves is established. These waves

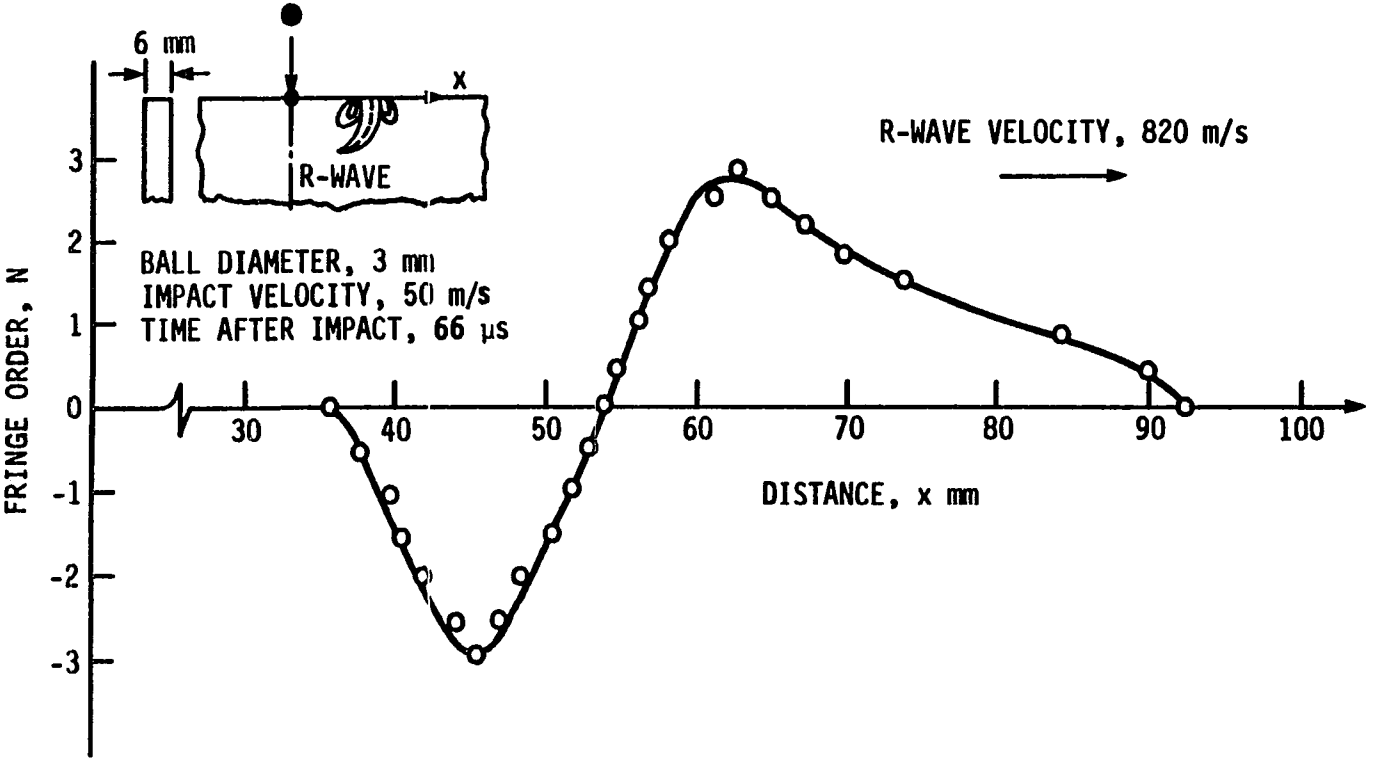

FIGURE 3. The variation of stress amplitude along the surface of a polycarbonate target after a single normal impact

are separated after impact as they propagate with different velocities in the target material. The P-waves, when reflected from the boundaries of the target material, are tensile but are not strong enough to cause any crack nucleation.

To study the stress situation that leads to material removal, the same location was impacted repeatedly. The spark camera arrangement was still unable to resolve the presence of any cracks. The dynamic stress field was the same as shown in Figure 1 after each impact. However, a small residual stress field was observed near the impact location. This implies that the dynamic stress field that causes localized plastic deformation moves on as an elastic stress field because its stress intensity drops below that of the yield strength of the target material. After every impact, the impacted location was examined using transmission light microscopy for the presence of cracks and/or material removal. It was observed that the material removal occurred finally after about 5 to 8 impacts.

The residual stress field fringes were photographed in a standard circularly diffused-light polariscope after each impact. The polariscope was equipped with a monochromatic sodium light source of 589.3 nm wave length. The residual stress field induced after a single normal impact is shown

in Fig. 4. It shows that the residual stress field is symmetrical about the impact direction and the fringes get closer to each other towards the impact crater. The diameter of the crater was found to be 2.10 mm and its depth was 0.23 mm. Based on a static stress fringe value, f_σ, of 7 KN/m [9], the maximum shear stress just below the crater bottom after the first impact is 10 MPa, as calculated from the fringe order of 16 measured at that location. It is also noted that the stress gradient is maximum just below the point of impact, and the residual stress field extends to about three times the impact crater radius.

The case of repeated impacts at the same location was also studied. Here the residual stress field intensity was measured in terms of the fringe order along the z-axis after each impact. The plot of residual fringe order with depth below the point of contact for repeated impacts is given in Fig. 5. Since the fringe orders represent the relative magnitude of residual stresses, the plot shows that the stress magnitude at the crater bottom is maximum after every impact. Repeated impacts did not change significantly the extent of the field of deformation, but an increase in the residual fringe order and the stress gradient was noted just below the impact crater. As a result of 5 to 8 impacts, the fringe order increased from about 16 to 20 which implies

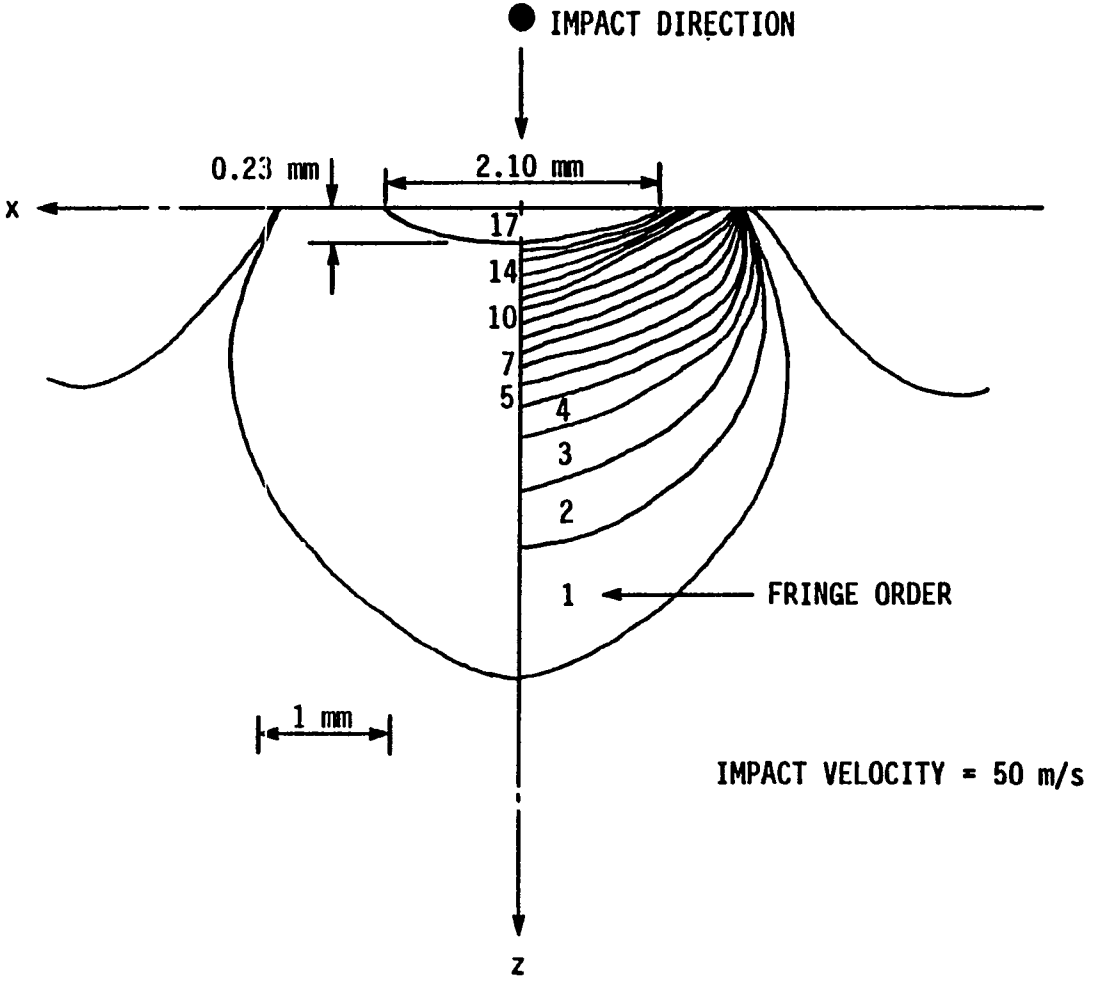

FIGURE 4. Residual stress fringes in a polycarbonate specimen after a single normal impact (bright field, λ = 589.3 nm)

increase in residual stress due to repeated impacts. The stress fringes at a distance greater than about 1.5 times the impact crater radius increased in thickness. This means that the layers of target material with uniform stress are formed at a distance from the impact location while the material close to the crater bottom is much more severely deformed. There is thus a greater possibility of crack nucleation near the impact location due to a high stress gradient than at a larger distance. It was also noted that repeated impacts kept forming layers of material with uniform stress at larger depths which probably accounts for steady state erosion rate after incubation and initial removal of material. The crater surface was observed to be severely deformed and the material was detached in the form of small fragments with smeared surface due to repeated plastic deformation. It was possibly because of the severe plastic deformation of the impact location and the eroded debris that the cracks could not be seen.

In view of the above problem, further investigation of the material detachment due to cracking was carried out using CR-39 (Columbia resin) which is a relatively brittle material. It developed cracks after only one or two impacts. The residual stress field observed in this material was similar to that of polycarbonate. However, the

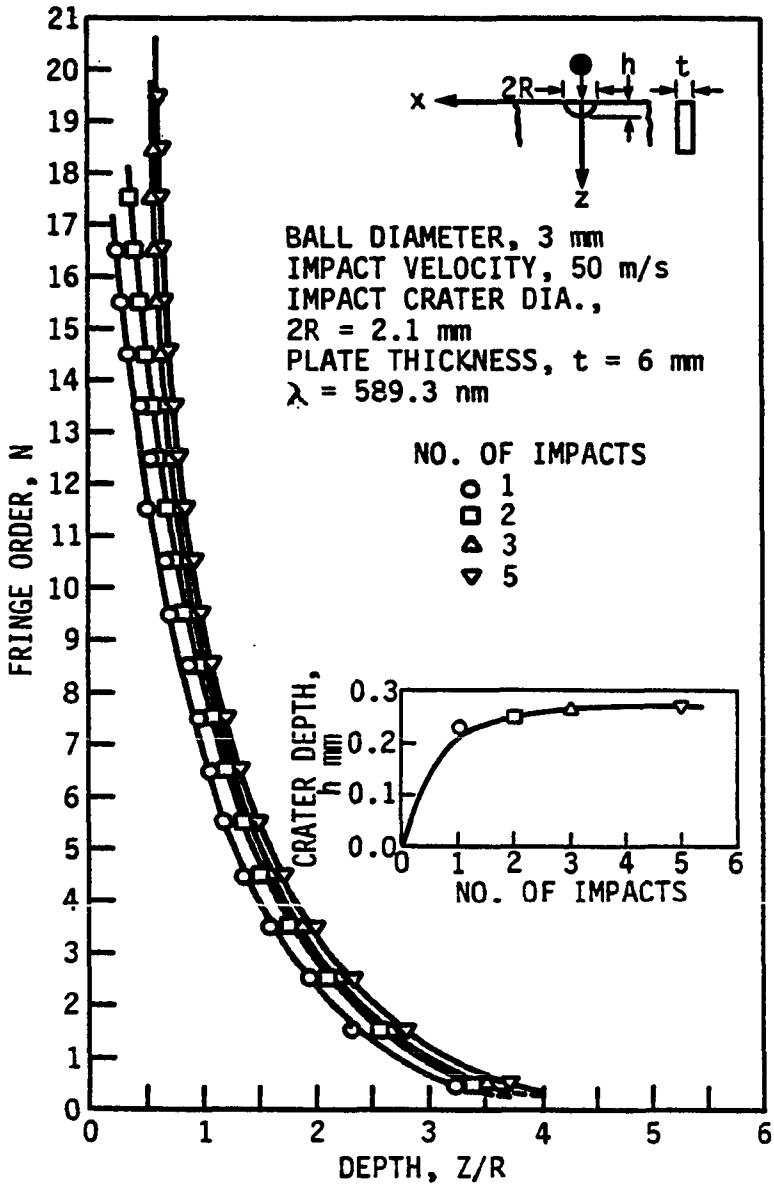

FIGURE 5. Residual stress distribution in polycarbonate for repeated normal impacts

presence of cracks distorted the stress fringes. Figure 6 (a) shows the circumferential and lateral cracks that led to the removal of small chips of material from the surface layers. Whereas the circumferential cracks are confined to the surface layer, the lateral cracks are deeper. There are radial cracks as well that originate a little below the surface in the plastic zone of deformation. Some of these cracks open up to the surface as lateral cracks. Knight et al. [3] also observed the formation of lateral cracks in soda-lime glass using high speed photography. They found that these cracks were formed just prior to complete unloading. The path of propagation of these lateral cracks that open up to the surface is very similar to the residual stress fringes on the sides of the symmetric stress field below the impact point as shown in Fig. 5. Figure 6 (b) also shows the paths of a number of radial cracks originating from the lateral cracks beneath the impact location. These radial cracks propagate into the depth of the target. The detachment of small fragments of material occurs because of the overlapping of these various cracks.

The plowing of CR-39 target surface by a hard conical stylus was also studied. The material on the edges of the plowing groove in Fig. 7 (a) shows a repeated cracking pattern that contributed to the fragmentation of material.

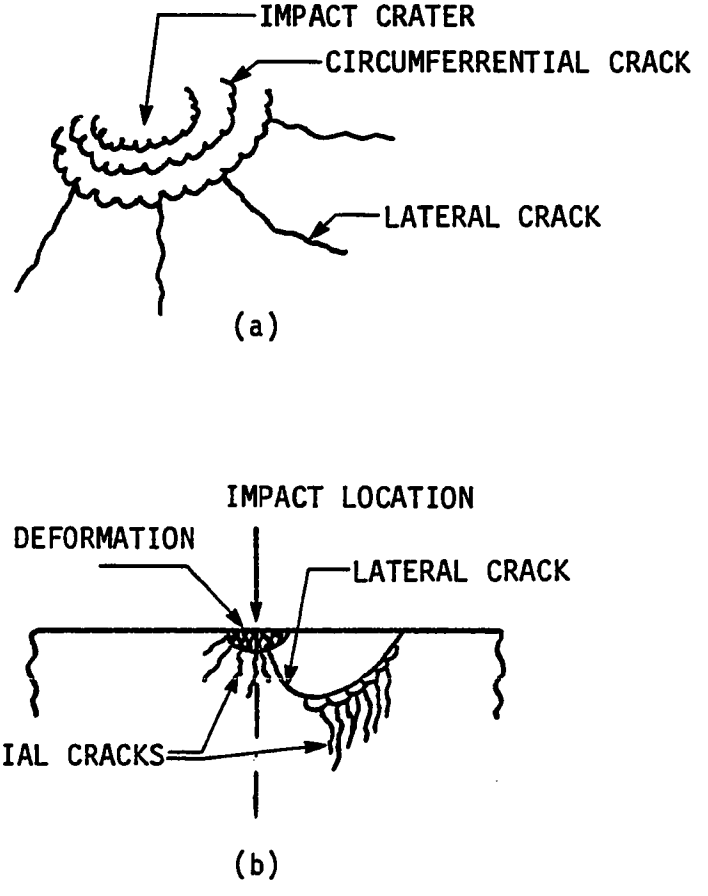

FIGURE 6. Impact damage of CR-39 target surface (a), and substrate (b)

The fragmented material is also shown in Fig. 7 (b). The crack paths are seen both on the specimen surface and on the debris removed. The magnitude of residual stresses, indicated by the presence of stress fringes in polarized light, was minimal. This is because the stresses are released due to crack propagation and subsequent separation of material without substantial plastic deformation. It was found that the increase in sliding speed contributed to smaller size debris removed from the surface.

Figure 8 shows the features of the groove formed and the material removed when the sharp particle was made to slide on the ductile polycarbonate surface at 6 mm/s speed. The debris size decreased as the sliding speed was increased to 20 mm/s. The displaced material was attached on the sides of the groove. The path of the propagation of cracks was again obscured due to accompanying large plastic deformation of material before its detachment from the surface. At small sliding speeds the residual deformation stress field variation was small and the stress intensity was the highest near the tip of the groove in the sliding direction gradually decaying to zero away from the groove. Figure 9 exhibits the subsurface deformation and the residual stress variation due to the sliding of sharp tip at a velocity of 20 mm/s. It shows the presence of a

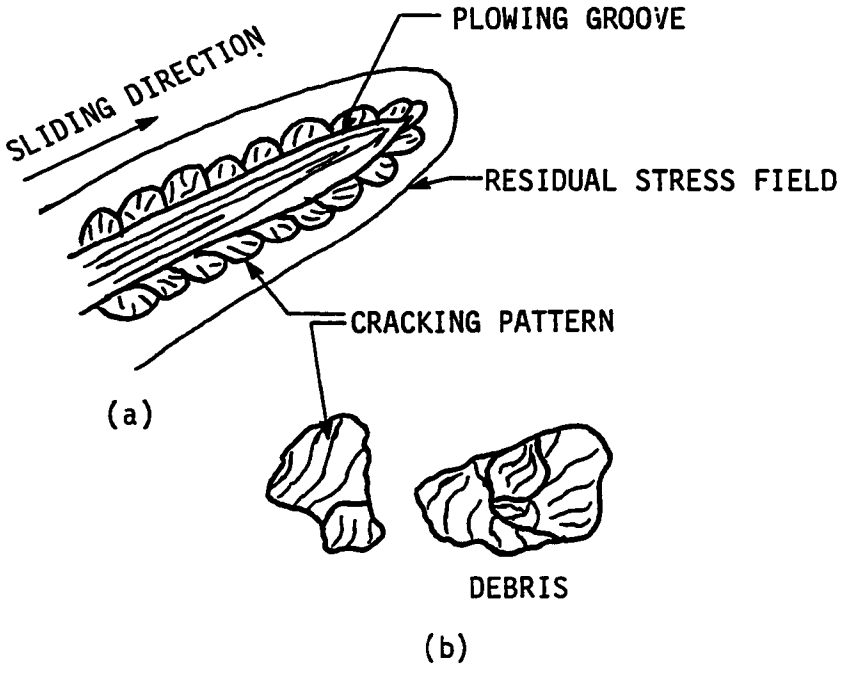

FIGURE 7. Plowing groove on a CR-39 target surface showing repeated cracking pattern (a), and debris from the groove (b)

large number of cracks and the residual stress field developed in the substrate. In addition to cutting and plowing, it is the interlinking of these cracks that contributes to material removal during the sliding process.

With the increase in sliding speed from 6 mm/s to 20 mm/s, the extent of the residual deformation field was reduced to half, but the stress intensity near the scratch was approximately doubled. When a second scratch was made parallel to the first scratch, their fields of deformation overlapped and more material was detached due to cutting, plowing and interlinking of the cracks.

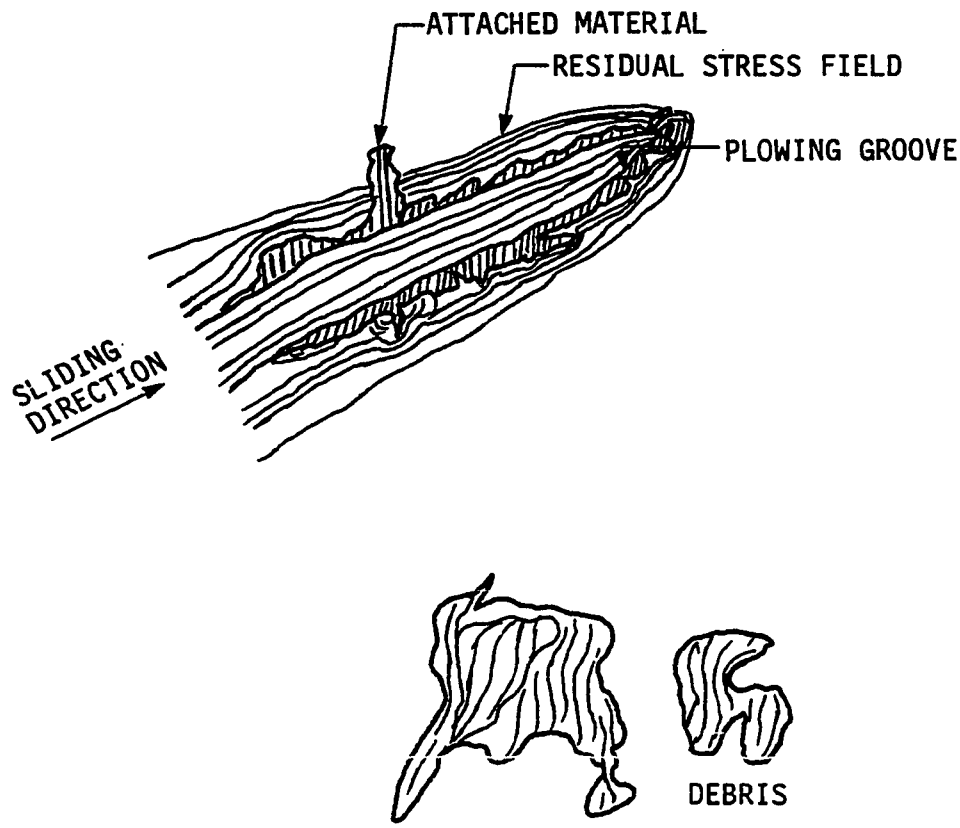

FIGURE 8. Plowing groove on polycarbonate surface and the debris from the groove

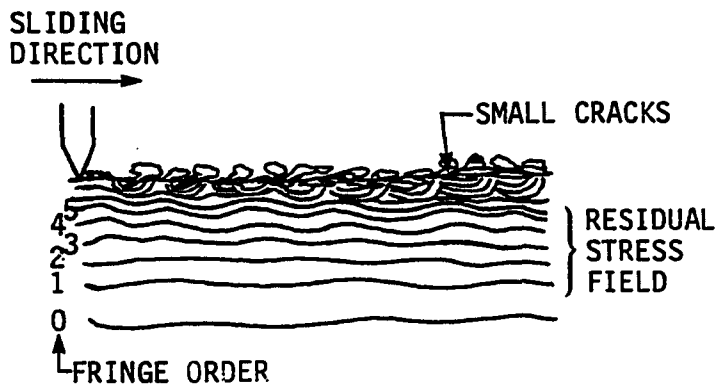

FIGURE 9. Subsurface deformation and the residual stress field due to plowing on polycarbonate surface

CONCLUSION

The dynamic photoelastic studies show that an impact results in plastic deformation and an elastic stress wave front. The plastic deformation is localized near the impact point. The dynamic stress field that causes plastic deformation moves on as an elastic stress field because its stress intensity level drops below that of the yield strength of the target material. This stress field consists of a leading pressure pulse followed by a shear wave. A surface wave also travels away from the impact location with a tensile stress front which is followed by compression. The intensity of the transmitted and reflected waves is not strong enough to cause cracking in the substrate away from the plastic zone of deformation. The residual stress gradient is higher near the impact location. The residual stress field extends up to three times the impact crater radius after the first normal impact. Repeated impacts at the same location cause cumulative plastic deformation and an increase in the residual stress intensity. Substrate cracking originates in this severely deformed plastic region. The cracks propagate to the surface with overlapping paths which results in the detachment of material in small fragments. During plowing the fragments of the target material are removed due to the combination of

cutting and crack formation. Whereas cutting and plowing are the dominant modes of erosion in ductile materials, cracking dominates in brittle materials.

ACKNOWLEDGMENT

This study was supported by the Engineering Institute at Iowa State University, Ames, Iowa. The guidance from Professor C. P. Burger in the area of dynamic photoelasticity is gratefully appreciated.

REFERENCES

1. Hutchings, I. M., Winter, R. E. and Field, J. E. "Solid Particle Erosion of Metals: The Removal of Surface Materials by Spherical Projectiles." Proceedings Royal Society of London 348 A (1976): 379-392.

2. Evans, A. G., Gulden, M. E., and Rosenblatt, M. "Impact Damage in Brittle Materials in the Elastic-Plastic Response Regime." Proceedings Royal Society of London 361A (1978): 343-365.

3. Knight, C. G., Swain, M. V., and Chaudhri, M. M. "Impact of Small Steel Spheres on Glass Surfaces." Journal of Material Science 12 (1977): 1573-1586.

4. Lawn, B. R. and Swain, M. V. "Microfracture Beneath Point Indentations In Brittle Solids." Journal of Material Science 10 (1975): 113-122.

5. Naim, M. and Bahadur, S. " Workhardening in Erosion due to Single-Particle Impacts." Wear 98 (1984): 15-26.

6. Naim, M. and Bahadur, S. "Study of Substrate Deformation by Photoelasticity in Single Particle Impacts." To be published in Wear.

7. Kolsky, H. Stress Waves in Solids. Dover Publications, Inc., New York, 1963.

8. Durelli, A. J. and Riley, W. F. "Stress Distribution on the Boundary of a Circular Hole in a Large Plate During Passage of a Stress Pulse of Long Duration." Journal of Applied Mechanics 28 (1961): 245-251.

9. Dally, J. W. and Riley, W. F. Experimental Stress Analysis. McGraw-Hill Book Company, New York, 1978.

10. Holister, G. S. Experimental Stress Analysis, Principles and Methods. Cambridge University Press, Cambridge, Mass., 1967.

11. Rinehart, J. S. Stress Transients in Solids. HyperDynamics, Santa Fe, New Mexico, 1975.

SUMMARY

The erosion of the precipitation hardening alloys studied can be related to the variation in microstructure and the mechanical properties. It is found that the presence of a soft phase increases the erosion resistance of a hard matrix. The overaging results in the growth of precipitate size which also increases the resistance to erosion. An increase in the size or concentration of dispersed hard particles in a soft matrix decreases the erosion rate, and the increased size is more effective in decreasing erosion rate than the concentration.

The erosion rate varies directly with hardness when ductility remains unchanged during precipitation hardening. It was also found to vary inversely with the percent area reduction when the hardness remained constant. Therefore, the hardness and ductility both affect the erosion resistance of a material. Aging with prior straining results in higher hardness and higher erosion rate, and the higher the prestrain, the higher the hardness and erosion rate for any aging time. Erosion rate is not a unique function of hardness or tensile strength, but it is inversely related to ductility for aged specimens.

It is found that the impact of a ball results in the formation of a pressure wave in the target material that

propagates symmetrically from the impact location. The maximum stress induced in the target is reached after a small time following the impact. The dynamic stress induced reaches a maximum and then decreases. The material undergoes a high strain rate of deformation. An impact, therefore, results in a plastic deformation zone and an elastic stress wave front. The plastic deformation occurs near the impact location. The dynamic stress field that causes plastic deformation moves on as its stress intensity level drops below that of the yield strength of the target material. This stress field then moves with a leading pressure pulse followed by a shear wave. A surface wave also travels away from the impact location with a tensile stress front leading the compression part. The intensity of these transmitted and then reflected waves is not strong enough to initiate cracks in the substrate away from the plastic zone of deformation. The residual stress gradient is higher near the impact location and the residual stress field extends up to three times the impact crater radius after the first normal impact. Repeated impacts at the same location cause cumulative plastic deformation and an increase in the residual stress intensity. Substrate cracking originates from the plastic deformation zone.

Erosion involves the impact and sliding of a particle on a target surface that removes the material by a combination of cutting, plowing, and crack formation. The material is detached in the form of multilayered flakes due to repeated plastic deformation.

ACKNOWLEDGMENT

I would like to acknowledge the constant unyielding efforts of Dr. Shyam Bahadur in the way of search for a better understanding of an event. His guidance, assistance and advice all geared to develop the ability to analyze are invaluable and gratefully appreciated.

The others acknowledged are: The instructors from my first grade and onwards who shared their visions with me to help shape my own. Professor C. P. Burger for his constant encouragement, advice and a lot of help in the area of Experimental Stress Analysis. Professor J. L. Hall for his encouragement, concern and for getting me started in the area of Measurements and Instrumentation. Professor L. C. Peters for his encouragement, identification of a 'Ph.D. material' and advice in handling students the way they are. Professor J. D. Verhoeven for his guidance in the area of Physical Metallurgy.

I dedicate this work to my parents for their dreams, their sacrifice, their encouragement, their love and their affection.